

Derivation and evaluation of interatomic potentials for pure-silica materials

Citation for published version (APA):

Boer, de, K. (1996). *Derivation and evaluation of interatomic potentials for pure-silica materials*. [Phd Thesis 1 (Research TU/e / Graduation TU/e), Chemical Engineering and Chemistry]. Technische Universiteit Eindhoven. <https://doi.org/10.6100/IR465746>

DOI:

[10.6100/IR465746](https://doi.org/10.6100/IR465746)

Document status and date:

Published: 01/01/1996

Document Version:

Publisher's PDF, also known as Version of Record (includes final page, issue and volume numbers)

Please check the document version of this publication:

- A submitted manuscript is the version of the article upon submission and before peer-review. There can be important differences between the submitted version and the official published version of record. People interested in the research are advised to contact the author for the final version of the publication, or visit the DOI to the publisher's website.
- The final author version and the galley proof are versions of the publication after peer review.
- The final published version features the final layout of the paper including the volume, issue and page numbers.

[Link to publication](#)

General rights

Copyright and moral rights for the publications made accessible in the public portal are retained by the authors and/or other copyright owners and it is a condition of accessing publications that users recognise and abide by the legal requirements associated with these rights.

- Users may download and print one copy of any publication from the public portal for the purpose of private study or research.
- You may not further distribute the material or use it for any profit-making activity or commercial gain
- You may freely distribute the URL identifying the publication in the public portal.

If the publication is distributed under the terms of Article 25fa of the Dutch Copyright Act, indicated by the "Taverne" license above, please follow below link for the End User Agreement:

www.tue.nl/taverne

Take down policy

If you believe that this document breaches copyright please contact us at:

openaccess@tue.nl

providing details and we will investigate your claim.

DERIVATION AND EVALUATION OF
INTERATOMIC POTENTIALS FOR
PURE-SILICA MATERIALS

CHRISTINE DE BOER

DERIVATION AND EVALUATION OF INTERATOMIC POTENTIALS FOR PURE-SILICA MATERIALS

PROEFSCHRIFT

ter verkrijging van de graad van doctor aan de
Technische Universiteit Eindhoven, op gezag van
de Rector Magnificus, prof.dr. M. Rem,
voor een commissie aangewezen door het College
van Dekanen in het openbaar te verdedigen op
dinsdag 15 oktober om 16.00 uur

door

Kristine de Boer

geboren te Bennebroek

Dit proefschrift is goedgekeurd door de promotoren:
prof.dr. R.A. van Santen
en
prof.dr.ir. A. van der Avoird

copromotor: dr. A.P.J. Jansen

Universiteitsdrukkerij
T.U. Eindhoven

ISBN 90-386-0328-2

Acknowledgement

The work described in this thesis has been supported by the Netherlands Foundation for Chemical Research (SON) with financial aid from the Netherlands Organization of Pure and Scientific Research (NWO).

*The purpose of computing is insight,
not pictures.*

Contents

1 Introduction	1
1.1 All-silica compounds	1
1.2 Scope of this thesis	2
1.3 Computation of the physical properties of solids	3
1.4 Appendix: Stress and strain	15
1.5 References	17
2 Ab initio approach to the development of interatomic potentials for the shell model of all-silica polymorphs	19
2.1 Introduction	20
2.2 Method	20
2.3 Results	24
2.4 Conclusions	27
2.5 References	28
3 Physical properties of α-quartz at variable temperatures and pressures	29
3.1 Introduction	30
3.2 Computational details	30
3.3 Properties of α -quartz at variable pressures	32
3.4 Properties of α -quartz at variable temperatures	41
3.5 Conclusions	45
3.6 Appendix: Sampling schemes	47
3.7 References	48
4 Derivation of an all-silica shell model potential from ab initio data and the structure of α-quartz	51
4.1 Introduction	52
4.2 Method and computational details	53
4.3 Results	55
4.4 Conclusions	67
4.5 References	69
5 Structure-stability relationships for all-silica polymorphs	71
5.1 Introduction	72
5.2 Computational details	73
5.3 Results	74
5.4 Conclusions	90
5.5 References	91

6 The structure and elasticity of dodecasil-3C at variable temperatures	93
6.1 Introduction	94
6.2 Method and computational details	95
6.3 Results	96
6.4 Conclusions	103
6.5 Appendix: Calculations on stishovite and coesite	104
6.6 References	106
Summary	107
Samenvatting	110
List of publications	113
Dankwoord	114
Curriculum Vitae	115

Chapter 1

Introduction

1.1 All-silica compounds

All-silica (SiO_2) polymorphs are subject to a fast growing interest, both from a scientific and an industrial point of view. They are the most abundant materials on earth, comprising more than 90% by weight of the earth's mantle and crust [1]. These materials found a widespread use in the manufacture of glasses, ceramics, electronic devices and more products mentioned below. Most all-silica materials are composed of SiO_4 units that are connected via Si-O-Si links. The SiO_4 units are rather rigid and approximately tetrahedral. The Si-O-Si links are very flexible, which leads to many possible ways for connecting the SiO_4 units. This results in a large variety of structures [2]. This variety includes dense compounds, such as α -quartz, and more open materials that contain pores and channels. The latter systems are known as all-silica zeolites. These materials can be characterized by their shapes and sizes of the channels and cavities in the structure [2]. Examples of such structures on an atomic scale are given in Fig. 1.1

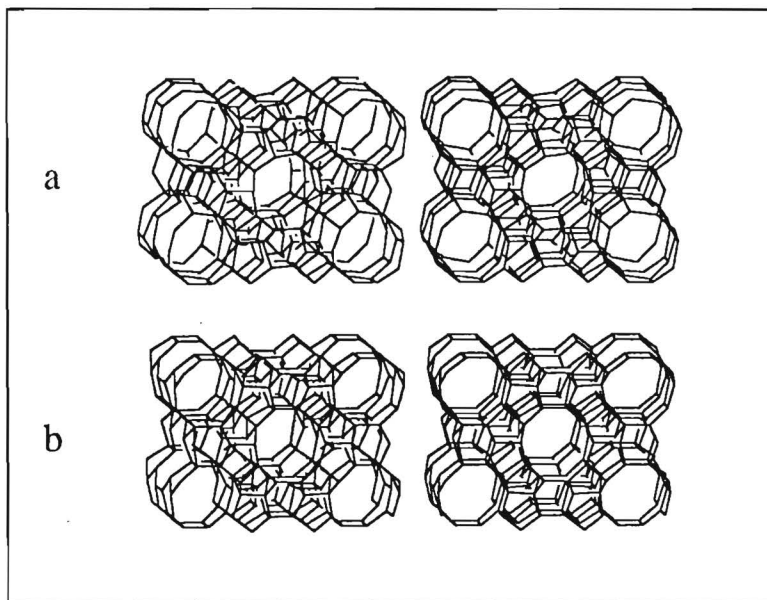


Figure 1.1. Stereographic drawings of the frameworks of a) ZSM5 and b) ZSM-11. Only lines between silicon atoms are drawn. Oxygen atoms are located near the middle of each line [3].

Many types of molecules can be adsorbed in the zeolite cages. These molecules can move rather unhindered in and out of the cages. The name 'zeolite' reflects this property, it stems from $\zeta\epsilon\iota\nu$ (to boil) and $\lambda\iota\theta\omicron\varsigma$ (stone) [4]. This property makes all-silica zeolites very useful for applications such as molecular sieves, detergents and catalysts. Also, these materials are

hydrothermally more stable and contain stronger individual acid sites than the 'common' zeolites [5], which are composed of SiO_4 and AlO_4 units. Furthermore, all-silica zeolites are hydrophobic [6] which favors the reactions with organic molecules. Therefore, the synthesis of these compounds is very important for the production of catalysts. Although many pure and high-silica zeolites have been reported [7], the synthesis of these materials is still a difficult process. Reviews on zeolite synthesis can be found in literature [3]. Research on these interesting compounds is done in virtually any area of materials science. One way to study these materials is the application of computational methods where theoretical models are used to describe the physical properties of solids. The application of such methods has several advantages. First, the behavior of materials at high pressures and temperatures can be studied. Such conditions are not easy to realize in an experiment. These studies can provide information about physical processes in the earth's interior. Second, computational studies of zeolitic systems are important tools in studying the relation between microscopic properties and catalytic activity. These methods allow screening of candidate zeolite structures prior to experimental study, assessment of their catalytic activity, and selection of the most promising candidates for experimental trails [3]. Reviews on current computational techniques can be found in literature. [8–10].

1.2 Scope of this thesis

In this thesis we studied all-silica polymorphs by using a computational technique based on interatomic potentials. The aim of this study is threefold. The first aim is to derive interatomic potentials that can be used to compute the physical properties of all-silica systems. The second aim is to investigate the reliability of these potentials. The third aim is to apply these potentials in studies on the physical properties of several all-silica polymorphs. This thesis is organized as follows: In the remainder of Chapter 1 we describe the theoretical background of the calculations. In Chapter 2 we present the derivation of a new interatomic potential and a brief discussion about its validity. The reliability of this potential is extensively tested in Chapter 3. We have done this by comparing calculated values with experimental data on properties of α -quartz at variable temperatures and pressures. Results of our potential are also compared with those of two other potentials. We will show that each potential can only describe a limited number of α -quartz properties at different conditions. We also give suggestions about how to improve each potential. In Chapter 4 we present a partially improved version of our potential. The predictive power of this potential is investigated by considering the physical properties of several all-silica polymorphs at variable conditions. We will discuss which physical properties are the most accurately described by this potential. The results in Chapters 3 and 4 clearly illustrate which potential should be used for computing certain material properties. In the remaining chapters we used the potentials to study the physical properties of several all-silica polymorphs. In Chapter 5 relationships between the structure and stability of several all silica zeolites are studied. We will show that many of the structure-stability relationships proposed in literature are not valid if many systems are considered. Finally, in Chapter 6 we studied the elasticity and structure of dodecasil-3C at variable temperatures and pressures. The results of this study indicate that the experimental structure of dodecasil-3C may not be well-resolved.

1.3 Computation of the physical properties of solids

Here we will describe the lattice-dynamical theory implemented in the code PARAPOCS [11]. We used this code to calculate the physical properties of solids at variable temperatures and pressures. The implemented method requires the use of interatomic potentials and is different from the well-know approach described by Born and Huang [12]. The latter approach is based on force constants rather than an explicit potential. Two types of interatomic potentials can be used in the calculations: The rigid-ion model potential where each ion is described as non polarizable and the shell model potential which takes polarizability into account. In the shell model, a polarizable ion is represented by two particles, known as the core and the shell. The core is a point charge which has the mass of the ion. The shell is a massless charged particle which is connected to the core by a harmonic spring. The sum of the core and shell charges equals the charge of the ion. The electronic polarization of an ion is then represented by a shell which is displaced with respect to the core [13]. In our derivations we will consider the shell model only. The simplified expressions for the rigid ion model are then immediately obvious. For notational convenience we assume that the shell model potential only acts between ion pairs. The static energy U_{cr}^{stat} of the whole crystal can then be written as [14]

$$U_{cr}^{stat} = \frac{1}{2} \sum_{k'k} \sum_{l'l} \sum_{\tau'\tau}' \Psi(\mathbf{r}_{\tau'}^{k'l'}, \mathbf{r}_{\tau}^{kl}), \quad (1.1)$$

where Ψ denotes the (shell model) potential and \mathbf{r} the position vector of the relevant particle. The indices τ and τ' distinguish the core and shell of the same ion, k and k' denote different ions in the unit cell, and l and l' denote different unit cells. The shell model potential is determined by the position vectors of the relevant particles and the potential parameters. As the potential contains a Coulomb term, Eq. (1.1) requires the summation of Coulomb terms. This is done using the standard Ewald method. Details are given in Ref. 14. The prime in Eq. (1.1) denotes that certain terms must be excluded from the summation. The term with $k' = k$, $\tau' = \tau$ and $l' = l$ must be omitted. The Coulomb term must be excluded in cases where the core and shell are on the same ion. In those cases the term $\Psi(\mathbf{r}_{\tau'}^{kl}, \mathbf{r}_{\tau}^{kl})$ is the harmonic core-shell interaction.

In subsequent derivations we will also consider the static energy per unit cell, U^{stat} , and treat the cores and shells without distinction. The latter energy may then be written as

$$U^{stat} = \frac{1}{2} \sum_l \sum_{n'n}' \Psi(\mathbf{r}_{n'}^0, \mathbf{r}_n^l), \quad (1.2)$$

where the particle indices, n and n' , represent both cores and shells, i.e. $n = \{k, \tau\}$ and $n' = \{k', \tau'\}$. Eqs. (1.1) and (1.2) can be used to calculate the physical properties of a solid at equilibrium. The equilibrium structure can be found by minimization of the Gibbs free energy. We will describe this method first.

1.3.1 Minimization of the Gibbs free energy

To minimize the Gibbs free energy of a solid, the lattice vectors and the coordinates of the particles within the unit cell must be varied until the configuration satisfies two equilibrium conditions. The first condition states that all net mechanical forces on the ions must vanish and is given by [12]

$$\frac{\partial U^{stat}}{\partial r_n^\alpha} = 0, \quad (1.3)$$

where r_n^α denotes the Cartesian component α of the position vector \mathbf{r} of the n -th particle in the cell. The second equilibrium condition states that the configuration must be free of stresses, i.e the net 'generalized' forces per unit area must vanish [12]. This condition is expressed as

$$\frac{\partial G}{\partial \epsilon_{\alpha\beta}} = 0, \quad (1.4)$$

where G is the Gibbs free energy per unit cell and $\epsilon_{\alpha\beta}$ denote the Cartesian components of the 3x3 symmetrical bulk strain matrix ϵ . A comprehensive treatment of strain and stress is given by Nye *et al.* [15] and we discuss them briefly in the Appendix. Notice that derivatives of the Gibbs free energy with respect to the particle coordinates need not to be computed in order to minimize this energy. This has been proven by Born and Huang [12]. Computation of the configuration with minimal Gibbs free energy requires a relation between the equilibrium conditions and the interatomic potential. For the first condition this relation is obvious from Eqs. (1.3) and (1.2). For the second equilibrium this relation can be found if the Gibbs free energy is split in to vibrational and static parts. The Gibbs free energy per unit cell of a solid in any configuration is given by [16]

$$G = U - TS + VP, \quad (1.5)$$

where U is the internal energy per unit cell, S the entropy per unit cell, T the temperature and P the (applied) hydrostatic pressure. The internal energy can be written as [16]

$$U = U^{vib} + U^{stat}, \quad (1.6)$$

where the vibrational energy U^{vib} is the contribution per unit cell from the vibrational motions of the ions including the zero point vibration. If we define the vibrational *free* energy F^{vib} per unit cell as

$$F^{vib} = U^{vib} - TS, \quad (1.7)$$

then the Gibbs free energy per unit cell of any configuration can be expressed as [16]

$$G = F^{vib} + U^{stat} + PV. \quad (1.8)$$

To compute the derivatives of the Gibbs free energy with respect to the strain, a relation between the volume and the strain is needed. The unit cell volume of a strained crystal is given by

$$V = V_0 |(\mathbf{I} + \epsilon)|, \quad (1.9)$$

where V_0 is the volume of the unit cell at zero bulk strain, ϵ the symmetrical bulk strain matrix and \mathbf{I} the identity matrix. (See the Appendix.) Inserting Eqs. (1.8) and (1.9) in Eq. (1.4) gives the second equilibrium condition as

$$\frac{1}{V_0} \frac{\partial F^{vib}}{\partial \epsilon_{\alpha\beta}} + \frac{1}{V_0} \frac{\partial U^{stat}}{\partial \epsilon_{\alpha\beta}} + P \delta_{\alpha\beta} = 0, \quad (1.10)$$

where $\delta_{\alpha\beta}$ is the Kronecker delta. As $\epsilon_{\alpha\beta}$ and $\delta_{\alpha\beta}$ are components of symmetrical matrices, we can group identical terms in this equation by using the Voigt notation. In this notation the relation between Voigt components a_v and Cartesian matrix components $a_{\alpha\beta}$ is given by:

$$\begin{aligned} a_1 &= a_{11}, & a_2 &= a_{22}, & a_3 &= a_{33}, \\ a_4 &= 2a_{23}, & a_5 &= 2a_{13}, & a_6 &= 2a_{12}. \end{aligned} \quad (1.11)$$

In Voigt's notation, Eq. (1.10) is represented as

$$\frac{1}{V_0} \frac{\partial F^{vib}}{\partial \epsilon_v} + \frac{1}{V_0} \frac{\partial U^{stat}}{\partial \epsilon_v} + P(\delta_{1v} + \delta_{2v} + \delta_{3v}) = 0. \quad (1.12)$$

Each term in Eq. (1.12) can be identified as a stress. The kinetic stress σ_v^{kin} , the static stress σ_v^{stat} and the hydrostatic stress σ_v^{hydr} are given by:

$$\sigma_v^{kin} = \frac{1}{V_0} \frac{\partial F^{vib}}{\partial \epsilon_v}, \quad (1.13)$$

$$\sigma_v^{stat} = \frac{1}{V_0} \frac{\partial U^{stat}}{\partial \epsilon_v}, \quad (1.14)$$

$$\sigma_v^{hydr} = -P(\delta_{1v} + \delta_{2v} + \delta_{3v}). \quad (1.15)$$

In order to solve Eqs. (1.3) and (1.12), the variation of the static energy with respect to the bulk strain components and the particle coordinates must be computed. Provided that the crystal is subject to small deformations during the free energy minimization, we may expand the static energy of a lattice configuration about any other configuration to second order in the bulk strain components and particle coordinates. First we will consider the static energy of crystals in the absence of electric fields and discuss more general cases later. In the former case the crystal must be isolated from external charges and the material may not possess a permanent (macroscopic) dipole moment. Pyroelectric materials have a permanent dipole moment but for these systems we can bring the field to zero by considering crystals that are earthed [12,14]. In this assumption, no field terms contribute to the static energy. Hence, expansion of the static energy about an arbitrary configuration will contain derivatives of the potential energy only. These derivatives can be calculated from the potential energy function given by Eq. (1.2). At this point it is convenient to introduce some vector and matrix definitions. The vector \mathbf{r} representing the particle configuration within one unit cell is defined as

$$\mathbf{r} = [r_n^\alpha]. \quad (1.16)$$

This vector has dimension $3N$ where N is the number of particles (cores *and* shells) per cell. The six-dimensional bulk strain vector ϵ and stress vector σ are defined as:

$$\epsilon = [\epsilon_v], \quad \sigma = [\sigma_v]. \quad (1.17)$$

Vectors that contain first derivatives of the potential energy with respect to the particle coordinates and bulk strain components are defined as:

$$\mathbf{g}_r = \frac{\partial U^{stat}}{\partial \mathbf{r}}, \quad \mathbf{g}_\epsilon = \frac{\partial U^{stat}}{\partial \epsilon}. \quad (1.18)$$

Matrices containing second derivatives of the potential energy with respect to the particle coordinates and bulk strain components are defined as:

$$\begin{aligned} \mathbf{W}_{rr} &= \frac{\partial^2 U^{stat}}{\partial \mathbf{r} \partial \mathbf{r}^T}, & \mathbf{W}_{r\epsilon} &= \frac{\partial^2 U^{stat}}{\partial \mathbf{r} \partial \epsilon^T}, \\ \mathbf{W}_{\epsilon r} &= \frac{\partial^2 U^{stat}}{\partial \epsilon \partial \mathbf{r}^T}, & \mathbf{W}_{\epsilon\epsilon} &= \frac{\partial^2 U^{stat}}{\partial \epsilon \partial \epsilon^T}. \end{aligned} \quad (1.19)$$

Using definitions (1.16)–(1.19), expansion of the static energy to second order can be written as

$$U^{stat}(\tilde{\mathbf{r}}) = U^{stat}(\mathbf{r}) + (\mathbf{g}_r \quad \mathbf{g}_\epsilon) \begin{pmatrix} d\mathbf{r}^T \\ d\epsilon^T \end{pmatrix} + \frac{1}{2} (d\mathbf{r} \quad d\epsilon) \begin{pmatrix} \mathbf{W}_{rr} & \mathbf{W}_{r\epsilon} \\ \mathbf{W}_{\epsilon r} & \mathbf{W}_{\epsilon\epsilon} \end{pmatrix} \begin{pmatrix} d\mathbf{r}^T \\ d\epsilon^T \end{pmatrix}, \quad (1.20)$$

where $\tilde{\mathbf{r}}$ denotes a particular configuration and \mathbf{r} any other configuration. The relation between these configurations is given by

$$\tilde{\mathbf{r}} = (\Delta\epsilon + \mathbf{I})(\mathbf{r} + d\mathbf{r}), \quad (1.21)$$

where $\Delta\epsilon$ is a symmetrical matrix with elements $d\epsilon_{\alpha\beta}$. The vector $d\epsilon$ in Eq. (1.20) is defined as

$$\tilde{\epsilon} = \epsilon + d\epsilon, \quad (1.22)$$

where $\tilde{\epsilon}$ represents an arbitrary bulk strain and ϵ any other bulk strain. Equation (1.21) simply states that a new configuration $\tilde{\mathbf{r}}$ can either be obtained by changing the bulk strain or the particle coordinates within the cell. The derivatives in Eq. (1.19) are calculated using analytical expressions derived for the potential energy function given by Eq. (1.2). Details can be found in Ref. 14. Using definitions (1.13)–(1.18) we write equilibrium conditions (1.3) and (1.12) as:

$$\mathbf{g}_r = 0, \quad (1.23)$$

$$\sigma^{tot} = 0, \quad (1.24)$$

where the total stress σ^{tot} is given by

$$\sigma^{tot} = \sigma^{kin} - \sigma^{hydr} + \sigma^{stat} \quad (1.25)$$

The configuration with minimal Gibbs free energy is found by application of an iterative three-step procedure based on Eqs. (1.20) and (1.23)–(1.25). We will outline these steps first and discuss them later in more detail. The calculations start with a trial configuration, usually taken from experimental data. In the first step of the iterations, the cell dimensions of the trial configuration are held constant, i.e. the bulk strain is kept fixed, and the particle coordinates are varied until the static energy is minimal as required by Eq. (1.23). This step will be referred to as minimization of the static energy at constant strain. In the second step, the phonon frequencies are calculated for the configuration obtained in the first step. From these frequencies the vibrational free energy is computed. Subsequently, the kinetic stress is computed from the vibrational frequencies by using Eq. (1.13) and Eq. (1.45) discussed below. Given the kinetic and hydrostatic stress, the kinetic stress is then adjusted in the third step until the total stress is zero as required by Eq. (1.24). Adjustment of the kinetic stress is done by variation of the bulk strains in the crystal which changes the cell dimension. See Eq. (1.14). This last step will be referred to as removal of the total stress. The altered cell dimensions in the last step have changed the configuration. This requires a new minimization at constant strain and computation of new values for the phonon frequencies and the kinetic stress. A new value for the kinetic stress requires another adjustment of the static stress. This changes the cell dimensions again *et cetera*. The calculations are repeated until both the particle coordinates and cell dimensions do not change any more. Each step of the calculations will be explained in more detail below.

1.3.2 Minimization of the static energy at constant strain

In this part of the calculations, the static energy of the crystal is minimized while keeping the cell dimensions constant. The latter is achieved by keeping the bulk strains fixed. This part of the computations is often referred to as minimization at constant volume. For fixed bulk strain the expression for the static energy [Eq. (1.20)] reduces to

$$U^{stat}(\tilde{\mathbf{r}}) = U^{stat}(\mathbf{r}) + \mathbf{g}_r d\mathbf{r}^T + \frac{1}{2} d\mathbf{r} \mathbf{W}_{rr} d\mathbf{r}^T, \quad (1.26)$$

where

$$\tilde{\mathbf{r}} = \mathbf{r} + d\mathbf{r}, \quad (1.27)$$

which is Eq. (1.21) for constant bulk strain. As the bulk strains do not vary, equilibrium condition (1.23) must be satisfied only. Equations (1.23), (1.26) and (1.27) define an iterative scheme to locate the minimum of the static energy if the matrix \mathbf{W}_{rr} is positive definite. In this scheme the coordinates must be updated according to:

$$\tilde{\mathbf{r}} = \mathbf{r} - \mathbf{g}_r \mathbf{H}_{rr}, \quad (1.28)$$

where $\mathbf{H}_{\mathbf{r}\mathbf{r}} = \mathbf{W}_{\mathbf{r}\mathbf{r}}^{-1}$. To reach convergence, Eq. (1.28) must be applied iterately until $\mathbf{g}_{\mathbf{r}} = \mathbf{0}$. In each cycle the large $\mathbf{W}_{\mathbf{r}\mathbf{r}}$ matrix must be calculated and subsequently inverted. This is computationally expensive. Therefore, the Norget-Fletcher procedure [17] is applied where the inverse of $\mathbf{W}_{\mathbf{r}\mathbf{r}}$ is updated according to the approximate expression:

$$\mathbf{H}_{\bar{\mathbf{r}}\bar{\mathbf{r}}} = \mathbf{H}_{\mathbf{r}\mathbf{r}} + \frac{d\mathbf{r}d\mathbf{r}^T}{d\mathbf{r}d\mathbf{g}_{\mathbf{r}}^T} - \frac{\mathbf{H}_{\mathbf{r}\mathbf{r}}d\mathbf{g}_{\mathbf{r}}^Td\mathbf{g}_{\mathbf{r}}\mathbf{H}_{\mathbf{r}\mathbf{r}}}{d\mathbf{g}_{\mathbf{r}}\mathbf{H}_{\mathbf{r}\mathbf{r}}d\mathbf{g}_{\mathbf{r}}^T}, \quad (1.29)$$

where $d\mathbf{g}_{\mathbf{r}} = \mathbf{g}_{\bar{\mathbf{r}}} - \mathbf{g}_{\mathbf{r}}$. The approach implemented in PARAPOCS is that only after a fixed number of iterations the inverse of $\mathbf{W}_{\mathbf{r}\mathbf{r}}$ is computed. For the intervening iterations the matrix $\mathbf{W}_{\mathbf{r}\mathbf{r}}$ is updated with the Norget-Fletcher procedure. Another approach to reduce computational costs would be the inclusion of symmetry constraints, by relating the displacements of particles which are equivalent by symmetry. These constraints are *not* included and the structure is thus allowed to reduce its symmetry if this leads to a lower energy structure.

1.3.3 Calculation of the phonon frequencies and the kinetic stress

The kinetic stress is calculated from the phonon frequencies, and we will first describe the method for determining them. These frequencies can only be calculated for equilibrium configurations that satisfy Eq. (1.23). Those configurations are obtained from the minimization at constant strain. The phonon frequencies are obtained by solving the equations of motion for each particle in the crystal [18]. In our discussion concerning the stability of the crystal we could consider shells and cores as independent particles and hence treat them identically. At this point it is more convenient to consider separate equations of motion for the cores and shells, because the latter particles are massless. The equations of motion for the cores in the *whole* crystal are

$$-\frac{\partial U_{cr}^{stat}}{\partial \mathbf{u}_c^{kl}} = m^k \ddot{\mathbf{u}}_c^{kl}, \quad (1.30)$$

where U_{cr}^{stat} is the static energy of the whole crystal and \mathbf{u}_c^{kl} the displacement of the k -th core in unit cell l . The mass m^k of this core is equal to the mass of the k -th ion in the unit cell. For the massless shells the equations are

$$\frac{\partial U_{cr}^{stat}}{\partial \mathbf{u}_s^{kl}} = 0, \quad (1.31)$$

where \mathbf{u}_s^{kl} is the displacement of the k -th shell in unit cell l . The last equation is equivalent to the adiabatic approximation, where it is assumed that the electron clouds (shells) follow the movements of the atomic nuclei (cores) instantaneously [13]. Solvation of the equations of motion requires a relation between the static energy and displacements of the cores and shells. Hence we expand the static energy in terms of those displacements. As the configuration satisfies Eq. (1.23), we consider displacements from equilibrium positions only. We assume that these displacements are small (the harmonic approximation). The

static energy of an arbitrary configuration may then be expanded about the equilibrium configuration up to second order in the shell and core displacements. Again we assume that no electric field terms contribute to the static energy. Thus, expansion of the static energy will contain potential energy derivatives only. First we introduce a vector and matrix notation for the above quantities. Vectors representing the core and shell displacements are given by

$$\mathbf{u}_c = [\mathbf{u}_c^{kl}], \quad \mathbf{u}_s = [\mathbf{u}_s^{kl}]. \quad (1.32)$$

The dimension of these vectors is $3M$ times the number of unit cells, where M is the number of ions per cell. Matrices that contain derivatives of the potential energy with respect to the core and shell displacements are given by:

$$\begin{aligned} \Phi^{cc} &= \left(\frac{\partial^2 U_{cr}^{stat}}{\partial \mathbf{u}_c \partial \mathbf{u}_c^T} \right)_{\substack{\mathbf{u}_c=0 \\ \mathbf{u}_s=0}}, & \Phi^{cs} &= \left(\frac{\partial^2 U_{cr}^{stat}}{\partial \mathbf{u}_c \partial \mathbf{u}_s^T} \right)_{\substack{\mathbf{u}_c=0 \\ \mathbf{u}_s=0}}, \\ \Phi^{sc} &= \left(\frac{\partial^2 U_{cr}^{stat}}{\partial \mathbf{u}_s \partial \mathbf{u}_c^T} \right)_{\substack{\mathbf{u}_c=0 \\ \mathbf{u}_s=0}}, & \Phi^{ss} &= \left(\frac{\partial^2 U_{cr}^{stat}}{\partial \mathbf{u}_s \partial \mathbf{u}_s^T} \right)_{\substack{\mathbf{u}_c=0 \\ \mathbf{u}_s=0}}. \end{aligned} \quad (1.33)$$

The second derivative matrices are calculated using analytical expressions derived from the potential energy function given by Eq. (1.1). Details can be found in Ref. 14. Using the above definitions and approximations we can write the static energy of the crystal as

$$U_{cr}^{stat}(\mathbf{u}_c, \mathbf{u}_s) = U_{cr}^{stat}(\mathbf{0}, \mathbf{0}) + \frac{1}{2} \begin{pmatrix} \mathbf{u}_c & \mathbf{u}_s \end{pmatrix} \begin{pmatrix} \Phi^{cc} & \Phi^{sc} \\ \Phi^{sc} & \Phi^{ss} \end{pmatrix} \begin{pmatrix} \mathbf{u}_c^T \\ \mathbf{u}_s^T \end{pmatrix}, \quad (1.34)$$

where $U_{cr}^{stat}(\mathbf{0}, \mathbf{0})$ is the static energy of the equilibrium configuration with zero displacements. Equation (1.34) does not contain linear terms because we consider equilibrium configurations only. Substitution of Eq. (1.34) in the equations of motion would give an infinite number of second order differential equations. These equations can be linearized and their number can be reduced to $3M$ if we consider solutions of the following form [18]:

$$\mathbf{u}_c^{kl} = \mathbf{w}_c^k \exp[i(\check{\mathbf{r}}_c^{kl} \cdot \mathbf{k} - \omega t)], \quad (1.35)$$

$$\mathbf{u}_s^{kl} = \mathbf{w}_s^k \exp[i(\check{\mathbf{r}}_s^{kl} \cdot \mathbf{k} - \omega t)]. \quad (1.36)$$

where \mathbf{w}_c^k is the displacement of the k -th core in each cell, \mathbf{w}_s^k the displacement of the k -th shell in each cell, \mathbf{k} an arbitrary wave vector, ω the phonon frequency and t the time. Notice that the latter displacements are independent of the cell index l . The vectors $\check{\mathbf{r}}_c^{kl}$ and $\check{\mathbf{r}}_s^{kl}$ are equilibrium positions of the core and shell, respectively. These particles represent ion k in unit cell l . The identical frequencies in these solutions are a consequence of the adiabatic approximation [Eq. (1.31)]. Substitution of Eqs. (1.36) and (1.35) in the equations of motion gives [13]

$$\mathbf{R}\mathbf{u}_c + \mathbf{T}\mathbf{u}_s = \omega^2 \mathbf{M}\mathbf{u}_c, \quad (1.37)$$

$$\mathbf{T}^\dagger \mathbf{u}_c + \mathbf{S}\mathbf{u}_s = \mathbf{0}, \quad (1.38)$$

where $\mathbf{M} = m_k \delta_{kk'} \delta_{\alpha\beta}$, $\mathbf{w}_c = [\mathbf{w}_c^k]$ and $\mathbf{w}_s = [\mathbf{w}_s^k]$.

The matrices \mathbf{R} , \mathbf{T} and \mathbf{S} are given by:

$$\mathbf{R} = \sum_{l'k'} \Phi_{l'k'lk}^{cc} \exp [i(\tilde{\mathbf{r}}_c^{l'k'} - \tilde{\mathbf{r}}_c^{lk} \cdot \mathbf{k})], \quad (1.39)$$

$$\mathbf{T} = \sum_{l'k'} \Phi_{l'k'lk}^{cs} \exp [i(\tilde{\mathbf{r}}_c^{l'k'} - \tilde{\mathbf{r}}_s^{lk} \cdot \mathbf{k})], \quad (1.40)$$

$$\mathbf{S} = \sum_{l'k'} \Phi_{l'k'lk}^{ss} \exp [i(\tilde{\mathbf{r}}_s^{l'k'} - \tilde{\mathbf{r}}_s^{lk} \cdot \mathbf{k})], \quad (1.41)$$

where $\Phi_{l'k'lk}^{\tau'\tau}$ ($\tau', \tau = c, s$) are elements of the matrices $\Phi^{\tau'\tau}$ given in Eq. (1.33). Notice that elements of \mathbf{R} , \mathbf{T} and \mathbf{S} have indices k and k' only. These elements are independent of the cell index l , which is due to the lattice periodicity. We can eliminate the shell displacements from Eqs. (1.37) and (1.38) and set the core displacements \mathbf{w}_c^k equal to the atomic displacements \mathbf{w}^k to give

$$\omega^2 \mathbf{M} \mathbf{w} = (\mathbf{R} - \mathbf{T} \mathbf{S}^{-1} \mathbf{T}^\dagger) \mathbf{w}, \quad (1.42)$$

where $\mathbf{w} = [\mathbf{w}^k]$.

If we define the Dynamical matrix \mathbf{D} and the mass-weighted atomic displacements \mathbf{n} as:

$$\mathbf{D} = \mathbf{M}^{-1/2} (\mathbf{R} - \mathbf{T} \mathbf{S}^{-1} \mathbf{T}^\dagger) \mathbf{M}^{-1/2}, \quad (1.43)$$

$$\mathbf{n} = \mathbf{M}^{-1/2} \mathbf{w}, \quad (1.44)$$

then we can write Eq. (1.42) as an eigenvalue problem given by

$$\omega^2 \mathbf{n} = \mathbf{D} \mathbf{n}. \quad (1.45)$$

Normal coordinate analysis of Eq. (1.45) gives for each wave vector \mathbf{k} the solutions $\omega_j(\mathbf{k})$, where $j = 1, 2, \dots, 3M - 6$, as the rotational and vibrational degrees of freedom have been excluded. These solutions are the vibrational frequencies of $3M - 6$ independent harmonic oscillators [18].

We will now describe how the vibrational free energy and the kinetic stress are computed from the phonon frequencies. The vibrational free energy for $3M - 6$ independent harmonic oscillators is given by [16]

$$F^{vib} = kT \sum_{j\mathbf{k}} \frac{x_j(\mathbf{k})}{2} + \ln \left(1 - \exp[-x_j(\mathbf{k})] \right), \quad (1.46)$$

where

$$x_j(\mathbf{k}) = \frac{\hbar \omega_j(\mathbf{k})}{kT}. \quad (1.47)$$

Computation of the vibrational free energy requires summation over the frequencies for all wave vectors in the Brillouin-zone. This is done by computing only the frequencies for wave vectors on a three-dimensional mesh within the Brillouin-zone. The sum is then taken over these frequencies using appropriate weighting factors [10]. Phonon frequencies at the Γ point must be omitted from Eq. (1.46) because the Ewald sum contains a singularity at $\mathbf{k} = \mathbf{0}$ [12,18]. We recall that the kinetic stress is related to the vibrational free energy as

$$\sigma_v^{kin} = \frac{1}{V_0} \frac{\partial F^{vib}}{\partial \epsilon_v}. \quad (1.13)$$

Eqs. (1.46) and (1.13) show that an analytical expression for the static stress is difficult to find, if not impossible. Therefore, the kinetic stress is calculated numerically. This is done as follows: First the vibrational free energy F^{vib} is calculated for the equilibrium configuration by using Eqs. (1.45) and (1.46). Then the crystal is subjected to small bulk strains $d\epsilon_v$ in each of the six directions. Subsequently, the vibrational energy F_v^{vib} is calculated for each of the strained cells. Each component of the kinetic stress is then calculated with the difference formula given below.

$$\sigma_v^{kin} = \frac{1}{V_0} \frac{(F_v^{vib} - F^{vib})}{d\epsilon_v}. \quad (1.48)$$

Equations (1.13) and (1.48) are equivalent if the applied bulk strains are sufficiently small.

1.3.4 Removal of the total stress

Given the hydrostatic and kinetic stress, the total stress on the crystal can be removed by adjustment of the static stress [see Eqs. (1.25) and (1.24)]. This part of the computations is often referred to as minimization at constant pressure. Adjustment of the static stress is done by variation of the bulk strains by using Eq. (1.14). This requires a relation between the static energy and the bulk strains only, which can be found as follows: First we consider an equilibrium configuration \mathbf{r} obtained from the minimization at constant strain. Equilibrium condition (1.23) may then be applied to the expression for the static energy [Eq. (1.20)], which gives

$$d\mathbf{r} = -d\epsilon \mathbf{W}_{\epsilon\mathbf{r}} \mathbf{H}_{\mathbf{r}\mathbf{r}}, \quad (1.49)$$

where $\mathbf{H}_{\mathbf{r}\mathbf{r}} = \mathbf{W}_{\mathbf{r}\mathbf{r}}^{-1}$. We can eliminate $d\mathbf{r}$ from the static energy expression by substitution of Eq. (1.49) in Eq. (1.20), which gives

$$U^{stat}(\tilde{\mathbf{r}}) = U^{stat}(\mathbf{r}) + \mathbf{g}\epsilon d\epsilon^T + \frac{1}{2}d\epsilon(\mathbf{W}_{\epsilon\epsilon} - \mathbf{W}_{\epsilon\mathbf{r}}\mathbf{H}_{\mathbf{r}\mathbf{r}}\mathbf{W}_{\mathbf{r}\epsilon})d\epsilon^T. \quad (1.50)$$

We now consider changes in the particle configuration that are only caused by variation of the bulk strain components. The changed configuration $\tilde{\mathbf{r}}$ is then related to the configuration \mathbf{r} at equilibrium by

$$\tilde{\mathbf{r}} = (\Delta\epsilon + \mathbf{I})\mathbf{r}, \quad (1.51)$$

which is Eq. (1.21) for $d\mathbf{r} = \mathbf{0}$. If the matrix $\mathbf{C}_{\epsilon\epsilon}^{stat}$ is defined as

$$\mathbf{C}_{\epsilon\epsilon}^{stat} = \frac{1}{V_0}(\mathbf{W}_{\epsilon\epsilon} - \mathbf{W}_{\epsilon\mathbf{r}}\mathbf{H}_{\mathbf{r}\mathbf{r}}\mathbf{W}_{\mathbf{r}\epsilon}), \quad (1.52)$$

then Eq. (1.50) can be written as a function of variation in the bulk strain only:

$$U^{stat}(\tilde{\epsilon}) = U^{stat}(\epsilon) + \mathbf{g}_\epsilon d\epsilon^T + \frac{1}{2}d\epsilon\mathbf{C}_{\epsilon\epsilon}^{stat}d\epsilon^T, \quad (1.53)$$

where we have replaced $U^{stat}(\tilde{\mathbf{r}})$ by $U^{stat}(\tilde{\epsilon})$ and $U^{stat}(\mathbf{r})$ by $U^{stat}(\epsilon)$ as we consider changes in the bulk strain only. We recall that:

$$\tilde{\epsilon} = \epsilon + d\epsilon, \quad (1.22)$$

and that the second equilibrium condition is given by

$$\boldsymbol{\sigma}^{tot} = \mathbf{0}, \quad (1.24)$$

where $\boldsymbol{\sigma}^{tot}$ is the first derivative of the Gibbs free energy with respect to the strain. In this part of the calculations both the kinetic and static stress are kept constant. Variation of the Gibbs free energy is then only due to variation of the static energy, i.e.,

$$\frac{dU^{stat}}{d\epsilon} = \frac{dG}{d\epsilon}, \quad (1.54)$$

where $dU^{stat} = U^{stat}(\tilde{\epsilon}) - U^{stat}(\epsilon)$ for sufficiently small steps and dG is defined similarly. Substituting Eq. (1.54) and the definition of $\boldsymbol{\sigma}^{tot}$ [Eq. (1.25) in Eq. (1.53)] gives

$$G(\tilde{\epsilon}) = G(\epsilon) + \boldsymbol{\sigma}^{tot}d\epsilon^T + \frac{1}{2}d\epsilon\mathbf{C}_{\epsilon\epsilon}^{stat}d\epsilon^T. \quad (1.55)$$

Equations (1.22), (1.24) and (1.55) define an iterative scheme where the bulk strain components must be updated according to

$$\tilde{\epsilon} = \epsilon + \boldsymbol{\sigma}^{tot}(\mathbf{C}_{\epsilon\epsilon}^{stat})^{-1}, \quad (1.57)$$

until $\boldsymbol{\sigma}^{tot} = \mathbf{0}$. Each variation $d\epsilon$ in this iterative scheme requires a new minimization at fixed strain to ensure that Eq. (1.49) remains satisfied. Notice that the second equilibrium condition [Eq. (1.24)] can also be achieved by considering an expression where the Gibbs free energy is expanded directly to second order in the strain. This expression requires second derivatives of the Gibbs free energy with respect to the strain. These derivatives are not implemented in the program [10]. This almost concludes our treatment of the free energy minimization method implemented in PARAPOCS. We recall that the method described so far is only valid for crystals in the absence of electric fields. If we consider isolated pyroelectric crystals, which possess a permanent dipole moment, then the macroscopic electric field must be taken into account. In those cases, the method proceeds the

same as before, except that in all equations \mathbf{g}_r , \mathbf{W}_{rr} and \mathbf{H}_{rr} must be replaced by $\hat{\mathbf{g}}_r$, $\hat{\mathbf{W}}_{rr}$ and $\hat{\mathbf{H}}_{rr}$, respectively [14]. The latter quantities are given by

$$\hat{\mathbf{g}}_r^\alpha = \mathbf{g}_r^\alpha + 4\pi P^\alpha(\mathbf{r})\mathbf{q}, \quad (1.58)$$

$$\hat{\mathbf{W}}_{rr}^{\alpha\beta} = \mathbf{W}_{rr}^{\alpha\beta} + \delta_{\alpha\beta} \left(\frac{8\pi}{V_0} \right) \mathbf{q}\mathbf{q}^T, \quad (1.59)$$

$$\hat{\mathbf{H}}_{rr} = \hat{\mathbf{W}}_{rr}^{-1}, \quad (1.60)$$

where $\mathbf{P}(\mathbf{r})$ is the permanent dipole moment of configuration \mathbf{r} and \mathbf{q} an N-dimensional row vector defined by:

$$\mathbf{q} = [q_n], \quad (1.61)$$

where q_n is the charge of the n -th particle (core or shell) in the cell. For details see Ref. 14. The free energy minimization for a crystal subject to a displacement field induced by *external* charges is not implemented in PARAPOCS.

Many properties of the thermodynamically equilibrated structure can be calculated with PARAPOCS. We will describe only the computation of properties discussed in this thesis.

1.3.5 Crystal properties

For a given temperature, the isothermal elastic constants $\mathbf{C}_{\epsilon\epsilon}$ are defined as [15]

$$\mathbf{C}_{\epsilon\epsilon} = \frac{1}{V_0} \frac{\partial^2 G}{\partial \epsilon \partial \epsilon^T}. \quad (1.62)$$

The constants implemented in PARAPOCS are the *adiabatic* elastic constants $\mathbf{C}_{\epsilon\epsilon}^{stat}$ defined as

$$\mathbf{C}_{\epsilon\epsilon}^{stat} = \frac{1}{V_0} \frac{\partial^2 U^{stat}}{\partial \epsilon \partial \epsilon^T}, \quad (1.63)$$

for fixed entropy. These constants are given by [see Eqs. (1.53), (1.60) and (1.63).]

$$\mathbf{C}_{\epsilon\epsilon}^{stat} = \frac{1}{V_0} (\mathbf{W}_{\epsilon\epsilon} - \mathbf{W}_{r\epsilon} \hat{\mathbf{H}}_{rr} \mathbf{W}_{\epsilon r}), \quad (1.64)$$

Equation (1.64) gives the adiabatic elastic constants neglecting temperature. Thus, the vibrational part of the elastic constants at elevated temperatures is neglected in the calculations. Work of Harding *et al.* [19] has shown that this approximation is reasonable. The low-frequency dielectric constants $\epsilon_{\alpha\beta}^0$ are given by [18]

$$\epsilon_{\alpha\beta}^0 = \delta_{\alpha\beta} + \frac{4\pi}{V_0} [\mathbf{q}^T \hat{\mathbf{H}}_{rr} \mathbf{q}]_{\alpha\beta}, \quad (1.65)$$

The high-frequency dielectric constants $\epsilon_{\alpha\beta}^0$ are given by [18]

$$\epsilon_{\alpha\beta}^0 = \delta_{\alpha\beta} + \frac{4\pi}{V_0} [\check{\mathbf{q}}^T \hat{\mathbf{H}}_{rr}^{\check{\check{}}} \check{\mathbf{q}}]_{\alpha\beta}, \quad (1.66)$$

where $\widehat{\mathbf{H}}_{\mathbf{rr}}^{ss}$ denotes the submatrix of $\widehat{\mathbf{H}}_{\mathbf{rr}}$ which contains the shell-shell interaction only. The vector $\widehat{\mathbf{q}}$ contains only the shell charges. Derivations of Eqs. (1.65) and (1.66) can be found in Ref. 14. Expressions for the free energy of crystals in an displacement field are not implemented in PARAPOCS. Therefore, care must be taken when comparing experimental and calculated values for the elastic and dielectric constants of piezoelectric materials. An electric field applied to a piezoelectric crystal, such as α -quartz, induces an elastic strain and vice versa [15]. Computed elastic constants of piezoelectric solids must therefore be compared with experimental zero field values. Calculated low-frequency dielectric constants of these materials must be compared with values measured for a clamped crystal. This means that the solid must be mechanically constrained to prevent deformation induced by the applied field during the measurement. The latter does not apply for the high-frequency constants [18].

Finally we will discuss computation of the thermodynamical properties encountered in this thesis. The entropy per unit cell, S , is given by

$$S = k \sum_{\mathbf{jk}} \frac{x_j(\mathbf{k})}{(\exp[x_j(\mathbf{k})] - 1)} - \ln(1 - \exp[-x_j(\mathbf{k})]) \quad (1.67)$$

The constant volume heat capacity C_v is computed from

$$C_v = k \sum_{\mathbf{jk}} \frac{(x_j(\mathbf{k})^2 \exp[x_j(\mathbf{k})])}{(\exp[x_j(\mathbf{k})] - 1)} \quad (1.68)$$

Equations (1.67) and (1.68) are derived in Ref. 16. They are valid for a set of independent harmonic oscillators. The sums required by these equations are done with an appropriate wave vector grid, as discussed in Sect. 1.2.3. The constant pressure heat capacity C_p is given by [20]

$$C_p = C_v + \beta^2 \mathcal{K} T V, \quad (1.69)$$

where \mathcal{K} is the bulk modulus and β the coefficient of volumetric expansion. The bulk modulus is defined as [4]

$$\mathcal{K}^{-1} = \sum_{\substack{v=1 \\ w=1}}^3 [C_{\epsilon\epsilon}^{-1}]_{vw}, \quad (1.70)$$

where v, w are Voigt indices. We recall that the program neglects the vibrational part of the elastic constants. [See Eqs. (1.62) and (1.63).] Hence, the calculated bulk modulus is based on the same approximation. The coefficient of volumetric expansion is given by [21]

$$\beta = \sum_{v=1}^3 \alpha_v, \quad (1.71)$$

where α_v are the Voigt components of the expansion tensor α defined as [21]

$$\alpha = \frac{d\epsilon}{dT} \quad (1.72)$$

Notice that the sums in Eqs. (1.70) and (1.71) are taken over the first three Voigt components only. Alternatively, the constant pressure heat capacity can also be calculated from the Grüneisen parameters and the heat capacity at constant volume. Details are given in Ref. 14. This approach is also implemented in PARAPOCS.

1.4 Appendix: Stress and strain

A body in which parts exerts a force on neighboring parts is said to be in a state of stress. The body is subject to a homogeneous stress if the forces acting on a surface element dS do not depend on the position of dS in the body. The forces are then only determined by the orientation of dS with respect to a fixed frame of reference. Consider now a homogeneous stressed body in which all parts are in static equilibrium, and imagine within this a cube of unit edge. This cube is then acted on by several forces due to the stress σ . The stress components $\sigma_{\alpha\beta}$ ($\alpha, \beta = 1, 2, 3$) are illustrated in Fig. 1.2.

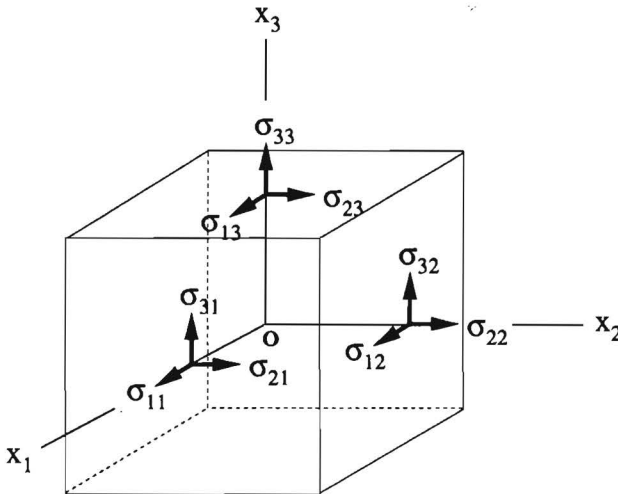


Figure 1.2. The (Cartesian) stress components $\sigma_{\alpha\beta}$. Cartesian axes are labeled by Ox_1 , Ox_2 and Ox_3 .

A stress component $\sigma_{\alpha\beta}$ is defined as the force along the $+\alpha$ direction (that is along Ox_α) transmitted across the face normal to Ox_β by the medium on the $+$ side of the face. Since the cube is assumed to be in static equilibrium, the moments about Ox_1 , Ox_2 and Ox_3 vanish. This gives $\sigma_{\alpha\beta} = \sigma_{\beta\alpha}$, i.e. the stress tensor is symmetric. In the case of inhomogeneous stress, the stress varies within the body and is specified at a given point \mathbf{r} by considering a small area dS around \mathbf{r} and then examining the force transmitted across it using the convention above. We notice that the (scalar) pressure P is defined by

$$P = -\frac{1}{3}(\sigma_{11} + \sigma_{22} + \sigma_{33}) \quad (1.73)$$

The stress components are often expressed as σ_v in Voigt's notation. [See Eq. (1.11).]

A body under a stress undergoes a deformation. This deformation is specified by the components $u_{\alpha\beta}$ of the infinitesimal strain tensor \mathbf{u} defined as

$$u_{\alpha\beta} = \frac{\partial u_\alpha}{\partial r_\beta}, \quad (1.74)$$

where \mathbf{u} denotes the displacement of the point \mathbf{r} around which the strain is examined. Observe that the strain components are dimensionless. The geometrical meaning of these components is as follows: Components u_{11} , u_{22} and u_{33} are the extensions per unit length parallel to Ox_1 , Ox_2 and Ox_3 , respectively. The component u_{12} is the rotation about Ox_3 towards Ox_1 of a line element parallel to Ox_2 . The component u_{21} is the rotation about Ox_3 towards Ox_2 of a line element parallel to Ox_1 . (See Fig 1.2.). The other components are defined similarly. When a homogeneous deformation is considered, all the components $u_{\alpha\beta}$ are constants and we may write:

$$u_\alpha = u_\alpha^0 + \sum_\beta u_{\alpha\beta} r_\beta, \quad (1.75)$$

where u_α^0 is the displacement of the origin corresponding to translation of the body. Equation (1.75) can be written as

$$u_\alpha = u_\alpha^0 + \sum_\beta \varpi_{\alpha\beta} r_\beta + \sum_\beta \epsilon_{\alpha\beta} r_\beta, \quad (1.76)$$

where $\varpi_{\alpha\beta}$ is the rotation of the body given by

$$\varpi_{\alpha\beta} = \frac{1}{2}(u_{\alpha\beta} - u_{\beta\alpha}), \quad (1.77)$$

and where $\epsilon_{\alpha\beta}$ is the bulk strain of the body given by

$$\epsilon_{\alpha\beta} = \frac{1}{2}(u_{\alpha\beta} + u_{\beta\alpha}). \quad (1.78)$$

The bulk strain is a measure for the distortion of a body, i.e. its deformation without rotation and translation. Equation (1.78) shows that the bulk strain matrix ϵ is symmetrical and that the geometrical meaning of the components $\epsilon_{\alpha\alpha}$ and $u_{\alpha\alpha}$ is identical. Hence, the volume V of a strained body is given by

$$V = V_0 |(\mathbf{I} + \epsilon)|, \quad (1.79)$$

where V_0 is the volume of the unstrained body. The off-diagonal components of ϵ are the shear strains. For the geometrical meaning of those strains we refer to the work of Nye *et al.* [15]. The bulk strain components are often expressed as ϵ_v by using the Voigt notation. [See Eq. (1.11).]

1.5 References

- [1] R.B. Sosman, *The phases of silica* (Rutgers University Press, New Brunswick, 1965).
- [2] W.M. Meier and D.H. Olson, *Atlas of zeolite structure types* (Butterworths, London 1987).
- [3] *Inclusion chemistry with zeolites: Nanoscale materials by design*, edited by N. Herron and D.R. Corbin (Kluwer academic publishers, Dordrecht, 1995).
- [4] A.J.M. de Man, PhD. thesis, Eindhoven University of Technology, Eindhoven (1992).
- [5] I. Petrovic, A. Navrotsky, M.E. Davis and S.I. Zones, *Chem. Mater.* **5**, 1805 (1993).
- [6] *Solid State Chemistry, Vol 2; Compounds*, edited by A.K. Cheetham and P. Day (University Press, Oxford, 1990).
- [7] P.A. Jacobs and J.A. Martens, *Synthesis of High Silica Alumino Silicate Zeolites* (Elsevier, Amsterdam, 1987).
- [8] C.R.A. Catlow and W.C. Mackrodt, *Computer simulations in physics, lecture notes in physics* (Springer, Vienna, 1982).
- [9] C.R.A. Catlow *Modeling of structure and reactivity in zeolites* (Academic Press, London, San Diego, 1992).
- [10] S.C. Parker and G.D. Price, *Advances in Solid-Sate Chem.* **1**, 295 (1989).
- [11] S.C. Parker, computercode: PARAPOCS, BATHPROGS (School of Chemistry, University of Bath, Claverton Down, Bath BA2 7AY, U.K.)
- [12] M. Born and K. Huang, *Dynamical Theory of Crystal Lattices, The international series of monographs on physics*, edited by D.H. Wilkinson and W. Marshall (Clarendon press, Oxford, 1968).
- [13] W. Cochran, *Crit. Rev. Solid State Sci.* **2**, 1 (1971).
- [14] C.R.A. Catlow and M.J. Norgett, *Lattice Structure and Stability of Ionic Materials*, private communication.
- [15] J.F. Nye, *Physical properties of crystals. Their representation by tensors and matrices* (Clarendon Press, Oxford, 1985).
- [16] D.A. McQuarrie, *Statistical Mechanics* (Harper and Row Publishers, New York, London, 1976)
- [17] M.J. Norgett and R. Fletcher, *J. Phys. C* **3**, 163 (1970).
- [18] G. Venkatamaran, L.A. Feldkamp and V.C. Sahni, *Dynamics of perfect crystals* (The MIT press, Cambridge, Massachusetts, London, 1975).
- [19] *Defects in solids, modern techniques*, edited by J.H. Harding, A.V. in Chadwick, and M. Terenzi (Plenum Press, New York 1976).
- [20] S.W. Kieffer, *Rev. Geophys. Space Phys.* **17**, 1 (1979).
- [21] T.H.K. Barron, J.G. Collins and G.K. White, *Adv. Phys.* **20**, 609 (1980).

Chapter 2

Ab initio approach to the development of interatomic potentials for the shell model of all-silica polymorphs

Abstract

We developed a new method for deriving parameters for the shell model of all-silica polymorphs. All parameters for the shell model are derived in a self-consistent way from *ab initio* energy surfaces, polarizabilities, and dipole moments of small clusters. This yields an *ab initio* partial-charge shell model potential. The predictive power of our potential is demonstrated by presenting predictions for the structure of α -quartz, α -cristobalite, coesite, and the vibrational spectrum and elastic constants of α -quartz which are compared with experiment and predictions of two widely used potentials.

2.1 Introduction

There has been a long history in attempts to derive interatomic potentials for all-silica polymorphs [1–9]. The most often employed models in the parametrizations are the rigid-ion [10,11] and the shell model [12,13,14]. Initially the parameters for both models were derived from experimental data, like crystal structure, infrared spectra and elastic constants of simple systems like α -quartz. The applicability of those potentials based on experimental data turned out to be of limited value for properties not used explicitly in the parametrization [15–18]. To obtain a potential which has no bias due to the incorporation of experimental data, attempts have been made to develop parametrization schemes for a rigid-ion model based on information which is obtained from *ab initio* energy surfaces of small clusters [2,7,8,9]. In most cases it appeared that the atomic charges could not be derived from *ab initio* potential energy surfaces of small clusters and that additional experimental data was required to determine the ion charges [2,7,9]. Kramer *et al.* [2] derived a rigid-ion model potential from *ab initio* potential energy surfaces of small clusters, and showed that this potential does not predict the correct symmetry of α -quartz. They concluded that incorporation of additional crystal data in the fit procedure was mandatory to obtain a potential for all-silica polymorphs, and presented a potential fitted on both *ab initio* data and experimental data on the structure and elastic tensor of α -quartz [2].

On basis of the above considerations, and because it is attractive from a methodological point of view, we have investigated whether an *ab initio* potential can be derived by:

- using the shell model which describes, by incorporation of polarization effects, the electrostatic interactions more accurately than the rigid-ion model;
- using *both* *ab initio* potential energy surfaces and *ab initio* electrostatic data (to determine the charges) in the fit procedure.

We have used the above approach and we will show that we have derived a fully *ab initio* potential based on the shell model and *ab initio* potential energy surfaces, polarizabilities and dipoles of small clusters. By presenting this derivation we also show that incorporation of crystal data in the fit procedure, as used to be the approach in previous parametrization schemes [1,2,7,9], is no longer needed in our approach. The performance of our potential will be illustrated by presenting predictions for the structures of α -quartz, α -cristobalite and coesite. Also, predictions for the vibrational spectrum (Raman and infrared) and the elastic constants of α -quartz will be given. The results will be compared to predictions of the shell model potential of Catlow *et al.* [1], which is a modified version of the Sanders potential [19] and based on empirical data of α -quartz. Also, a comparison with the previously mentioned rigid-ion model potential of Kramer *et al.* will be made. The potential of Catlow *et al.* and Kramer *et al.* will be referred to as the JC and the KFBS potential, respectively.

2.2 Method

In our approach all potential parameters are derived from *ab initio* energy surfaces, polarizabilities and dipole moments of small clusters. This procedure will be explained in several steps. We will introduce the clusters, the analytical form of the shell model potential used in our procedure, and the method to derive the covalent parameters and the charges from *ab initio* potential energy surfaces and *ab initio* electrostatic data, respectively.

2.2.1 Clusters

The clusters employed in our procedure are $\text{Si}(\text{OH})_4$ and $(\text{HO})_3\text{SiOSi}(\text{OH})_3$ for reasons that are explained below. These clusters will be referred to as the monomer and the dimer, respectively. The Si and H atoms in the clusters are considered as nonpolarizable. The O atom is described as polarizable with a charged core and a massless charged shell, which are connected by a harmonic spring, in accordance with the shell model.

2.2.2 Interatomic potential

In line with previous work on all-silica polymorphs [1] we adopt a two-body energy function of the form:

$$E^{pot} = \sum_{\substack{i,j \\ i < j}} [A_{ij} \exp\left(\frac{-r_{ij}}{\rho_{ij}}\right) - \frac{C_{ij}}{r_{ij}^6}] + \sum_{\substack{i,j \\ i < j}} \frac{q_i q_j}{r_{ij}} + \frac{1}{2} \sum_i k(r_{i,shell} - r_{i,core})^2 \quad (2.1)$$

The first and second term in Eq. (2.1) constitute the well-known Buckingham form. The O-O interaction only acts through the shells, the Si-O interaction acts between the O shell and the Si ion. The fourth term is the harmonic interaction, which acts between core and shell of the same O atom. The Coulomb term includes all electrostatic interactions between cores, between shells, and cores and shells belonging to different ions.

2.2.3 Parametrization method

Fits of all parameters in Eq.(2.1) on potential energy surfaces of the monomers gave fits with the same error for several combinations of the spring constant, the atomic and the shell charges. A similar redundancy has been reported before for the rigid-ion model [2,7]. Instead of taking experimental data, as used to be the approach [1,2,7], we used *ab initio* dipole moments and polarizabilities to determine the charges. To derive both the Buckingham parameters and values for the atomic and shell charges we have developed a two-step procedure. As these steps are interdependent they are done iteratively. Both steps will be discussed in more detail below

2.2.4 Derivation of short range parameters

For the derivations of the short range parameter set we have used two *ab initio* energy surfaces of the monomers. One potential energy surface is obtained by symmetric stretching of the Si-O bonds in the monomer from 1.35 Å with steps of 0.05 Å to 2.00 Å (14 configurations) for a fixed O-Si-O angle (109.7°), a fixed O-H distance (0.947 Å), and a fixed Si-O-H angle (119.5°), keeping the Si and O atoms in T_d symmetry. The second potential energy surface is made by varying two opposite O-Si-O angles from 70° with steps of 5° to 150° (17 configurations) for a fixed Si-O distance (1.629 Å), a fixed O-H distance (0.947 Å), and a fixed Si-O-H angle (119.5°), keeping the Si and O atoms in D_{2h} symmetry. These potential energy surfaces will further on be referred to as the stretching and bending potential energy surface, respectively. The potential surfaces are calculated

with Møller-Plesset second-order perturbation theory (MP2) using the code GAUSSIAN [20]. The basis sets used are 6-31G(d) on Si, 6-311G(d) on O and 6-31G(p) on H.

The choice of these potential surface allows almost separate fit procedures for the Si-O and O-O interaction. The Si-O interaction is fitted on the stretching potential energy surface, where the O-O distance changes little. The O-O parameters are obtained from the bending potential energy surface where the Si-O distance is constant. This enables us to keep the Si-O parameters fixed. As the parameter sets for the Si-O and O-O interaction are not completely independent, both fits are done iteratively. with a least squares procedure, using the code PARFIT [21]. During the fit the shell positions are determined by minimizing the energy in the cluster with respect to the shell positions [22], which is done by our own code SHELLMIN. During the fit procedure we have applied a potential between the shells of O atoms and neighboring hydrogens, which is chosen such that the shell moves in the plane bisecting the H-O-Si angle, to mimic the situation in the crystal where each O atom connects two SiO₄ tetrahedra, that produce equal forces on the shell. In this step the atomic charges, shell charges and spring constant are fixed. The Buckingham parameters obtained will be used for determination of the charges in the second step.

2.2.5 Derivation of charges

We employed the dimer clusters to determine the shell charges from the *ab initio* polarizability tensors and the atomic charges from the dipole moments. The monomers are not suitable because in these clusters the motion of the shell, which simulates the atomic polarization and thereby governs the fit on the polarizabilities, is strongly influenced by the neighboring H atoms. This side effect is diminished in the dimers which contain an O atom with only Si atoms as neighbors. However, for larger clusters less accurate *ab initio* calculations can be done. *Ab initio* calculations are done for three configurations of the dimer. In these configurations the Si-O-Si angle has the values 130°, 140° and 150° and the Si-O and the O-H distances are kept fixed (Si-O 1.65 Å, O-H 0.974 Å). The *ab initio* dipole and the polarizability tensor were calculated for each configuration with SCF because MP2 was too time consuming. The basis functions used are the same as those in the MP2 calculations. We expect that MP2 calculations of the dipoles and polarizabilities would give slightly lower values for the dipole and higher values for the polarizability than SCF. (For example, an optimization for H₂O with a 6-311G(d,p) basis set done with both methods gives an MP2 dipole which is 5% lower than the SCF result and MP2 polarizability tensor elements that are 10% higher on the average.)

To obtain the charges, the potential given by Eq. (2.1) with the Buckingham parameters obtained in the previous step and fixed values of the remaining parameters were transferred to the dimer clusters. The charges are then determined as follows: For a fixed geometry of the dimer clusters, the polarizability is caused by displacements of the shells only. By comparing the variations of the dipole moments in the shell model and in an SCF calculation for each cluster, using a finite field method, the shell charge was determined. The atomic charges were subsequently determined by fitting on the dipole moment in zero field. In both procedures the charges are derived from fits on the *ab initio* data of the dimer clusters that were mentioned before. The fittings are done with the linear least squares technique implemented in our own code CHARGEFIT. For the relations used in

these fit the following assumptions have been made:

- all atoms of the same type in the clusters have the same atomic charge, irrespective of their positions;
- all shells of the O atoms in the dimer have the same spring constant and charge;
- the ratio of the atomic charges, is fixed to $q_{Si} = -2q_O = 4q_H$, in order to keep the cluster and the crystal to which the potential must be transferred, neutral.

We thus have an iterative cycle which consists of four separate fit procedures; a fit to determine the Si-O interaction from the stretching potential energy surface of the monomer, a fit to determine the O-O interaction from the bending potential energy surface of the monomer, a fit to derive the shell charge from the *ab initio* polarizability of the dimers, and a fit of the atomic charges on the *ab initio* dipole moments of the dimers. These fits are combined with a procedure to determine the shell positions in the clusters. All procedures are performed iteratively to yield a parameter set which fits in a self consistent way the *ab initio* data employed. The fit procedure is illustrated in Fig. 2.1. In our procedure all parameters, except the harmonic spring constant k , are directly derived from *ab initio* data. The value of k is determined by the value which gives the smallest possible errors in the fit procedures.

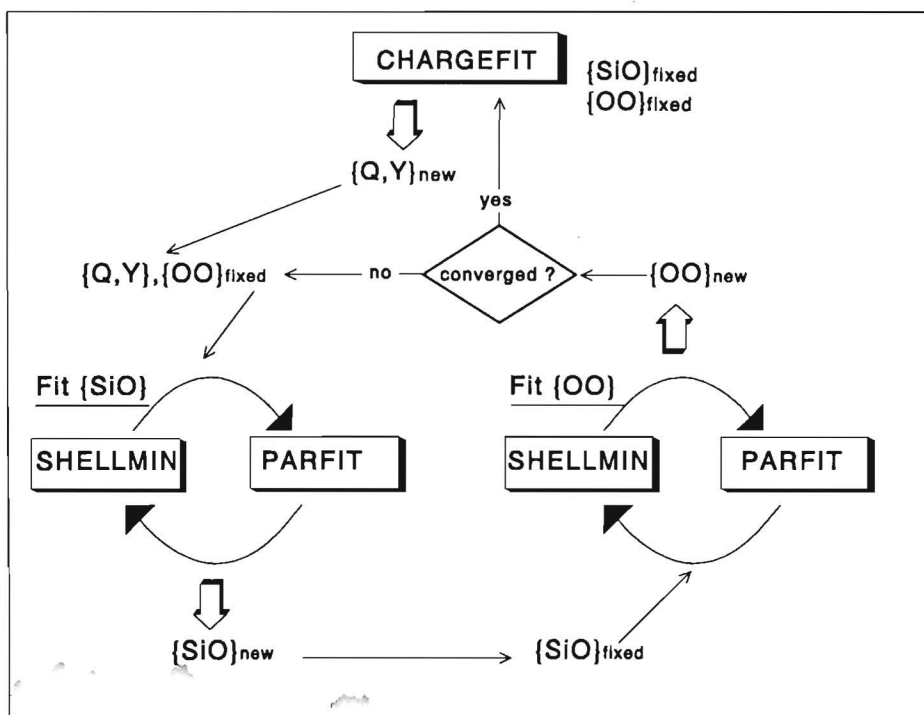


Figure 2.1. Fit procedure. $\{O, O\}$ denotes the parameter set of the O-O interaction and $\{Si, O\}$ that of the Si-O interaction. $\{Y, Q\}$ denotes the electrostatic parameter set, with Y the shell charge and Q the atomic charge.

The accuracy of the obtained potential is tested by calculating the structure and the Vibrational spectrum of α -quartz, coesite and α -cristobalite. The structures are calculated by energy minimization starting from experimental structures [23–26,28]. This relaxation is performed by the THBREL code [27]. This code also generates the elastic constant tensor (elastic stiffness tensor) and the high and low frequency dielectric tensor. Using the relaxed structure and the interatomic potential, the vibrational spectra are calculated with the THBPHON code [29]. The spectra serve as a check on the stability of the structures. [30]. The structure predictions for α -quartz, α -cristobalite, coesite and predictions for the vibrational spectrum and the elastic constants of α -quartz will be compared with experiment and predictions of the JC and KFBS potential.

2.3 Results

At first we notice that the calculated Mulliken charges on the dimers differ much from the charges obtained with our procedure. Table 2.1 shows the Mulliken charges and those obtained with our procedure.

Table 2.1. Mulliken charges, calculated with SCF, for the dimer with an Si-O-Si angle of 140° . Resulting charges of our parametrisation: $q_{Si} = 2.7226$, $q_{O_s} = -2.0125$ and $q_{O_c} = 0.6512$. (q_{O_s} denotes the shell charge of the O atom and q_{O_c} denotes the core charge.)

atom	charge	atom	charge
q_{Si}	1.486	q_{O_s}	-0.638
q_{O_1}	-0.774	q_{H_1}	0.273
q_{O_2}	-0.630	q_{H_2}	0.267

To determine the k value we optimized parameter sets for a range of k values and evaluated the errors of the four fit procedures with respect to k . This gave the following results:

- errors of the fits on the monomer bending and stretching potential energy surfaces behave like decreasing asymptotic functions with increasing k ;
- the error of the fit on the polarizability tensor behaves like a decreasing asymptotic function with increasing k ;
- the error of the fit on the permanent dipole moments, is a function of k that has a single sharp minimum at $k = 34.89 \text{ eV } \text{\AA}^{-2}$.

The error in the fit on the stretch potential energy surface is higher than that in the fit on the bending potential energy surface at any k . The asymptotic behavior of the errors of the first two fits indicate that for the physical quantities used in the fit, the point dipole model is more appropriate than a model where the shell has a finite displacement. However, the errors for these fits are also reasonable small for $k = 34.89 \text{ eV } \text{\AA}^{-2}$. (See below.) Moreover, the errors are largely determined by the largest and smallest distances and angles in the fits. Because of the last fit we selected the parameter set with $k = 34.89 \text{ eV}$ and used this set for the calculations presented in all the tables and the figure. Table 2.2 gives the parameter set and the errors in the fits. The potential with the above parameters will be referred to as the BJS I potential. Note that there is no dispersion interaction ($C=0$). The electrostatic interaction completely swamps the dispersion in the first fit.

Table 2.2. Our parameter set for the shell model, $q_{Si}=2.7226$, $q_{O_s}=-2.0125$ and $q_{O_c}=0.6512$. Errors in fits on the stretch and the bending potential energy surface are 0.28 eV and 0.11 eV, respectively. The error in the shell charge is $8.9 \cdot 10^{-5}$. The error in the atomic charge is $3.15 \cdot 10^{-3}$.

	$A(\text{eV})$	$\rho(\text{\AA})$	$C(\text{eV}\text{\AA}^6)$	$k(\text{eV}\text{\AA}^{-2})$
$O_s - O_s$	266757.0	0.173411	0.0	-
$Si - O_s$	18122.0	0.17077	0.0	-
$O_c - O_s$	-	-	-	34.98

Results of the structure calculations are shown in Tables 2.3 and 2.4. The predictions of the BJS I potential for α -quartz are reasonable, even though no empirical data has been used whatsoever. Especially, the predicted elastic tensor elements are in good agreement with experiment; some are even closer to experiment than the predictions of both other potentials.

Table 2.3. Predicted and experimental [23,24] properties of α -quartz. Symbols l and s refer to the largest and smallest distance, respectively. Lengths are in \AA and angles in degrees. Elastic constants C_{ij} are in 10^{10}N/m^2 . Low-frequency dielectric constants are denoted as ϵ_{ij}^0 and high-frequency dielectric constants as ϵ_{ij}^∞ .

Property	Expt.	BJS I	KFBS	JC
a	4.913	4.751	4.941	4.836
c	5.405	5.213	5.449	5.347
u	0.469	0.460	0.465	0.464
x	0.415	0.395	0.427	0.408
y	0.272	0.288	0.272	0.278
z	0.120	0.094	0.124	0.108
d_{Si-O_s}	1.614	1.621	1.598	1.610
d_{Si-O_l}	1.605	1.623	1.605	1.614
γ	120.0	120.0	120.0	120.0
$\angle_{Si-O-Si}$	143.7	131.9	148.5	139.1
C_{11}	8.68	8.85	9.06	9.47
C_{12}	0.70	1.67	0.81	1.84
C_{13}	1.91	1.15	1.53	1.97
C_{14}	-1.80	-1.73	-1.77	-1.45
C_{33}	10.58	11.26	10.70	11.61
C_{44}	5.82	5.46	5.03	5.00
C_{66}	3.99	3.59	4.12	3.81
ϵ_{11}^0	4.45	2.42	1.95	4.74
ϵ_{33}^0	4.81	2.46	1.99	5.01
ϵ_{11}^∞	2.36	1.81	-	2.12
ϵ_{33}^∞	2.36	1.82	-	2.14

A large error is found for the Si-O-Si angle. This is understandable. We have fitted to the potential energy surface of the monomer but not (yet) of the dimer so that there is no good effective bending interaction. A fit on the bending potential energy surface might remedy the defect. As no experimental data is used to obtain the BJS I potential, it should have a higher transferability to other systems than the JC and KFBS potential. This is not yet apparent from the results of α -cristobalite. This may be due again to the incorrect Si-O-Si angle. However, for coesite the BJS I potential performs as well as for α -quartz and α -cristobalite, whereas the KFBS potential and JC potential become less accurate for this material.

Table 2.4. Predicted and experimental properties of all-silica polymorphs. References denote experiment. Lengths are in Å and angles in degrees.

Property	Expt.	BJS I	KFBS	JC
α -cristobalite [25]				
a	4.978	4.860	4.920	4.971
c	6.948	6.718	6.602	7.010
u	0.300	0.305	0.331	0.294
x	0.246	0.234	0.245	0.240
y	0.100	0.125	0.119	0.097
z	0.175	0.195	0.189	0.177
$d_{\text{Si-O}_e}$	1.605	1.613	1.608	1.600
$d_{\text{Si-O}_i}$	1.613	1.614	1.595	1.602
$\angle_{\text{Si-O-Si}}$	146.8	136.8	143.9	147.1
coesite [26]				
a	7.136	6.832	7.138	6.805
b	12.369	12.138	12.493	12.291
c	7.174	7.019	7.271	7.115
$\langle d_{\text{Si-O}} \rangle$	1.611	1.612	1.601	1.607
β	120.0	120.03	120.7	119.5
$\langle \angle_{\text{Si-O-Si}} \rangle \dagger$	143.6	134.2	150.5	138.7

† Averaged over angles that are not equal to 180°

Figure 2.2 shows calculated and experimental [31] infrared and Raman spectra of α -quartz. The JC potential gives a good prediction of the low frequencies while the KFBS potential does this for the high frequencies. Our potential gives a reasonable prediction of both the high and the low frequency region. The BJS I predictions for the vibrational spectrum of α -quartz are almost as accurate as the predictions based on the potential of de Vos et al. [4], although the latter potential is fitted on experimental infrared data of α -quartz.

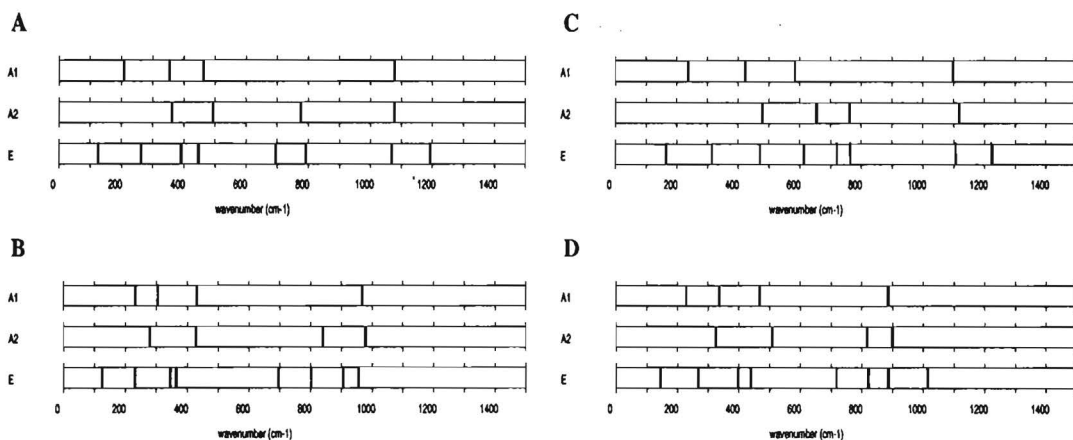


Figure 2.2. Calculated and experimental vibrational spectrum of α -quartz. The A1 modes are Raman active, the A2 modes infrared active and the E modes are both Raman and infrared active. A: Experiment. B: BJS I prediction. C: KFBS prediction. D: JC prediction.

2.4 Conclusions

We have developed a method to derive potential parameters for the shell model of all-silica polymorphs from *ab initio* potential energy surfaces, polarizabilities and dipole moments of small clusters. This approach leads to an *ab initio* partial charge shell model potential. By including both *ab initio* potential energy surfaces and *ab initio* electrostatic data in our fit procedures, we have introduced a method with a well defined balance between covalent and electrostatic interactions. By presenting this derivation we have also proven that inclusion of crystal data (either experimental or theoretical) in the fit procedure is not needed to derive the charges and to obtain a reasonable potential for all-silica polymorphs. This contradicts the conclusion of previous work based on the rigid-ion approach [2,7,9]. We also conclude that our method needs further improvement, because for three structures considered, the BJS I potential underestimates the Si-O-Si angle. We think that this indicates the lack of an appropriate (*ab initio*) Si-O-Si bending term in our model. Notwithstanding this limitation, the predictions of the BJS I potential for the vibrational spectrum of α -quartz, provide an improvement over those of the JC and KFBS potential.

2.5 References

- [1] R.A. Jackson and C.R.A. Catlow, *Mol. Simul.* **1**, 207 (1988).
- [2] G.J. Kramer, N.P. Farragher, B.W.H. van Beest and R. A. van Santen, *Phys. Rev. B* **43**, 5068 (1991).
- [3] B. Vessal, M. Amini and C.R.A. Catlow, *Mol. Simul.* **5**, 1 (1990).
- [4] E. de Vos Burchart, H. van Bekkum and B. van de Graaf, *J. Chem. Soc. Faraday Trans.* **88**, 1161 (1992).
- [5] C.S. Vempati and P.W.M Jacobs, *Radiation Effects.* **73**, 285 (1983).
- [6] J.B. Nicolas, A.J. Hopfinger, F.R. Trouw and L.E. Iton, *J. Am. Chem. Soc.* **113**, 4792 (1991).
- [7] S. Tsuneyuki, M. Tsukada, H. Aoki and Y. Matsui, *Phys. Rev. Lett.* **61**, 4792 (1988).
- [8] A.C. Lasaga and G.V. Gibbs, *Phys. Chem. Minerals* **14**, 107 (1987).
- [9] A.C. Lasaga and G.V. Gibbs, *Phys. Chem. Minerals* **16**, 28 (1988).
- [10] E.W. Kellerman, *Phil. Trans. Roy. Soc. London* **A238**, 513 (1940).
- [11] W. Cochran, *Crit. Rev. Solid State Sci.* **2**, 1 (1971).
- [12] B.G. Dick Jr. and A.W. Overhauser, *Phys. Rev.* **112**, 90 (1958).
- [13] W. Cochran, *Phys. Rev. Lett.* **2**, 495 (1959).
- [14] S. K. Sinha, *Crit. Rev. Solid State Sci. (USA)* **3**, (No. 3) 273 (1973).
- [15] A.J.M. de Man, PhD Thesis, Eindhoven University of Technology, Eindhoven (1992).
- [16] A.J.M. de Man, B.W.H. van Beest, M. Leslie and R.A. van Santen, *J. Phys. Chem.* **94**, 2524 (1990).
- [17] J.D. Gale and A.K. Cheetham, *Zeolites* **12**, 674 (1992).
- [18] J.S. Tse and D.D. Klug, *J. Chem. Phys.* **95**, 9176 (1991).
- [19] M. Sanders, M. Leslie and C.R.A. Catlow, *J. Chem. Soc., Chem. Commun.* 1271 (1984).
- [20] Gaussian 90, Revision I, M. J. Frisch, M. Head-Gordon, G. W. Trucks, J. B. Foresman, H. B. Schlegel, K. Raghavachari, M. Robb, J. S. Binkley, C. Gonzalez, D. J. Defrees, D. J. Fox, R. A. Whiteside, R. Seeger, C. F. Melius, J. Baker, R. L. Martin, L. R. Kahn, J. J. P. Stewart, S. Topiol, and J. A. Pople, Gaussian, Inc., Pittsburgh PA, (1990).
- [21] B.W.H. van Beest, private communication
- [22] G. Venkatamaran, L.A. Feldkamp and V.C. Sahni, *Dynamics of perfect crystals* (The MIT press, Cambridge, Massachusetts, London, 1975).
- [23] C.T. Levien and D.E. Weidner, *Am. Mineral.* **65**, 920 (1980).
- [24] H.J. Mc Skimin, P. Andreat and R.N. Thurston, *J. Appl Phys.* **36**, 1624 (1965).
- [25] D.R. Peacor, *Z. Kristallogr.* **138**, 274 (1973).
- [26] K.L. Geisinger, M.A. Spackman and G.V. Gibbs, *J. Phys. Chem.* **91**, 3237 (1987).
- [27] C.R.A. Catlow and W.C. Mackrodt, *Computer simulations in physics, lecture notes in physics* (Springer, Vienna, 1982); C.R.A. Catlow, M. Doherty, G.D. Price, M.J. Sanders and S.C. Parker, *Mater. Sci. Forum* **7**, 163 (1986); author of THBREL: M. Leslie, Science and Engineering Research Council, Daresbury Laboratory, U.K.
- [28] L.W. Finger and R.M. Hazen, *Acta. Crys.* **B47**, 561 (1991).
- [29] G. Dolling, *Calculations of phonon frequencies in: Methods in computational physics vol. 15* (Academic Press, New York, 1976); author of THBPHON: M. Leslie, Science and Engineering Research Council, Daresbury Laboratory, U.K.
- [30] A.J.M. de Man, H.K. Küppers and R.A. van Santen, *J. Phys. Chem.* **96**, 2092 (1992).
- [31] J. Etchepare, M. Merian and L. Smetankine, *J. Chem. Phys.* **60**, 1873 (1974).

Chapter 3

Physical properties of α -quartz at variable pressures and temperatures

Abstract

The reliability of two shell model potentials and a rigid-ion model potential has been investigated by comparing available experimental data with predicted values for a large number of α -quartz properties at variable temperatures and pressures. Calculations were performed with a recently developed free energy minimization code. Predictions for the structure, Raman modes and elastic constants of α -quartz at elevated temperatures and pressures are discussed. Calculations of the constant pressure entropy and heat capacity as a function of temperature are presented. Calculated low-frequency phonon dispersion curves in the $[\xi \xi 0]$, $[\xi 0 0]$ and $[0 0 \xi]$ direction are also discussed. Analysis of these predictions shows which atomic interactions are most accurately described by each potential. Furthermore, the conditions are discussed under which the predictions of each potential are the most reliable.

3.1 Introduction

From a technological point of view, silicon dioxide is an interesting material. It is used in many electronic devices, as well as in the ceramic industry and the synthesis of zeolites. Zeolites are microporous materials that, in general, have complex structures. These materials are mainly used as detergents and catalysts in many industrial processes. Therefore, a large number of approaches has been developed to predict all-silica structures and their properties. These approaches range from *ab initio* quantum mechanical calculations [1–9] to those based on interatomic potentials [10–13]. Although *ab initio* calculations give more accurate results than the semi-empirical potentials reported so far [4–7], they are computationally expensive. Intrinsic complexity of a crystalline solid, i.e., a low symmetry or a large unit cell, can make an *ab initio* calculation computationally intractable [4]. The use of interatomic potentials might then be desirable, provided that they are sufficiently accurate. Therefore, the development of reliable interatomic potentials, especially those derived from *ab initio* data, is a subject of interest. It is also useful to know how reliable the interatomic potentials are under different conditions.

In this work, we have investigated the reliability of a recently derived *ab initio* shell model potential [10] and two other interatomic potentials [11,12]. This is done by making detailed comparisons between predicted and experimental values for a large number of α -quartz properties at variable temperatures and pressures. Calculations were performed with the free energy minimization code PARAPOCS [14]. We will discuss predictions for the structure, Raman modes and elastic constants of α -quartz at elevated temperatures and pressures. We will consider predictions for the temperature dependence of the constant-pressure entropy and heat capacity of α -quartz. Calculated low-frequency phonon dispersion curves in the $[\xi \xi 0]$, $[\xi 0 0]$ and $[0 0 \xi]$ direction will also be discussed. Analysis of these predictions will demonstrate which atomic interactions are the most accurately described by each potential. We will further indicate under which conditions the predictions of each potential are the most reliable.

3.2 Computational details

Free energy minimizations were done with the code PARAPOCS [14] which can be used to calculate physical properties of solids at variable temperatures and pressures. To calculate thermodynamical properties, the vibrational frequencies of the solid must be computed. The calculations assume that vibrational motions in the solid are described by collective harmonic oscillators. The frequency of those oscillators varies with cell volume [25]. Minimization of the Gibbs free energy can be achieved by varying the cell volume and the positions of the ions until the configuration satisfies the following equilibrium conditions at a given temperature and pressure:

$$\frac{\partial F}{\partial V} = P_{app}, \quad (3.1)$$

$$\frac{\partial U_{stat}}{\partial \mathbf{r}} = 0. \quad (3.2)$$

In Eq. (3.1) F denotes the Helmholtz free energy, V the cell volume and P_{app} the applied pressure. In Eq. (3.2) U_{stat} denotes the static energy due to the interatomic interactions and \mathbf{r} denotes the atomic coordinates. Equation (3.1) states that the pressure exerted by the system (internal pressure) must equal the applied pressure. [Equation (3.1) is only valid for cubic crystals. For more general cases the derivatives of the Helmholtz free energy with respect to the strain must be computed. Details can be found in Ref. 20.] Equation (3.2) states that the net force on each atom must vanish. After the Gibbs free energy is minimized, thermodynamical properties, elastic constants, dielectric constants and the structure of the solid can be computed. Calculation of the Helmholtz free energy and other thermodynamical properties requires computation of the vibrational frequencies for all wave vectors in the Brillouin-zone. Those frequencies are calculated with an appropriate wave vector grid. (See the Appendix.)

In our calculations we have employed the recently derived *ab initio* shell model potential of de Boer *et al.* [10] denoted as the BJS I potential. We have used the shell model potential published by Catlow *et al.* [11] and the rigid-ion model potential derived by Kramer *et al.* [12]. The latter potentials are referred to as the JC and KFBS potential, respectively. Cutoffs applied in calculations using the KFBS and JC potential are 10 Å [27]. The covalent O-O interactions of the BJS I potential are applied with a cutoff of 3.5 Å, because for larger distances all covalent terms are effectively zero. The covalent Si-O interaction of this potential is applied with a cutoff of 2.5 Å (i.e., in between the nearest and next nearest Si and O neighbors) to simulate a real Si-O bond. The electrostatic interactions are calculated using the Ewald summation.

3.3 Properties of α -quartz at variable pressures

3.3.1 Pressure-induced changes of the α -quartz structure

We will first review the pressure-induced geometrical changes of α -quartz that are known from experiment [30–33]. These changes and their correlations are important in our subsequent discussion. Compression of α -quartz is mainly governed by changes in the bond angles because the Si-O bond distances remain virtually constant at variable pressures [30–33]. Therefore, we will concentrate on changes of the bond angles with pressure. Figure 3.1 shows the experimental structure of α -quartz at $P = 10.2$ GPa.

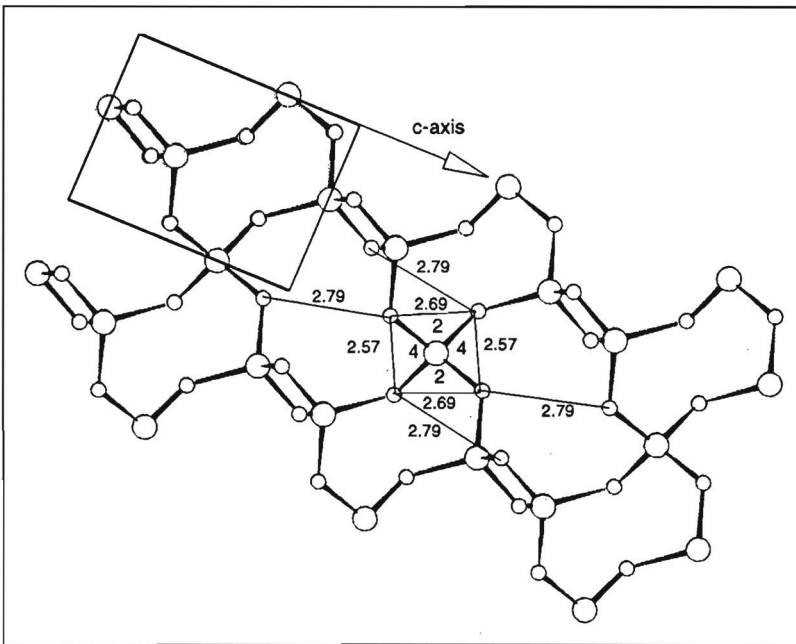


Figure 3.1. Intra-tetrahedral distances, OO_s distances, and tetrahedral angles in the experimental structure of α -quartz at $P = 10.2$ GPa [33] viewed along the a -axis. Distances of 2.79 Å are the OO_s distances. Numbering of the tetrahedral angles corresponds to that in Fig. 3.4. Numbers 2 and 4 denote tetrahedral angles in the plane of drawing.

At low pressure, the compression of α -quartz is governed by decrease of the weak Si-O-Si bond angle, together with rotation of the tetrahedra along their twofold axis perpendicular to the c -axis [30–33]. The pressure-induced decrease of the Si-O-Si bond angle and that of the smallest intertetrahedral distance are correlated. This distance will be referred to as the OO_s distance. Decreased OO_s distances cause increased O-O repulsions. (See Fig. 3.1.) The increased O-O repulsions cause distortion of the tetrahedral O-Si-O bond angles. The tetrahedral bond angles do not change much at low pressures, because they are more rigid than the Si-O-Si bond angles [30–33]. The tetrahedral bond angles become gradually more distorted when pressure is increased. The decrease of the Si-O-Si bond

angle becomes less pronounced at higher pressures. The tetrahedral bond angle distortion is therefore mainly responsible for the compression of α -quartz at high pressures. Unit cell compression of α -quartz is directly related with compression of the intertetrahedral distances, which are themselves related to compression of the bond angles [30]. The c -axis compression is correlated with changes of the OO_s distance, because this distance has the largest component parallel to the c -axis [33]. The c -axis compression is via the OO_s distance correlated to compression of the Si-O-Si bond angle. Compression of the a -axis is correlated with that of the OO_l distance (the largest intertetrahedral distance) because one of these two distances is nearly parallel to the a -axis. The other is approximately 45° between a and c [31]. Calculated and experimental α -quartz structures at ambient conditions are given in Table 3.1.

Table 3.1. Predictions for the structure of α -quartz at $T = 300$ K compared with experiment [43]. Distances are in \AA and angles in degrees. The symbols l and s refer to the largest and smallest distance, respectively.

	Expt.	BJS I	KFBS	JC
a	4.914	4.772	4.963	4.855
c	5.405	5.232	5.468	5.362
γ	120.0	120.0	120.0	120.0
d_{Si-O_l}	1.614	1.623	1.606	1.614
d_{Si-O_s}	1.606	1.620	1.598	1.607
$\angle_{Si-O-Si}$	143.6	132.8	149.6	140.0
\angle_{O-Si-O_1}	109.3	108.9	110.4	109.5
\angle_{O-Si-O_2}	110.5	112.8	107.7	111.2
\angle_{O-Si-O_3}	108.9	104.4	114.9	108.2
\angle_{O-Si-O_4}	108.8	108.9	108.1	108.4
Symmetry	$P3_121$	$P3_121$	$P3_121$	$P3_121$

Table 3.2 presents predictions for the Si-O bond distances in α -quartz at variable pressures. All potentials predict that the Si-O bond distances in α -quartz change slightly with pressure, which is in accordance with experiment.

Table 3.2. Predictions for Si-O bond distances in α -quartz versus pressure at $T = 300$ K, compared with experiment [33]. P denotes pressure, r_l the longest Si-O bond distance and r_s the shortest Si-O bond distance. Distances are in \AA and pressures in GPa. Distances in the third row are the predicted values at pressures which induce acoustic mode softening.

	Expt.		BJS I		KFBS		JC	
P	r_l	r_s	r_l	r_s	r_l	r_s	r_l	r_s
0.0	1.614	1.606	1.623	1.620	1.606	1.598	1.614	1.607
9.5	1.621	1.596	1.639	1.639	1.598	1.580	1.627	1.605
—	—	—	1.652	1.639	1.594	1.570	1.627	1.605

Hence, we will focus on predictions of the bond angle compression. Furthermore, all results

are obtained for pressures up to the value at which each potential predicts acoustic mode softening. This will be further discussed in Sec. 3.3.2. Calculated and experimental [30,32,33] values for the compression of the Si-O-Si bond angle and c -axis are shown in Figs. 3.2 and 3.3.

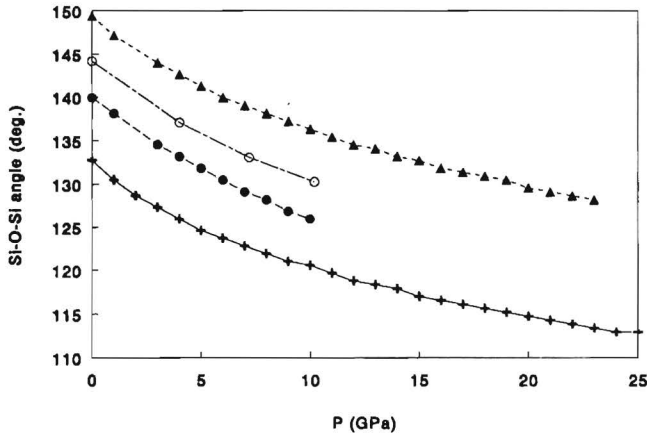


Figure 3.2. Predictions for the Si-O-Si bond angle in α -quartz versus pressure, compared with experimental data of Glinneman et al. [33]. Crosses: BJS I predictions. Closed triangles: KFBS predictions. Closed points: JC predictions. Open points: data of Glinneman et al. [33].

Although the JC-predicted α -quartz structure at ambient conditions is the closest to experiment, this potential slightly underestimates the Si-O-Si bond angle at any pressure. Predictions of the JC potential for the Si-O-Si bond angle, OO_s distance and c -axis at low pressures are in agreement with the experimental correlation mentioned earlier.

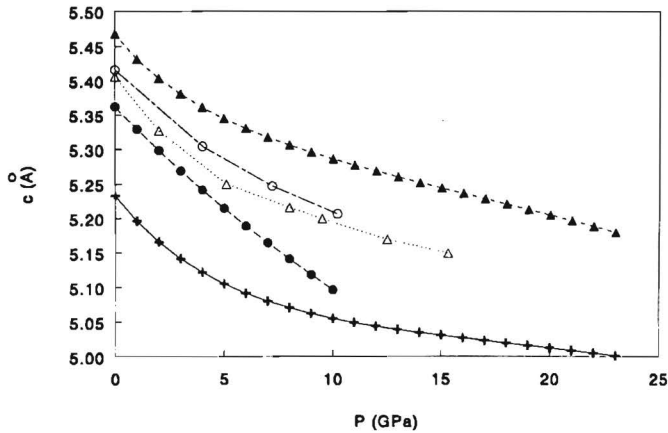


Figure 3.3. Predictions for the c -axis in α -quartz versus pressure, compared with experimental data of Hazen et al. [30] and Glinneman et al. [33]. Crosses: BJS I predictions. Closed triangles: KFBS predictions. Closed points: JC predictions. Open triangles: data of Hazen et al. [30]. Open points: data of Glinneman et al. [33].

The JC-predicted OO_s distance follows a trend similar to that of the c -axis with pressure.

Hence, the underestimation of the OO_s distance at low pressures might be caused by: underestimation of the Si-O-Si bond angle; insufficient O-O repulsions; or a combination of both. To investigate this, we have studied pressure-induced changes of the a -axis, OO_l distance and O-Si-O bond angles. As explained above, those properties are virtually independent of the Si-O-Si bond angle. The JC predictions of the OO_l distance and a -axis versus pressure reproduce the experimental curve. (The latter quantities are underestimated by 4% and 1%, respectively.) Thus, the O-O interactions at longer interatomic distances are reasonably described. Figure 3.4 illustrates calculated and experimental values for the tetrahedral bond angles at variable pressures.

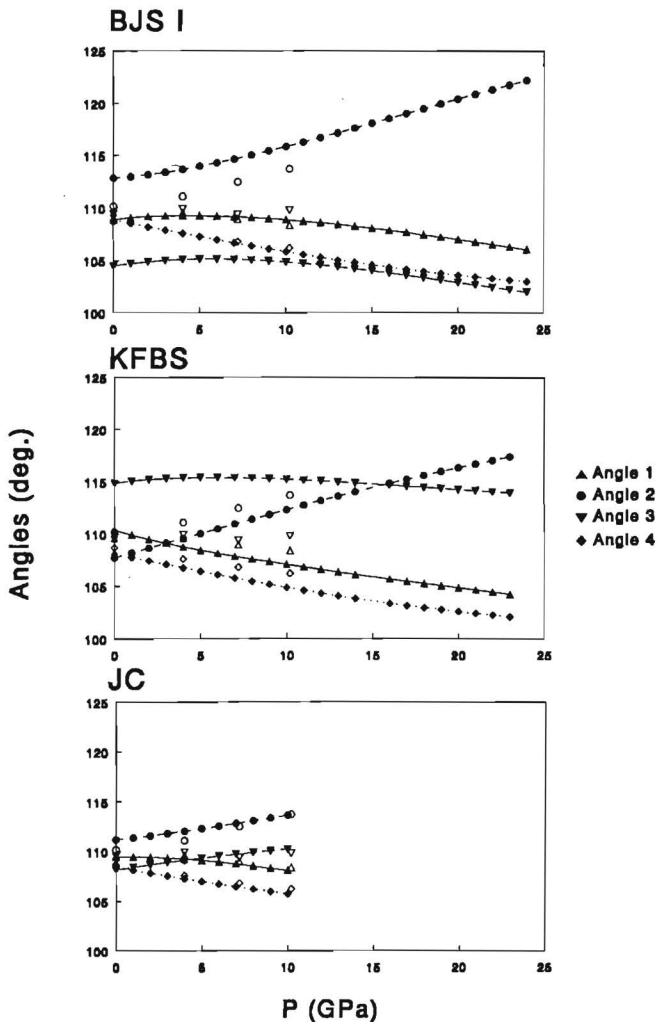


Figure 3.4. Predictions for the tetrahedral angles in α -quartz versus pressure, compared with experimental data of Glinneman *et al.* [33]. Closed symbols: calculations. Open symbols: experiment. The numbering of angles is identical to that in Fig. 3.1. Angles 1 and 4 are perpendicular on the plane of drawing in Fig. 3.1

Those angles are well predicted by the JC potential. This could be expected because the JC potential contains, besides an O-O pair potential term, an O-Si-O bending term, in contrast to both other potentials. Therefore, the underestimation of the Si-O-Si bond angle is mainly responsible for that of the OO_o distance and c -axis at low pressure. At higher pressures, the predicted OO_o distance and c -axis become increasingly too low. We attribute this to an underestimation of the O-O repulsions at *short* interatomic distances because the difference between predicted and experimental values for the Si-O-Si bond angle is nearly constant in the pressure range studied. (See Figs. 3.2 and 3.3.) We conclude that electrostatic interactions in the JC potential, which determine the Si-O-Si bond angle, are slightly too weak. This potential also underestimates the O-O repulsions at short interatomic distances.

Predictions of the KFBS potential for the α -quartz structure at variable pressures are less accurate than those of the JC potential. This is mainly caused by overestimation of the Si-O-Si bond angle as will be shown next. The too high KFBS values of the OO_o distance and c -axis are consistent with overestimation of the Si-O-Si bond angle. (See Figs. 3.2 and 3.3.) Predictions for the OO_l distance and a -axis, properties that are mainly determined by the O-O potentials, follow the experimental trend. (At variable pressures, the latter quantities are overestimated by 2% and 1%, respectively.) The KFBS potential predicts the tetrahedral bond angles in α -quartz less accurate than the JC potential. (See Fig. 3.4.) However, KFBS predictions for the angles which vary the most under pressure follow the experimental trend. The discrepancy between the KFBS-predicted structure and experiment is therefore mainly due to overestimation of the Si-O-Si bond angle. We conclude that the electrostatic interactions in the KFBS potential, which determine the Si-O-Si bond angle, are too stiff.

Predictions of the BJS I potential for the structure of α -quartz at variable pressures are less accurate than those of both other potentials. This is mainly due to underestimation of both the Si-O-Si bond angle and the O-O repulsions, as will be shown next. The BJS I potential underestimates the Si-O-Si bond angle at any pressure. The same holds for the predicted c -axis and OO_o distance. (See Figs. 3.2 and 3.3. The OO_o distance is underestimated by 10% at any pressure.) Predicted values for the OO_l distance and a -axis are 7% and 3% too low, respectively. This indicates that the O-O repulsions are too weak. These weak O-O repulsions might also be responsible for the less accurate prediction of the tetrahedral bond angles. (See Fig. 3.4.) We conclude that the electrostatic interactions in the BJS I potential, which determine the Si-O-Si bond angle, are too weak. This potential also underestimates the O-O repulsions.

How the above discussed deficiencies of each potential affect predictions for a large range of other physical properties will be discussed in the remaining sections.

3.3.2 Mechanical properties and acoustic modes of α -quartz

When α -quartz is subjected to high pressure, one of its acoustic modes becomes soft. Softening of an acoustic mode with a wave vector close to the Γ point indicates elastic instability of the material, caused by violation of the Born stability criteria [3,24]. Softening on other special points in the Brillouin-zone indicates formation of a supercell [5,15]. The X-ray diffraction measurements of Kingma *et al.* [21] indicate that α -quartz forms a $3 \times 3 \times 1$

supercell at $P = 21$ GPa. This supercell is created by tripling of the unit cell in the a and b directions of α -quartz and is consistent with acoustic mode softening along $[\xi \xi 0]$ at the K point [15]. According to Kingma *et al.* [21], α -quartz becomes gradually amorphous (i.e., the sample contains both crystalline and amorphous SiO_2) at pressures between 21 and 30 GPa. The material becomes completely amorphous at $P = 30$ GPa. [43]. Other reported amorphization pressures range from 15 to 35 GPa [30,35]. The amorphization of α -quartz is subject to debate. According to some authors [3,5,13], amorphization starts at the pressure which induces softening of acoustic modes close to the Γ point, indicating mechanical instability [24]. Others [19] suggest that amorphization immediately happens after formation of the $3 \times 3 \times 1$ supercell, just above the pressure that induces mode softening at the K-point. Amorphization of α -quartz would then be due to dynamic instability [19] prior to the mechanical instability. In this paper, we will compare experimental amorphization pressures with calculated pressures that induce acoustic mode softening close to the Γ point.

The JC potential predicts that the lowest acoustic branch along $[0 0 \xi]$ softens at the A point when α -quartz is subjected to a pressure of 9.6 GPa. This prediction indicates formation of a supercell that is *different* from the $3 \times 3 \times 1$ structure reported by Kingma *et al.* [21]. We will show that this discrepancy is due to underestimation of both the Si-O-Si bond angle and the O-O repulsions at short interatomic distances. At pressures slightly above 9.6 GPa, the JC potential predicts imaginary frequencies close to the Γ point for phonons along $[0 0 \xi]$, indicating that the structure becomes mechanically unstable. The mechanical stability of α -quartz is determined by the Born stability criteria $B1$, $B2$ and $B3$ [41]. Terhune *et al.* [41] showed along which directions acoustic mode softening must occur in order to violate these criteria. The JC-predicted mode softening along $[0 0 \xi]$ does *not* agree with any of those directions. Thus, the JC predicted supercell formation is not accurate, because it is due to mode softening along the $[0 0 \xi]$ direction. This leads to an instability that is inconsistent with violation of the Born stability criteria. The instability along $[0 0 \xi]$ indicates that the stiffness of the crystal in the c -direction is underestimated. At pressures well above 9.6 GPa, the JC potential predicts that the next branch which softens is the lowest acoustic branch along $[\xi \xi 0]$. At $P = 16.8$ GPa, this branch softens at the K point. At higher pressures, the JC potential predicts imaginary frequencies close to the Γ point for phonons propagating along $[\xi \xi 0]$. These results would be consistent with formation of the $3 \times 3 \times 1$ supercell at $P = 16.8$ GPa, followed by violation of the $B3$ stability criterion at a higher pressure. Thus, the softness in the c -direction of the JC-predicted crystal is responsible for softening of the lowest acoustic branch along $[0 0 \xi]$ before softening of modes with wave vectors along the correct $[\xi \xi 0]$ direction can take place. The underestimated stiffness of the crystal in the c -direction is due to underestimation of both the Si-O-Si bond angle and the O-O repulsions at short interatomic distances, as argued in Sec. 3.3.1. That the JC potential is less appropriate for studies of the mechanical properties of α -quartz under pressure is further indicated by less precise predictions for the pressure shifts of the elastic constants. The pressure shift of an elastic constant is defined as the derivative of this constant with respect to pressure at $P = 0$. Table 3.3 gives predicted and experimental values for the pressure shifts.

Table 3.3. Calculated pressure shifts of the elastic constants C_{ij} of α -quartz, compared with experimental data of McSkimin *et al.* [38] and Wang *et al.* [39].

C_{ij}	McSkimin	Wang	BJS I	KFBS	JC
C_{11}	3.82	1.49	1.65	1.38	-1.12
C_{12}	8.66	12.12	5.54	7.68	4.61
C_{13}	5.97	4.04	4.63	6.67	2.27
$ C_{14} $	1.93	3.96	1.73	1.83	1.26
C_{33}	10.84	9.51	11.50	14.79	1.94
C_{44}	2.66	1.84	-1.08	1.76	-2.14
C_{55}	-2.96	-5.32	-1.95	-3.15	-2.86

The BJS I potential predicts that the lowest acoustic branch along $[\xi \xi 0]$ softens in the vicinity of the Γ point when α -quartz is subjected to a pressure of 24.2 GPa. This value is comparable to experimental amorphization pressures (see above) and the predicted mode softening agrees with violation of the $B3$ stability criterion. However, at pressures below 24.2 GPa, no mode softening at the K point is predicted. Thus, the BJS I potential only predicts the pressure-induced elastic instability of α -quartz without prior formation of the $3 \times 3 \times 1$ superstructure. Thus, although the structure of α -quartz is predicted less accurately, the BJS I potential is still able to model the mechanical properties of this material under pressure. This can be explained as follows: Recall that the BJS I-predicted c -axis is systematically too low at all pressures due to underestimation of the Si-O-Si bond angle. Weak O-O repulsions are mainly responsible for the underestimated value of the a -axis. (See Sec. 3.3.1.) As the BJS I potential underestimates both axes, their ratio can still be accurate. The BJS I predicted c/a ratio is closest to that determined by experiment [30,33] at moderate and high pressures. Experimental, KFBS, JC and BJS I values for this ratio at $P = 9.5$ GPa are 1.131, 1.139, 1.122 and 1.129, respectively. Experimental, KFBS and BJS I values for the c/a ratio at $P=15.3$ GPa are 1.152, 1.162 and 1.154, respectively. The accurate BJS I prediction of the c/a ratio indicates a balance in the forces along the c and a direction. That the BJS I potential is suitable for modeling the mechanical properties of α -quartz, is further indicated by reasonable predictions for the pressure shifts of the elastic constants. (See Table 3.3.)

The KFBS potential predicts that the lowest acoustic branch along the $[\xi \xi 0]$ direction of α -quartz becomes soft at the K point when pressure is increased to 22.8 GPa. The predicted mode softening is consistent with formation of the $3 \times 3 \times 1$ superstructure, reported by Kingma *et al.* [21]. At higher pressures (25 GPa at $T=0$ [19]), the KFBS potential predicts imaginary frequencies for phonons with wave vectors along $[\xi \xi 0]$ which are close to the Γ point. This is consistent with violation of the $B3$ stability criterion. That the KFBS potential is appropriate for modeling the mechanical properties of α -quartz under pressure is further indicated by accurate predictions for the pressure derivatives of the elastic constants. (See Table 3.3). The good KFBS predictions for the mechanical properties of α -quartz at high pressures are not inconsistent with less accurate predictions for the structure. We recall from Sec. 3.3.1 that the KFBS potential overestimates the Si-O-Si bond angle, causing the predicted crystal to be too stiff in the c -direction. The

KFBS-predicted c/a ratio (see above) is slightly too high. Thus, the predicted crystal is relatively too soft in the a -direction. This favors the instability along the $[\xi \xi 0]$ direction, leading to violation of the $B3$ stability criterion.

3.3.3 Low-frequency Raman modes of α -quartz

We will consider low-frequency Raman modes of α -quartz and their pressure shifts because they are the most sensitive to pressure [10,17,18,34,36]. The pressure shift of a mode is defined as the derivative of the frequency with respect to pressure at $P = 0$. As low-frequency Raman modes are sensitive to temperature changes [36], we have done the calculations at $T = 300$ K. For predictions of high-frequency Raman modes we refer to $T = 0$ calculations in literature [10,17,18] as, according to experiment [36] and to our calculations, temperature effects are negligible for those modes. Table 3.4 presents predicted and experimental [34] values for low-frequency Raman modes of α -quartz at ambient conditions.

Table 3.4. Predictions for frequencies and pressure shifts (latter in parenthesis) of the six lowest Raman modes of α -quartz, compared with experiment [34]. Calculations are done using $\mathbf{k} \rightarrow \mathbf{0}$ along the c -axis. Calculations with $\mathbf{k} \rightarrow \mathbf{0}$ along the a -axis gave similar results. Frequencies are in cm^{-1} and pressure shifts in $\text{cm}^{-1} \text{kbar}^{-1}$

Expt.	BJS I	KFBS	JC	Symmetry
128 (0.54)	125 (0.35)	165 (0.57)	143 (0.50)	E(TO+LO)
206 (2.04)	227 (1.25)	226 (2.61)	222 (1.72)	A1
464 (0.81)	426 (1.21)	585 (0.19)	463 (0.82)	A1
696 (0.80)	695 (0.35)	718 (0.53)	717 (0.46)	E(TO+LO)
796 (0.59)	801 (0.50)	761 (0.91)	821 (0.57)	E(TO)
808 (0.59)	801 (0.50)	761 (0.91)	821 (0.57)	E(LO)

The JC predictions for those modes and their pressure shifts are accurate. This is consistent with good JC predictions for properties of α -quartz at zero pressure, as discussed previously. This also indicates that temperature effects are accurately predicted by the JC potential. Predictions of the BJS I potential for the low-frequency Raman modes are accurate, except that the experimental 464 cm^{-1} mode is underestimated. The BJS I-predicted atomic displacements of this mode show a symmetrical Si-O-Si bond angle stretch along the Si-O bonds, which agrees with experiment [34]. The underestimated frequency of the latter mode indicates that the predicted stretch is too weak. This is due to the predicted Si-O-Si bond angle, which is too small, because in silicates there exists a negative coupling between the Si-O bond distance and the Si-O-Si bond angle [37]. Consequently, the Si-O bond distance is slightly overestimated. (See Tables 3.1 and 3.2). The overestimated pressure shift of the experimental 464 cm^{-1} mode further indicates that the interactions in the BJS I potential which determine the Si-O-Si bond angle are too weak. The other modes and their pressure shifts are accurately predicted, although the calculated α -quartz structure is less close to experiment. As for the BJS I results, discussed earlier, this is due to underestimation of both the Si-O-Si bond angle and the O-O repulsions. This can be seen as follows: Atomic displacements of the BJS I-calculated 125 cm^{-1} mode correspond

with rotation of the tetrahedra around their twofold axis perpendicular to the c -axis. The rotation of the tetrahedra is caused by O-O repulsions along the OO_s distances. (See Fig. 3.1.) We recall that the Si-O-Si bond angle and the correlated OO_s distance in α -quartz are underestimated by the BJS I potential. This would cause an overestimation of O-O repulsions along the OO_s distances. The latter would facilitate an easy rotation of the tetrahedra, leading to an underestimation of the frequency. The fact that this does not happen indicates that the O-O repulsions must be too weak. Thus, the weak O-O repulsions compensate for the too small value of the Si-O-Si bond angle. Atomic displacements of the other modes are complex and show changes in the Si-O-Si bond angle and distortion of O-Si-O angles. The accurate prediction of those modes might also be due to the above mentioned compensation effect. At high pressure, the experimental 577 cm^{-1} mode, which corresponds to the symmetrical Si-O-Si bond angle stretch, is underestimated while the two lowest Raman modes are predicted accurately. Calculated and experimental values for the low-frequency Raman modes of α -quartz at 20 GPa are given in Table 3.5. Thus, also at elevated pressure, the underestimated Si-O-Si bond angle is compensated by weak O-O interactions.

Table 3.5. Predictions of the six lowest Raman modes of α -quartz at $P = 20\text{ GPa}$ and $T = 300\text{ K}$, compared with experiment [34]. Calculations are done using $\mathbf{k} \rightarrow \mathbf{0}$ along the c -axis. Calculations with $\mathbf{k} \rightarrow \mathbf{0}$ along the a -axis gave similar results. Frequencies are in cm^{-1} .

Expt.	BJS I	KFBS	Symmetry
165	165	242	E(TO+LO)
311	308	348	A1
577	551	651	A1
793	720	825	E(TO+LO)
895	838	874	E(TO)
895	838	874	E(LO)

We recall that the KFBS potential overestimates the Si-O-Si bond angle. This is clearly reflected in the calculated low-frequency Raman modes and their pressure shifts for α -quartz at ambient conditions. (See Table 3.4.) Overestimation of the experimental 464 cm^{-1} mode is consistent with overestimation of the Si-O-Si bond angle, for the same reasons explained for the BJS I potential. Consequently, the predicted pressure shift of this mode is too low. Overestimation of the experimental 128 cm^{-1} mode reflects a hindered rotation of the tetrahedra. This is due to overestimation of the Si-O-Si bond angle and the correlated OO_s distance. The latter causes O-O repulsions which are too weak. We notice that the overestimated stiffness of the Si-O-Si bond angle is less apparent in predictions for the higher frequency modes. (See Table 3.4.) The KFBS potential also overestimates the above mentioned frequencies at high pressures (See Table 3.5.) We have discussed the relation between potential parameters and predicted properties of α -quartz at variable pressures. The effect of these parameters on predictions for temperature dependent properties of α -quartz, will be discussed below.

3.4 Properties of α -quartz at variable temperatures

3.4.1 Temperature-induced changes of the α -quartz structure

Experiments [33,43] indicate that the α -quartz structure changes slightly upon heating. According to experiment [43], the Si-O-Si bond angle increases by 2.5° in the range 300 – 813 K. The BJS I, KFBS and JC-predicted values for this change are 2.3° , 1.4° and 0.9° , respectively. All potentials predict that the largest change of the tetrahedral angles is less than one degree in the range 300 – 813 K, which agrees with experiment [43]. Table 3.6 shows predicted and experimental values for the Si-O bond distances in α -quartz at elevated temperatures.

Table 3.6. Calculated and experimental[43] Si-O bond distances of α -quartz at several temperatures. T denotes temperature, r_l the longest and r_s the shortest Si-O bond distance. Distances are in Å and temperatures in K.

T	Expt.		BJS I		KFBS		JC	
	r_s	r_l	r_s	r_l	r_s	r_l	r_s	r_l
300	1.605	1.614	1.620	1.622	1.598	1.606	1.607	1.614
813	1.600	1.594	1.618	1.621	1.600	1.606	1.608	1.614

Only the BJS I potential predicts that both Si-O bond distances decrease in the temperature range studied. This agrees with the experimental trend. Table 3.7 gives calculated and experimental values for the elastic constants of α -quartz at variable temperatures. The mechanical properties of α -quartz do not show a strong temperature dependence in the temperature range studied. All three potentials give accurate predictions for those constants. Thus, the potentials predict that temperature-induced changes of the elasticity and structure of α -quartz are small. This is in accordance with experiment. Therefore, the accuracy of the predicted structure and elasticity of α -quartz at elevated temperatures is mainly determined by the performance of the potentials at ambient conditions. The latter was discussed in Sec. 3.3.

Table 3.7. Predictions for elastic constants of α -quartz at several temperatures compared with experiment [40]. Elastic constants are denoted as C_{ij} and are in GPa.

$T = 300 \text{ K}$				
C_{ij}	Expt.	BJS I	KFBS	JC
C_{11}	84.84	87.78	89.63	95.25
C_{12}	5.31	13.82	3.96	16.21
C_{13}	12.24	9.18	11.68	18.63
C_{14}	-17.66	-18.20	-18.50	-15.08
C_{33}	105.44	107.20	99.55	115.17
C_{44}	57.55	55.12	49.22	51.00
C_{66}	39.77	36.98	42.83	39.51
$T = 400 \text{ K}$				
C_{ij}	Expt.	BJS I	KFBS	JC
C_{11}	84.18	87.64	89.51	95.38
C_{12}	3.42	13.13	3.01	15.75
C_{13}	11.20	8.68	10.90	18.42
C_{14}	-17.72	-18.39	-18.66	-15.19
C_{33}	103.18	105.77	97.90	114.98
C_{44}	56.92	55.23	48.97	51.19
C_{66}	40.38	37.25	43.25	39.82

3.4.2 Thermodynamics and phonon dispersion curves of α -quartz

We have studied the low-frequency phonon dispersion curves of α -quartz because these phonons mainly determine the thermodynamic properties. Figure 3.5 illustrates calculated and experimental phonon dispersion curves of α -quartz at $T = 20 \text{ K}$ and $T = 300 \text{ K}$. These phonons were measured with inelastic scattering experiments [44,45]. Calculations at $T = 800 \text{ K}$ indicate that the phonon dispersion curves of α -quartz virtually do not change with temperature. We can thus relate the accuracy of the predicted thermodynamic properties at any temperature to that of the phonon dispersion curves in Fig. 3.5. The JC potential gives the most accurate prediction for the phonon dispersion curves. Consequently, the thermodynamic properties of α -quartz are accurately predicted. The JC prediction for the constant-pressure entropy differs by 1% from the experimental value [46] for temperatures between 200 and 800 K. Also, the JC prediction of the constant-pressure heat capacity is accurate for temperatures up to 700 K. Figure 3.6 illustrates calculated and experimental heat capacities. We notice that all predicted values for the heat capacity show similar deviations from experiment at temperatures above 700 K. This is perhaps caused by the semi-harmonic calculations, which can not cope with the α -quartz \rightarrow β -quartz transition, instead of inaccuracies in the parameter sets.

The accuracy of the BJS I-predicted phonon dispersion curves is almost comparable to that of the JC potential. (See Fig. 3.5.) Thus, the less accurate BJS I prediction for the structure of α -quartz is virtually not reflected in the calculated phonon dispersion curves. This is consistent with our discussion on the Raman results. (See Sec. 3.3.3.)

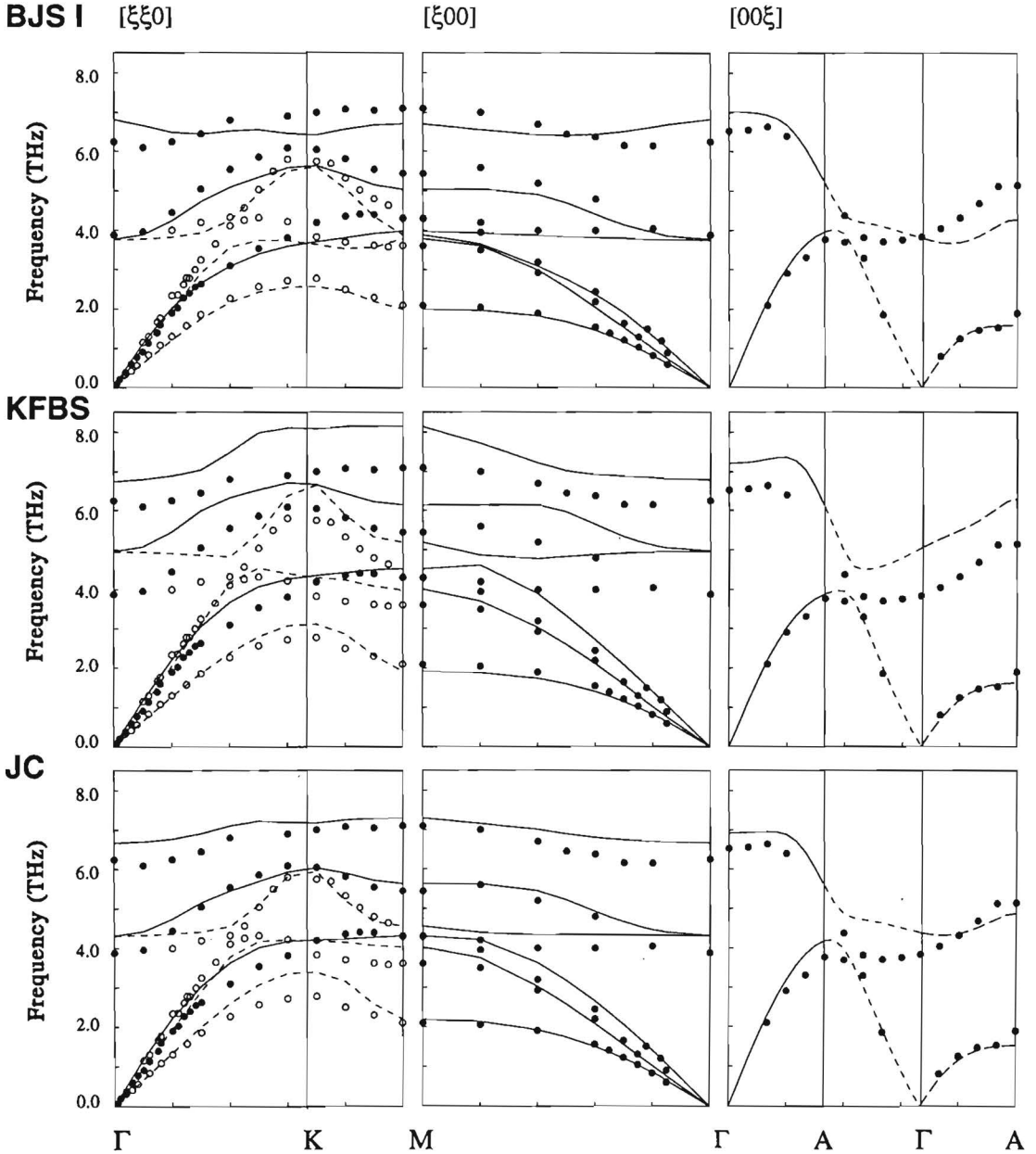


Figure 3.5. Calculated low-frequency phonon dispersion curves in the main directions of α -quartz in comparison with experiment. The $[\xi \xi 0]$ and $[\xi 0 0]$ direction are measured by Dorner *et al.* at $T = 300$ K [44] and calculations are done at $T = 300$ K. The $[0 0 \xi]$ direction is measured by Strauch *et al.* [45] at $T = 20$ K and calculations are done at 0 K. Lines represent calculations. Points represent measurements. In $[\xi \xi 0]$ direction: open points and broken lines show the T2 representation, closed points and straight lines show the T1 representation. For the $[0 0 \xi]$ direction an extended zone scheme is used.

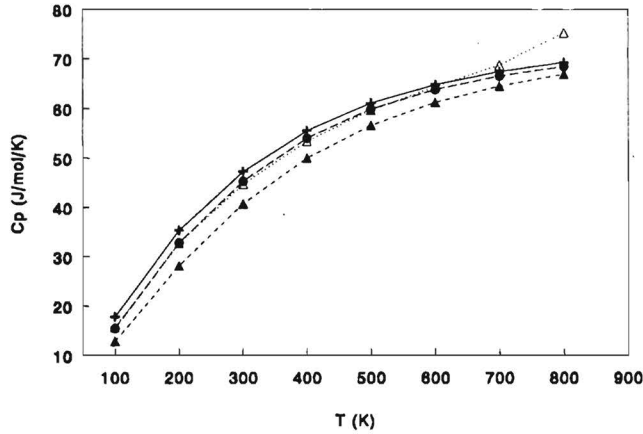


Figure 3.6. Predictions for the constant pressure heat capacity of α -quartz versus temperature, compared with experimental data of Richet *et al.* [46]. Crosses: BJS I predictions. Closed triangles: KFBS predictions. Closed points: JC predictions. Open triangles: experimental data.

The BJS I prediction of the constant-pressure heat capacity is accurate. The constant-pressure entropy is overestimated by 7%, which seems reasonable. The KFBS potential overestimates the optic branches in the phonon dispersion diagram. (See Fig. 3.5). This must be due to overestimation of the Si-O-Si bond angle, as shown in our discussion on the Raman results. (See Sec. 3.3.3.) Consequently, the constant-pressure entropy and heat capacity are systematically underestimated. (See Fig. 3.6. The entropy is underestimated by 12%.) Gonze *et al.* have reported first-principles calculations of the phonon dispersion curves [7] and the constant-volume heat capacity [8] of α -quartz, that are in better agreement with experiment than the predictions of the BJS I and JC potential. Given the simplicity of the latter calculations compared to the *ab initio* calculations, we consider the predictions of the BJS I and JC potential to be very reasonable. Gonze *et al.* [7–9] compared the interatomic force constants, calculated with the KFBS potential, with those obtained from the *ab initio* calculations. They suggest that two-body potentials are less suitable for a detailed description of the lattice dynamics of α -quartz. They advocate the use of three-body potentials. In this work we have shown that the JC potential, which contains a three-body term, indeed gives better predictions than the KFBS potential for the phonon dispersion curves of α -quartz.

3.5 Conclusions

3.5.1 The JC potential

The JC potential can model low-frequency Raman spectra and phonon dispersion curves of α -quartz at zero pressure. Good predictions are also given for the structure and the elasticity at zero pressure. Thermodynamic properties and the structure of α -quartz at variable temperature are accurately predicted. The JC potential is not able to model properties of α -quartz at pressures above 9.6 GPa. This is due to a predicted acoustic mode softening which is not in accordance with violation of the Born stability criteria. The less accurate performance of the JC potential at higher pressures is due to underestimation of both the Si-O-Si bond angle and the O-O repulsions at short interatomic distances. Therefore, we expect that the JC potential is less appropriate for the modeling of materials that are characterized by small Si-O-Si bond angles combined with short O-O distances, which is the case for dense structures or materials that are subjected to high pressures. This is consistent with predictions of the JC potential for the structure and elasticity of the dense materials stishovite and coesite [10,12,50], which are less accurate than those of the other potentials. We expect that the JC potential is appropriate for the modeling of thermodynamic properties, low-frequency phonon dispersion curves and the structure of materials which have a density lower than that of α -quartz. This is in line with accurate predictions of the structure [10,11,17], low-frequency Raman and infrared spectra [49] of a large variety of silicates.

3.5.2 The KFBS potential

At low pressures and variable temperatures, the KFBS potential models the α -quartz structure less accurately than the JC potential. The KFBS prediction for the elastic constants at ambient conditions is accurate. The KFBS potential is less suitable for modeling low-frequency Raman modes at any pressure. Also, the phonon dispersion curves and thermodynamic properties of α -quartz at zero pressure are less accurately predicted. At high pressures, the KFBS prediction for the mechanical properties of α -quartz is accurate and the structure is predicted reasonably. Overestimation of the Si-O-Si bond angle is mainly responsible for the less accurate prediction of the structure, spectra and thermodynamical properties of α -quartz. We have demonstrated that the overestimated stiffness of the Si-O-Si bond angle does not conflict with correct predictions for the mechanical behavior of α -quartz at high pressures. We expect the KFBS potential to be appropriate for high pressure studies on the structure and elasticity of dense silicates. This is in line with reasonable predictions for the structure and elasticity of stishovite] and coesite [12, 50] at zero pressure and temperature. We expect that the KFBS potential would be less suitable for modeling the structure and thermodynamic properties of materials having a density lower than that of α -quartz. This is consistent with less accurate predictions for the structure [48] and the low-frequency Raman and infrared spectra [49] of a large variety of all-silica polymorphs.

3.5.3 The BJS I potential

Predictions of the BJS I potential for the α -quartz structure are less accurate than those of both other potentials. This potential is able to model elasticity, thermodynamic properties, low-frequency Raman modes and phonon dispersion curves of α -quartz at zero pressure. The BJS I potential gives accurate predictions for the mechanical properties and the low-frequency Raman modes of α -quartz at high pressure. The less accurate prediction of the structure is mainly due to underestimation of both the Si-O-Si bond angle and the O-O repulsions. The underestimated O-O repulsions partially compensate for the too narrow Si-O-Si bond angle and therefore the BJS I predictions for properties other than the structure are less affected. As the BJS I potential is completely *ab-initio*, there is no reason to believe that it should behave differently for other silica-polymorphs, which is supported by calculations at zero pressure and temperature for a large variety of silica-polymorphs [10, 48]. We therefore expect the BJS I potential to be appropriate for modeling thermodynamic and mechanical properties of silicates at variable pressures. In particular, the ability to model thermodynamic properties of silicates at high pressure is desirable. Our results indicate that this is not feasible with both other potentials. The BJS I results indicate that both the O-O repulsion and the interactions that govern the Si-O-Si bond angle must be stiffened. A modified version of the BJS I potential with stiffened Si-O-Si bond angle interactions indeed gives better structure predictions for a large number of all-silica polymorphs, as has been shown elsewhere [48]. Further improvement of the BJS I potential is subject of current research.

3.6 Appendix: Sampling schemes

Free energy calculations require evaluation of the phonon-frequencies for all wave vectors in the Brillouin zone. The frequencies are determined by taking only the frequencies on a 3 dimensional grid in the Brillouin zone with an appropriate weighting factor [26]. Grids must be carefully chosen to avoid results that are determined by the number of \mathbf{k} -points used. To select an appropriate grid we did the following tests. Calculations have been done on α -quartz for several temperatures using the three potentials with a number of grids proposed by Fillipini *et al.* [26] and Pavesi *et al.* [28]. We have varied for each grid the number of \mathbf{k} -points. We have checked uneven grids, which are more dense in the region of the Γ point, against equally spaced grids. We also tested the effect of sampling the whole or the half irreducible part of the Brillouin zone, because α -quartz is trigonal and therefore, in principle, the whole Brillouin zone should be sampled [26]. We found that the calculated constant pressure entropy varies the most with the use of a particular grid where variation in other properties is negligible at any temperature above $T = 50$ K. For 125 points in \mathbf{k} -space at $T = 300$ K the variation in the entropy with the above mentioned grids is less than 1%. This variation decreased at higher temperatures, due to the lower occupancy number of the phonons close to the Γ point. Furthermore, we carried out calculations at elevated temperature *and* pressure. The use of a dense grid is then mandatory for detecting imaginary frequencies that are due to pressure-induced mode softening. Hence, we selected the following uneven 125-point grid in \mathbf{k} -space ($N = 5$), with each of the three coordinates k_n having values:

$$k_n = \frac{3(2^{n-1}) - 2}{4(2^N - 1)}. \quad (3.3)$$

In Eq. (3.3) N denotes the number of grid points in the reciprocal lattice and $n=1,2,\dots,N$. For temperatures below 50 K all predicted properties vary too much with the number of \mathbf{k} -points in any used grid. This is caused by the strongly increasing acoustic modes near the Γ point which contribute the most at low temperatures. More elaborate schemes are then needed [29]. Therefore, we present results for temperatures above 100 K. Furthermore, the calculations do not include the Γ point, due to the singularity in the Ewald sum at $\mathbf{k}=\mathbf{0}$. Hence we give Raman results obtained from calculations in the limit $\mathbf{k} \rightarrow \mathbf{0}$. Calculations have been done with this limit taken along the a and c -axis of α -quartz.

3.7 References

- [1] J. Chelikowsky, N. Troullier, J.L. Martins and H.E. King, *Phys. Rev. B* **44**, 489 (1991).
- [2] N. Binggeli, N. Troullier, J.L. Martins and J. Chelikowsky, *Phys. Rev. B* **44**, 4771 (1991).
- [3] N. Binggeli and J. Chelikowsky, *Phys. Rev. Lett.* **69**, 2220 (1992).
- [4] N.R. Keskar and J.R. Chelikowsky, *Phys. Rev. B* **46**, 1 (1992).
- [5] N. Binggeli, N.R. Keskar and J.R. Chelikowsky, *Phys. Rev. B* **49**, 3075 (1994).
- [6] J.R. Chelikowsky and N. Binggeli, *Comp. Mater. Sc.* **2**, 111 (1994) and references therein.
- [7] X. Gonze, J.C. Charlier, D.C. Allan and M.P. Teter, *Phys. Rev. B* **50**, 13035 (1994).
- [8] C. Lee and X. Gonze, *Phys. Rev. B* **72**, 1686 (1994).
- [9] C. Lee and X. Gonze, *Phys. Rev. B* **51**, 8610 (1995).
- [10] K. de Boer, A.P.J. Jansen and R.A. van Santen, *Chem. Phys. Lett.* **223**, 46 (1994), *Chapter 2 of this thesis*.
- [11] R.A. Jackson and C.R.A. Catlow, *Mol. Simul.* **1**, 207 (1988).
- [12] G.J. Kramer, N.P. Farragher, B.W.H. van Beest and R.A. van Santen, *Phys. Rev. B* **43**, 5068 (1991).
- [13] S. Tsuneyuki, M. Tsukada, H. Aoki and Y. Matsui, *Phys. Rev. Lett.* **61**, 869 (1988).
- [14] S.C. Parker, computercode: PARAPOCS, BATHPROGS (School of Chemistry, University of Bath, Claverton Down, Bath BA2 7AY, U.K.)
- [15] M.S. Somayazulu, S.M. Sharma and S.K. Sikka, *Phys. Rev. Lett.* **73**, 98 (1994) and references therein.
- [16] J.S. Tse and D.D. Klug, *Phys. Rev. Lett.* **67**, 3559 (1991).
- [17] P. Tschaufeser, PhD. thesis, University of Bath, Bath (1992).
- [18] G.W. Watson, PhD. thesis, University of Bath, Bath (1994).
- [19] G.W. Watson and S.C. Parker, *Phil. Mag. Lett.* **71**, 59 (1995).
- [20] C.R.A. Catlow and M.J. Norgett, *Lattice Structure and Stability of Ionic Materials*, private communication.
- [21] K.J. Kingma, R.J. Hemley, H.H. Mao and D.R. Veblen, *Phys. Rev. Lett.* **70**, 3927 (1993).
- [22] L.E. McNeil and M. Grimsditch, *Phys. Rev. Lett.* **72**, 1301 (1994).
- [23] K.J. Kingma, R.J. Hemley, H.H. Mao and D.R. Veblen, *Phys. Rev. Lett.* **72**, 1302 (1994).
- [24] M. Born and K. Huang, *Dynamical Theory of Crystal Lattices, The international series of monographs on physics* edited by D.H. Wilkinson and W. Marshall (Clarendon press, Oxford, 1968).
- [25] S.C. Parker and G.D. Price, *Advances in Solid-State Chem.* **1**, 295 (1989).
- [26] G. Filippini, C.M. Gramaccioli, M. Simonetta and G.B. Suffritti, *Acta. Cryst. A* **32**, 259 (1979).
- [27] G.J. Kramer, A.J.M. de Man and R.A. van Santen, *J. Am. Chem. Soc.* **113**, 6435 (1991).
- [28] A. Pavesi, private communication.
- [29] T.H.K. Barron and A. Pasternak, *J. Phys. Solid. State. Phys.* **20**, 215 (1987).
- [30] R.M. Hazen, L.W. Finger, R.J. Hemley, and H.K. Mao, *Solid State Commun.* **507** (1989).
- [31] L. Levien, C.T. Prewitt and D.J. Weidner, *Am. Mineral.* **65**, 920 (1980).
- [32] We compare predicted values for the Si-O-Si bond angle with experimental data of Glinneman *et al.* [33], that were obtained for pressure between 0 and 10.2 GPa. Although Hazen *et al.* [30] reported bond angles of α -quartz at pressures up to 12.5 GPa, we do not use these values in our comparison because they are less precise than the Glinneman data [33]. Calculated values for the *c*-axis and *c/a* ratio are compared with both the Glinneman and Hazen data.

- [33] J. Glinneman, H.E. King Jr., H. Schultz, Th. Hahn, S.J. La Placa and F. Dacol, *Z. Kristallogr.* **198**, 177 (1992).
- [34] R.J. Hemley in *High Pressure Research in Mineral Physics, Geophys. Monogr. Ser.* **39**, edited by M.H. Manghnani and Y. Syono (AGU, Washington D.C, 1987) pp. 347-359.
- [35] R.J. Hemley, A.P. Jephcoat, H.K. Mao L.C. Ming and M.H. Manghnani, *Nature* **334**, 52 (1988).
- [36] K.J. Dean, W.F. Sherman and G.R. Wilkinson, *Spectrochim. Acta.* **38A**, 1105 (1982).
- [37] R.J. Hill and G.V. Gibbs, *Acta Cryst. B* **35**, 25 (1978).
- [38] H.J. Mc Skimin, P. Andreat Jr. and R.N. Thurston, *J. Appl. Phys.* **36**, 1524 (1965).
- [39] Q. Wang, G.A. Saunders, E.F. Lambson, P. Tschaufeser, S. C. Parker and B.J. James, *Phys. Rev. B* **45**, 10242 (1992).
- [40] Q. Wang, First Year Report, University of Bath, Bath (1990).
- [41] W. Terhune, T. Kushida and G.W. Ford, *Phys. Rev. B* **32**, 8416 (1985).
- [43] K. Kihara, *Europ. J. Mineral.* **2**, 63 (1990).
- [44] B. Dorner, H. Grimm and H. Rzany, *J. Phys. C: Solid St. Phys.* **13**, 6607 (1980).
- [45] D. Strauch and B. Dorner, *J. Phys. Condens. Matter* **5**, 6149 (1993).
- [46] P. Richet, Y. Bottinga, L. Denielou, J.P. Petit and C. Tepui, *Geoch. Cosmochem. Acta* **46**, 2639 (1982).
- [47] S.W. Kieffer, *Rev. Geophys. Space Phys.* **17**, 1 (1979).
- [48] K. de Boer, A.P.J. Jansen and R.A. van Santen, *Phys. Rev. B* **52**, 12579 (1995), *Chapter 5 of this thesis.*
- [49] A.J.M. de Man, PhD. thesis, Eindhoven University of Technology, Eindhoven (1992).
- [50] K. de Boer, A.P.J. Jansen, R.A. van Santen and S.C. Parker, *Phys. Rev. B in press, (Chapter 6 of this thesis)*

Chapter 4

Derivation of an all-silica shell model potential from *ab initio* data and the structure of α -quartz

Abstract

We present the derivation of a new shell model potential which is fitted on *ab initio* data of small silicious clusters and the structure of α -quartz at low temperature. Our calculations indicate that this potential can model the structure, phonon dispersion curves and thermodynamical properties of all-silica polymorphs at variable temperatures. The potential is less suitable for modeling the elasticity and the pressure behavior of those systems. The reliability of this potential is compared with that of three other interatomic potentials.

4.1 Introduction

The rich polymorphism of all-silica zeolites combined with their technological importance as selective catalysts and absorbents has introduced widespread interest in the physical and chemical properties of those systems. Therefore, a large number of approaches has been developed to predict all-silica structures and their properties. These approaches vary from *ab initio* calculations [1–9] to those based on interatomic potentials [10–13]. Although *ab initio* calculations on small systems such as α -quartz give more accurate results than the interatomic potentials reported so far [10–13], those calculations become computationally intractable when applied to complex systems such as zeolites [4]. The derivation of reliable interatomic potentials, especially those based on *ab initio* data, is therefore a subject of interest. In previous work we presented a shell model potential that was solely derived from *ab initio* data on small silicious clusters. This potential will be referred to as the BJS I potential [10]. Elsewhere we have shown that the BJS I potential predicts a large number of all-silica structures less accurately than other empirical or semi-empirical potentials [10,14]. This is mainly due to underestimation of the Si-O-Si bond angle in those systems. In a study on calculated properties of α -quartz at elevated temperatures and pressures we have shown that the Si-O-Si bond angle interactions and the O-O repulsions of the BJS I potential must be stiffened [15].

In this work we discuss our attempts to improve the BJS I potential. We present the derivation of a new shell model potential, which will be referred to as the BJS II potential. This potential is derived from *ab initio* data of small silicious clusters and the structure of α -quartz at low temperature. The reliability of the BJS II potential will be compared with that of the BJS I potential and two other interatomic potentials. The latter potentials are the rigid-ion model potential derived by Kramer *et al.* [12] and the shell model potential published by Catlow *et al.* [11]. Those potentials will be referred to as the KFBS and JC potential, respectively. The JC potential is derived from experimental data on α -quartz. The KFBS potential is derived from *ab initio* data on small silicious clusters and experimental data on α -quartz.

We will show that the BJS II potential gives accurate predictions for several substantially different all-silica structures. The accuracy of these predictions is comparable to that of the JC potential. Our calculations indicate that the BJS II potential is suitable for modeling the structure, phonon dispersion curves and thermodynamical properties of all-silica polymorphs at variable temperatures. The BJS II potential gives less accurate predictions for the elasticity of these materials. Our results further indicate that this potential cannot model the behavior of all silica-polymorphs at high pressures, in contrast to the BJS I and KFBS potential.

4.2 Method and computational details

4.2.1 Parametrization procedure

In this section we will treat our attempts made to improve the BJS I potential. This potential has the following form:

$$E^{pot} = \sum_{\substack{i,j \\ i < j}} [A_{ij} \exp\left(\frac{-r_{ij}}{\rho_{ij}}\right) - \frac{C_{ij}}{r_{ij}^6}] + \sum_{\substack{i,j \\ i < j}} \frac{q_i q_j}{r_{ij}} + \frac{1}{2} \sum_i k(r_{i,shell} - r_{i,core})^2 \quad (4.1)$$

The first and second term in Eq. (4.1) constitute the well-known Buckingham form. The O-O interaction only acts through the shells, the Si-O interaction acts between the O shell and the Si ion. The fourth term is the harmonic interaction, which acts between core and shell of the same O atom. The Coulomb term includes all electrostatic interactions between cores, between shells, and between cores and shells belonging to different atoms.

The Buckingham parameters of the BJS I potential were derived from fits on *ab initio* potential energy surfaces of $\text{Si}(\text{OH})_4$ clusters that were calculated with Møller-Plesset second-order perturbation theory (MP2). The atomic and shell charges of this potential were derived from *ab initio* dipole moments and polarizability tensors of $(\text{HO})_3\text{SiOSi}(\text{OH})_3$ clusters, which were calculated using self-consistent Hartree-Fock (SCF). The latter quantities were calculated with SCF because MP2 required too much computational resources at that time [10]. The value of the spring constant k was fixed at the value which gave the smallest error in the fits. As the Buckingham parameters and the charges are interdependent, the fit procedures are done iteratively. Details of the *ab initio* calculations and these procedures are given in Ref. 10.

In a first attempt to improve the BJS I potential, we employed the fit procedures and *ab initio* calculations described in Ref. 10, except that we used MP2-calculated values for the dipole moments and polarizabilities of the $(\text{HO})_3\text{SiOSi}(\text{OH})_3$ clusters. The potential obtained in this way will be referred to as the BJSM potential. This potential appears to give unsatisfactory results, which will be discussed in Sect. 4.3.1. Therefore, we derived a new potential, referred to as the BJS II potential. This potential is fitted on the structure of α -quartz and the same *ab initio* data as used in the parametrization of the BJSM potential. In our derivations it is assumed that all atoms of the same type have identical charges, irrespective of their positions. Furthermore, the ratio of the atomic charges is fixed to $q_{\text{Si}} = -2q_{\text{O}} = 4q_{\text{H}}$, in order to keep the luster and the crystal neutral [10]. Hence, the value of the atomic charges is essentially determined by one parameter q . The parameter q is the sum of the shell and the core charge. The BJS II potential is derived by first choosing a large range of values for q , denoted as q_i . For each value q_i we fitted the covalent parameters on the *ab initio* potential energy surfaces of the $\text{Si}(\text{OH})_4$ clusters used in the derivation of the BJSM potential. During this fit we kept the shell charge and spring constant fixed on the values obtained for the BJSM potential. Thus, we only varied the core charge when choosing values for q_i . For each value q_i we

obtained a different parameter set. With each of these parameter sets we calculated the structure of α -quartz at absolute zero. Afterwards we selected the parameter set that gave the best agreement between the calculated structure at 0 K and the experimental [16] structure at 13 K.

4.2.2 Calculations

Calculations were done with the code PARAPOCS [17] which can be used to compute physical properties of solids at variable temperatures and pressures. To calculate thermodynamical properties, the vibrational frequencies of the solid have to be computed. The calculations assume that vibrational motions in the solid are described by collective harmonic oscillators. The frequency of those oscillators varies with cell volume [18]. Minimization of the Gibbs free energy can be achieved by varying the cell volume and the positions of the ions until the configuration satisfies the following equilibrium conditions for a given temperature and pressure:

$$\frac{\partial F}{\partial V} = P_{app}, \quad (4.1)$$

$$\frac{\partial U_{stat}}{\partial \mathbf{r}} = \mathbf{0}. \quad (4.2)$$

In Eq. (4.1) F denotes the Helmholtz free energy, V the cell volume and P_{app} the applied pressure. In Eq. (4.2) \mathbf{r} denotes the atomic coordinates and U_{stat} the static energy due to the interatomic interactions. Equation (4.1) states that the pressure exerted by the system (internal pressure) must equal the applied pressure. (This equation is only valid for cubic crystals. For more general cases the derivatives of the Helmholtz free energy with respect to the strain must be computed. Details can be found in Ref. 19.) Equation (4.2) states that the net force on each atom must vanish. After the Gibbs free energy is minimized, thermodynamical properties, elastic constants, dielectric constants and the structure of the solid can be computed. Calculation of the Helmholtz free energy and other thermodynamical properties requires computation of the vibrational frequencies for all wave vectors in the Brillouin-zone. This is done by computation of the frequencies on a three-dimensional grid within the Brillouin-zone. In our calculations we used the grid of Pavese *et al.* [20] with each of the three coordinates k_n having values:

$$k_n = \frac{3(2^{n-1}) - 2}{4(2^N - 1)}, \quad (4.3)$$

where N denotes the number of grid points in the reciprocal lattice and $n=1,2,..N$. In our calculations on stishovite, coesite and α -quartz we used the above grid with 125 k-points ($N = 5$). In a study on calculations of α -quartz we have tested the accuracy of integration schemes and we found that properties computed using this grid with 125 k-points are accurate [15] and we obtained similar results for stishovite and coesite. In calculations on the larger all-silica zeolites we have used the above grid with eight k-points ($N = 3$). Elsewhere it is shown that a coarse grid gives sufficiently accurate results for those systems [21]. The stability of all minimized

structures was tested by checking if all phonon frequencies were real on a grid in k -space of 125 grid points ($N = 5$). Cutoffs applied in calculations using the KFBS and JC potential are 10 Å [22]. The covalent O-O interactions of the BJS I, BJSM and BJS II potential are applied with a cutoff of 3.5 Å, because for larger distances all covalent potential terms are effectively zero. The covalent Si-O interaction of these potentials are applied with a cutoff of 2.5 Å (i.e. in between the nearest and next nearest Si and O neighbors) to simulate a real Si-O bond. The electrostatic interactions are calculated using the Ewald summation.

4.3 Results

First, we will discuss results of the parametrizations. Subsequently we will compare the performance of our potentials with results of the KFBS, BJS I and JC potential. We will consider predictions for the structure and elasticity of all-silica polymorphs at ambient conditions. We will discuss predictions for the physical properties of α -quartz at elevated pressures and temperatures. Preliminary results for all-silica zeolites at elevated temperatures will also be given.

4.3.1 Results of the parametrizations

Parametrization of the BJSM potential gives, similar to the BJS I potential [10], the following results for the fit errors:

- Errors of the fits on the potential energy surfaces of the $\text{Si}(\text{OH})_4$ cluster decrease asymptotically with increasing values of the spring constant k .
- The error of the shell charge fit decreases asymptotically with increasing k .
- The error of the fit determining the atomic charges has the lowest value for $k = 33.52 \text{ eV}\text{\AA}^{-2}$

Similar to the derivation of the BJS I potential, we selected the parameter set with the k value that gives a minimal error in the fit of the atomic charges. Table 4.1 presents parameter sets and errors of the fits. Errors for the fits which determine atomic and shell charges of the BJSM potential, are substantially lower than the BJS I values. The shell and atomic charges of the BJSM potential are 1.7% and 4% higher, respectively, than the BJS I values. MP2-calculated polarizabilities and dipole moments used in the fit of the BJSM potential, are 10% higher and 3.6% *lower*, respectively, than the SCF values used in the derivation of the BJS I potential. That the atomic charges of the BJSM potential are *higher* than those of the BJS I potential, is caused by application of the shell model as the following will demonstrate. If a rigid-ion model potential and SCF calculated dipoles are used in the fits we obtain a value of -0.7885 for the oxygen charge. The use of MP2-calculated dipoles in these fits gives a value of -0.7598, which is indeed 3.6% lower than the SCF value. If the shell model is applied, we find that the polarization of each $(\text{HO})_3\text{SiO}\dot{\text{S}}\text{i}(\text{OH})_3$ cluster used in the fit gives a net dipole moment that is opposite to the *ab initio* dipole moment. Hence, a larger atomic charge than in case of a rigid ion model is needed to fit the *ab initio* dipole moments of these clusters. A larger polarizability of the clusters, requires a higher atomic charge in order to fit the *ab initio* dipole moment. (In the equations used in the fit, the atomic charge depends linearly on the shell charge.) The MP2-calculated polarizabilities of the

$(\text{HO})_3\text{SiOSi}(\text{OH})_3$ clusters are substantially higher than the SCF values, whereas the calculated dipoles differ only slightly (see above). This explains why the atomic charges derived from the MP2 data are larger than the SCF values. Although the electrostatic parameters of the BJS I and BJSM potential are different, the fits on the *ab initio* potential energy surfaces of the $\text{Si}(\text{OH})_4$ cluster give comparably small errors for both potentials. (See Table 4.1.) As the BJS I and BJSM potential are derived from comparably accurate fits on identical potential energy surfaces, these potentials differ mainly by their values of the atomic and shell charges.

Table 4.1. Parameter sets and rms errors of the fits. The C term of all potentials is zero. Parameters of the $O_s - O_s$ and $\text{Si} - O_s$ interactions are derived from different potential energy surfaces, giving different errors for the fits. These errors are in eV. Values separated by commas are rms errors for fits of the atomic and shell charges, respectively. The atomic charges of the BJS II potential are not fitted on the dipole moments. The rms error of these charges is determined by calculating the dipole moments of the $(\text{HO})_3\text{SiOSi}(\text{OH})_3$ clusters with the BJS II potential and comparing the results with the *ab initio* dipole moments. The subscripts c and s denote core and shell, respectively.

BJS I				
	A (eV)	ρ (Å)	k ($\text{eV}\text{Å}^{-2}$)	rms error
$O_s - O_s$	266757.00	0.173411	34.98	0.10
$\text{Si} - O_s$	18122.00	0.17077		0.28
$O_c - O_s$				–
	q_{Si}	q_{O_s}	q_{O_c}	
	2.7226	-2.0125	0.6512	$2.5 \cdot 10^{-4}$, $8.9 \cdot 10^{-5}$
BJSM				
	A (eV)	ρ (Å)	k ($\text{eV}\text{Å}^{-2}$)	rms error
$O_s - O_s$	318006.00	0.170185	33.52	0.11
$\text{Si} - O_s$	9797.82	0.185087		0.31
$O_c - O_s$				–
	q_{Si}	q_{O_s}	q_{O_c}	
	2.7706	-2.0948	0.7095	$6.0 \cdot 10^{-6}$, $6.1 \cdot 10^{-6}$
BJS II				
	A (eV)	ρ (Å)	k ($\text{eV}\text{Å}^{-2}$)	rms error
$O_s - O_s$	4591190.00	0.139636	33.52	0.08
$\text{Si} - O_s$	5086.63	0.212366		0.35
$O_c - O_s$				–
	q_{Si}	q_{O_s}	q_{O_c}	
	3.0906	-2.0948	0.5495	0.19, $8.2 \cdot 10^{-6}$

Although these differences may seem small (see Table 4.1) they have a pronounced effect on the predictive power of the potentials. Table 4.2 presents calculated and experimental structures of α -quartz at ambient conditions. The α -quartz structure calculated with the BJSM potential is not very accurate. The Si-O distances are too large and the Si-O-Si bond angle is substantially underestimated. The overestimated Si-O distances might be due to the underestimated Si-O-Si bond angle [15]. In an attempt to remedy this effect, we modified the BJSM potential by the addition of an Si-Si repulsion term. We derived this term from fits on MP2-calculated potential energies of the $(\text{HO})_3\text{SiOSi}(\text{OH})_3$ cluster. (This potential energy surface is computed with the same basis sets and cluster geometries as used in the calculations of the *ab initio* dipole moments and polarizabilities of the $(\text{HO})_3\text{SiOSi}(\text{OH})_3$ clusters. For the latter see Ref. 10.) With the modified BJSM potential we calculated the structure of α -quartz. The structure is not in agreement with experiment because the Si-O-Si bond angle and Si-O bond distances are substantially overestimated. As a consequence, the structure has the wrong symmetry ($P6_222$), which is the symmetry of idealized β -quartz.

Table 4.2. Predicted and experimental [23] structures of α -quartz at room temperature. Lengths are in \AA and angles in degrees. The symbol l denotes the largest distance or angle and s the smallest distance or angle.

Property	Expt.	BJS I	BJSM	BJS II	KFBS	JC
a	4.914	4.772	4.656	4.878	4.963	4.855
c	5.405	5.232	5.123	5.367	5.468	5.362
u	0.469	0.460	0.456	0.472	0.467	0.465
x	0.415	0.395	0.384	0.407	0.428	0.409
y	0.272	0.288	0.298	0.264	0.268	0.275
z	0.120	0.094	0.081	0.118	0.128	0.111
$d_{\text{Si-O}_i}$	1.614	1.623	1.637	1.606	1.606	1.614
$d_{\text{Si-O}_s}$	1.606	1.620	1.635	1.605	1.598	1.607
γ	120.0	120.0	120.0	120.0	120.0	120.0
$\angle_{\text{Si-O-Si}}$	143.6	132.8	125.4	142.0	149.6	139.1
Symmetry	$P3_121$	$P3_121$	$P3_121$	$P3_121$	$P3_121$	$P3_121$

Thus, our attempt to improve the BJS I potential by using pure *ab initio* data did not give satisfactory results so far. Also, the *ab initio* potentials derived (BJS I and BJSM) differ only slightly with respect to the charges, but give substantially different predictions for the structure of α -quartz. We therefore derived a potential (BJS II) for which the atomic charges are optimized on the α -quartz structure and the remaining parameters are fitted on *ab initio* data. (See Sec. 4.4.1.) Parameters of the BJS II potential and errors of the fits are given in Table 4.1. These errors, except for the ones in the atomic charges, are reasonably small. Thus, only the atomic charges of the BJS II potential are not consistent with the *ab initio* dipole moments of the $(\text{HO})_3\text{SiOSi}(\text{OH})_3$ clusters. The atomic charges of our potentials are determined by a single parameter. (See Sec. 4.1.1.) Thus, we optimized one parameter of the BJS II potential on the structure of α -quartz while the remaining parameters are consistent with the *ab initio* data used in the fit. This optimization involved a moderate change in the charge parameter, as the atomic charges of the BJS II potential are only 11% higher than the BJSM values.

4.3.2 Properties of all-silica polymorphs at ambient conditions.

The BJS II potential gives an accurate prediction for the structure of α -quartz at ambient conditions. (See Table 4.2.) This could be expected as the potential is optimized on the experimental structure of α -quartz at 13 K, and this structure changes only slightly when temperature is increased to 300 K [15]. Table 4.3 gives calculated and experimental structures of several all-silica zeolites with substantially different geometries than α -quartz. Predictions of the BJS II potential for these structures are significantly closer to experiment than those of the BJS I potential.

Table 4.3. Calculated and experimental structures of all-silica zeolites. Cubic faujasite is abbreviated as FAU, monoclinic zsm-5 as zsm-5-m. These large structures were calculated at absolute zero. The results are compared with experimental data at room temperature, thereby assuming that the structures do not change much between 0 and 300 K. References denote experiment. Lengths are in Å and angles in degrees.

Property	Expt.	BJS I	BJS II	KFBS	JC
FAU [27]					
a	24.26	23.87	24.11	24.78	24.23
α	90.00	90.0	90.0	90.0	90.0
d_{Si-O_s}	1.597	1.608	1.591	1.600	1.599
d_{Si-O_t}	1.616	1.62	1.616	1.620	1.614
$\langle d_{Si-O} \rangle$	1.606	1.616	1.604	1.609	1.607
$\angle_{Si-O-Si_s}$	138.4	133.5	135.6	143.3	137.6
$\angle_{Si-O-Si_t}$	149.4	139.8	150.0	160.4	148.9
$\langle \angle_{Si-O-Si} \rangle$	143.7	136.4	142.6	152.7	143.3
\angle_{O-Si-O_s}	108.0	102.4	106.2	104.8	107.5
\angle_{O-Si-O_t}	111.5	114.4	112.4	116.0	112.0
Symmetry	$Fd\bar{3}m$	$Fd\bar{3}m$	$Fd\bar{3}m$	$Fd\bar{3}m$	$Fd\bar{3}m$
zsm-5-m [28]					
a	20.10	19.57	19.97	20.38	19.98
b	19.88	19.27	19.75	20.34	19.74
c	13.37	13.03	13.20	13.68	13.32
α	90.44	90.8	90.36	90.0	90.53
d_{Si-O_s}	1.583	1.589	1.580	1.594	1.591
d_{Si-O_t}	1.608	1.631	1.603	1.622	1.613
$\langle d_{Si-O} \rangle$	1.595	1.611	1.592	1.606	1.601
$\angle_{Si-O-Si_s}$	141.2	128.5	139.6	149.9	138.8
$\angle_{Si-O-Si_t}$	169.0	155.4	170.5	177.6	166.5
$\langle \angle_{Si-O-Si} \rangle$	153.9	130.0	151.0	162.1	148.8
\angle_{O-Si-O_s}	107.10	99.73	103.9	105.3	104.5
\angle_{O-Si-O_t}	111.63	117.0	113.4	114.9	112.72
Symmetry	$P2_1/c$	$P2_1/c$	$P2_1/c$	$Pnma$	$P2_1/c$

Elsewhere [14] we show that the BJS II potential gives accurate predictions for a large number of all-silica structures having densities between those of α -quartz

and the molecular sieve cubic faujasite. The accuracy of these predictions is higher than that of the KFBS potential and comparable to results of the JC potential [14]. The BJS II potential predicts only the structure of the high-density systems stishovite and coesite less accurately than the other potentials [14]. Thus, the partial optimization of the BJS II potential on the structure of α -quartz gives improved predictions for a large number of structures.

We further investigated the accuracy of BJS II predictions for properties other than the structure. Table 4.4 presents calculated and experimental values for the dielectric and elastic constants of α -quartz at ambient conditions. The BJS II potential underestimates the dielectric constants, similar to the BJS I potential. The reason for this has been found recently by Schober *et al.* [29,30]. These authors derived analytical expressions for the dielectric constants of α -quartz described with a shell model in which the oxygen atoms are polarized. They showed that atomic charges of such a model must be close to the formal values in order to obtain a correct prediction for the dielectric constants of α -quartz. Consistently we find that the JC potential, which is based on formal charges, predicts these constants accurately (see Table 4.4). This is a major problem for the derivation of *ab initio* shell model potentials because it is well-known that charges derived from *ab initio* calculations, irrespective whether they are done on clusters or crystals, have lower values than the formal charges. The elastic constants of α -quartz calculated with the BJS II potential are less satisfactory than those predicted by the other potentials. In particular, the C_{33} is underestimated. (See Table 4.4.)

Table 4.4. Predicted and experimental properties of α -quartz at room temperature. Experimental elastic constants are from Ref. [24]. Experimental values of the dielectric constants are from Refs. [25] and [26]. Lengths are in Å and angles in degrees. Elastic constants C_{ij} are in 10^{10}N/m^2 . Low-frequency dielectric constants are denoted as ϵ_{ij}^0 and high-frequency dielectric constants as ϵ_{ij}^∞ .

Property	Expt.	BJS I	BJS II	KFBS	JC
C_{11}	8.68	8.78	8.50	8.96	9.52
C_{12}	0.70	1.38	0.21	0.39	1.62
C_{13}	1.91	0.92	0.37	1.16	1.86
C_{14}	-1.80	-1.82	-2.15	-1.85	-1.51
C_{33}	10.58	10.72	8.57	9.95	11.51
C_{44}	5.82	5.51	4.57	4.92	5.10
C_{66}	3.99	3.70	3.23	4.28	3.95
ϵ_{11}^0	4.52	2.40	2.62	1.93	4.72
ϵ_{33}^0	4.64	2.45	2.75	1.98	5.01
ϵ_{11}^∞	2.36	1.79	1.81	—	2.11
ϵ_{33}^∞	2.36	1.80	1.82	—	2.13

That the BJS II potential is not suitable for modeling elasticity is further indicated by predicted elastic constants of stishovite and coesite which are less accurate than the KFBS and BJS I predictions. Calculated and experimental elastic constants of these materials are given in Table 4.5.

Table 4.5. Calculated and experimental elastic constants of coesite and stishovite at room temperature. References denote experiment. Elastic constants C_{ij} are in 10^{10}N/m^2 .

Property	Expt.	BJS I	BJS II	KFBS	JC
coesite [31]					
C_{11}	16.08	11.97	6.20	17.30	9.32
C_{12}	8.21	6.15	6.24	8.21	6.26
C_{13}	10.29	6.45	6.86	10.60	7.42
C_{15}	-3.62	-1.17	0.17	-2.93	0.47
C_{22}	23.04	21.37	19.33	24.89	21.05
C_{23}	3.56	5.53	6.30	8.72	6.60
C_{25}	0.26	1.78	1.86	0.98	2.17
C_{33}	23.16	22.20	18.90	27.83	23.96
C_{35}	-3.93	-5.51	-8.09	-4.80	-6.03
C_{44}	6.78	5.13	3.90	2.77	3.36
C_{46}	0.99	1.24	0.44	-0.83	0.70
C_{55}	7.33	4.49	3.29	5.90	4.77
C_{66}	5.88	4.13	2.91	3.92	3.95
stishovite [32]					
C_{11}	45.3	67.8	87.4	62.5	47.5
C_{12}	21.1	34.8	50.3	22.8	30.4
C_{13}	20.3	41.2	44.0	26.8	36.1
C_{33}	77.6	98.9	102.9	93.3	86.6
C_{44}	25.2	26.8	31.9	26.9	14.7
C_{66}	30.2	37.9	51.7	26.1	39.6

We conclude that the BJS II potential is suitable for the modeling of all-silica structures at ambient conditions, similar to the JC potential. The BJS II potential is less appropriate for studies on the elasticity of these systems, in contrast to the KFBS and BJS I potential.

4.3.3 Properties of α -quartz at elevated pressures.

In previous work [15] we analyzed predictions of the BJS I, KFBS and JC potential for the structure and mechanical properties of α -quartz at variable pressures. Here we follow a similar analysis of the BJS II predictions. We will emphasize the differences between the BJS I and BJS II potential. The properties of α -quartz are calculated up to pressures at which acoustic mode softening is predicted. Predicted values of the BJS I and BJS II potential for these pressures are 24.1 and 6.5 GPa, respectively. The latter value is far too low as will be discussed later.

Table 4.6 presents calculated and experimental Si-O bond angles of α -quartz at variable pressures. The computed pressure-induced changes of these bond angles are less than 1% and compare reasonably with experiment. Hence, we can discuss predictions for the α -quartz structure by considering changes of the bond angles and their correlations with the cell-axes compression. These correlations are explained elsewhere [15].

Table 4.6. Room temperature predictions for Si-O bond distances in α -quartz at variable pressures, compared with experiment [33,34]. P denotes pressure, r_l the longest Si-O bond distance and r_s the shortest Si-O bond distance. Distances are in \AA and pressures in GPa.

	Expt.		BJS I		BJS II	
P	r_l	r_s	r_l	r_s	r_l	r_s
0.0	1.614	1.606	1.623	1.620	1.606	1.605
5.1	1.623	1.604	1.634	1.628	1.627	1.621
9.5	1.621	1.596	1.639	1.639	—	—

Figures 4.1 and 4.2 illustrate calculated and experimental values for the c -axis and Si-O-Si bond angle at variable pressures. The BJS II-predicted Si-O-Si bond angle and correlated [15] c -axis decrease too fast with pressure. Thus, the interactions of the BJS II potential which determine the Si-O-Si bond angle are too weak at shorter interatomic distances.

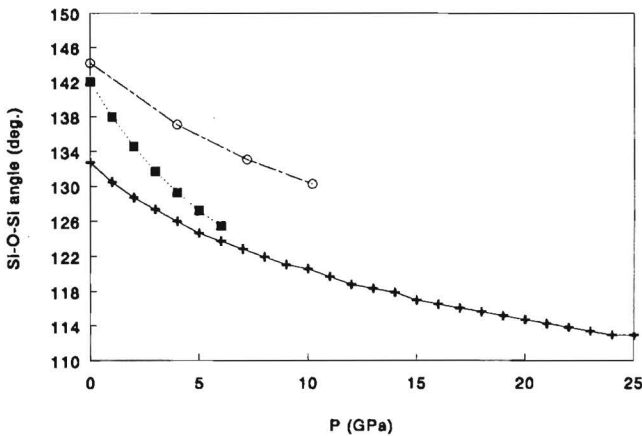


Figure 4.1. Predictions for the Si-O-Si bond angle in α -quartz at variable pressures and room temperature, compared with experimental data of Glinneman *et al.* [33]. Crosses: BJS I predictions. Squares: BJS II predictions. Open points: experimental data [33].

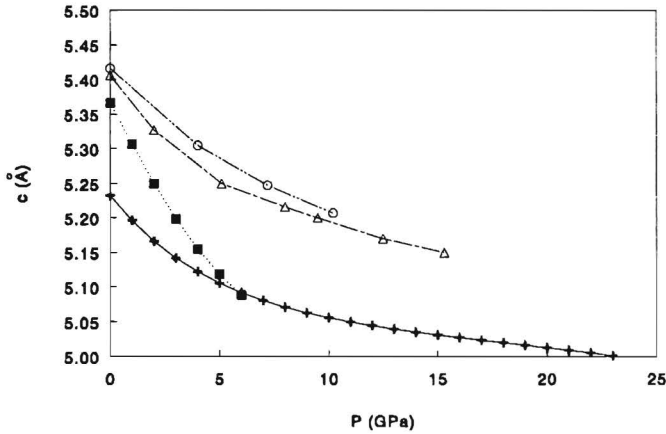


Figure 4.2. Room temperature predictions for the c -axis of α -quartz at variable pressures, compared with experimental data of Glinneman *et al.* [33] and Hazen *et al.* [34]. Crosses: BJS I predictions. Squares: BJS II predictions. Open points: data of Glinneman *et al.* Open triangles: data of Hazen *et al.*

Figure 4.3 illustrates calculated and experimental values for the a -axis at variable pressures. The a -axis calculated with the BJS II potential decreases too fast with pressure, indicating that the O-O repulsions are too weak at short interatomic distances [15]. This is also apparent from the overestimated distortion of the O-Si-O angles, illustrated in Fig. 4.4.

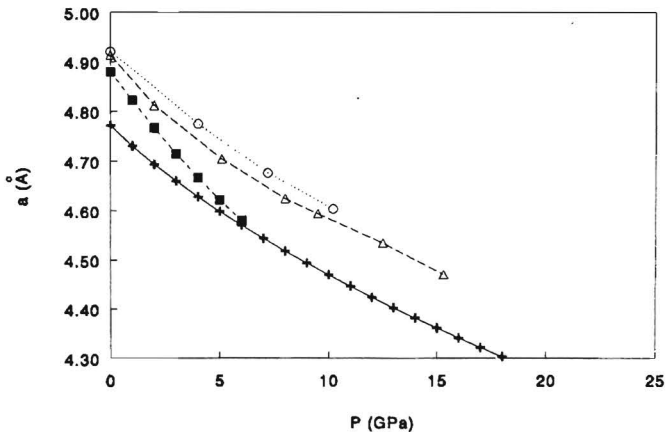


Figure 4.3. Predictions for the a -axis of α -quartz at variable pressures and room temperature compared with experiment [33,34]. Symbols are the same as in Fig. 4.2.

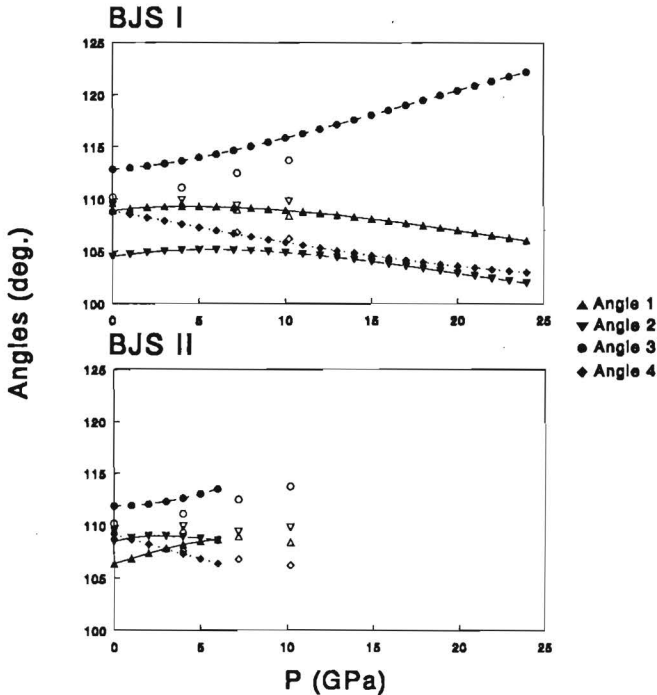


Figure 4.4. Calculated and experimental values for the tetrahedral bond angles in α -quartz at variable pressures and room temperature. Closed symbols: Calculations. Open symbols: experiment [33].

The underestimation of the c -axis becomes larger than that of the a -axis at higher pressures, causing an underestimation of the c/a ratio. This indicates that the BJS II-predicted crystal is relative too soft in the c -direction at elevated pressures. At zero pressure this was apparent from the underestimated value of the C_{33} (see Sec. 4.3.2) and this situation remains thus unchanged at higher pressures. This causes incorrect predictions for the mechanical stability of the crystal, as will be shown next. The BJS II potential predicts that the lowest acoustic mode along $[0\ 0\ \xi]$ softens at the A point when α -quartz is subjected to a pressure of 6.5 GPa. This indicates formation of a supercell that is different from the $3 \times 3 \times 1$ superstructure reported [35] for α -quartz at 21 GPa. At a pressure slightly above 6.5 GPa, the BJS II potential predicts imaginary frequencies close to the Γ point for phonons along $[0\ 0\ \xi]$, indicating that the structure becomes mechanically unstable [36]. This pressure is far too low when compared with the experimental amorphization pressures that range from 15 to 35 GPa [34,37]. The computed mode softening along $[0\ 0\ \xi]$ is inconsistent with violation of the Born stability criteria of α -quartz [15] and the predicted supercell formation is therefore not correct. The calculated mode softening along $[0\ 0\ \xi]$ is consistent with the relative softness in the c -direction of the predicted crystal. Thus, the BJS II potential can not describe the behavior of α -quartz at elevated pressures, in contrast to the BJS I potential. We have shown earlier [15] that the BJS I potential gives satisfactory predictions for the

mechanical properties of α -quartz up till high pressures, although the structure of this material is predicted less accurately. This could be explained from a systematic underestimation of both the Si-O-Si bond angle and O-O repulsions at variable interatomic distances, i.e. at variable pressures. The effect of the underestimated Si-O-Si bond angle on the elasticity of α -quartz is systematically compensated by too weak O-O repulsions [15]. The BJS II potential underestimates these quantities less systematically than the BJS I potential: Bond angles and cell-axes calculated with the former potential are close to experiment at zero pressure but gradually approach the BJS I values at higher pressures. (See Figs. 4.1–4.3.) This reflects the inclusion of α -quartz structure data in the parametrization of the BJS II potential. This has only improved the Si-O-Si bond angle and the O-O repulsions for atomic distances at ambient conditions, but made this potential unsuitable for modeling α -quartz at elevated pressures. The BJS II potential also predicts the elasticity of stishovite and coesite not very accurately. (See Table 4.5.) We therefore expect that this potential is not appropriate for pressure studies of all-silica polymorphs in general.

4.3.4 Properties of α -quartz at elevated temperatures

In this section we will mainly discuss BJS I and BJS II predictions for properties of α -quartz at elevated temperatures. For KFBS and JC results of these calculations we refer to earlier work [15].

According to experiment [23], the Si-O-Si bond angle of α -quartz increases by 2.5° in the range 300–813 K. Values predicted by the BJS I and BJS II potential for this change are 2.3° and 3.8° , respectively. Both potentials predict that the largest change of the tetrahedral bond angles is less than one degree, when temperature is increased from 300 to 813 K. This agrees with experiment [23]. Predictions of the BJS II potential for the Si-O bond distances in α -quartz at variable temperature are the closest to experiment. Table 4.7 presents calculated and experimental values for these bond distances.

Table 4.7. Calculated and experimental [23] Si-O bond distances of α -quartz at several temperatures. T denotes temperature, r_l the longest and r_s the shortest Si-O bond distance. Distances are in Å and temperatures in K.

T	Expt.		BJS I		BJS II	
	r_s	r_l	r_s	r_l	r_s	r_l
300	1.605	1.614	1.620	1.622	1.604	1.606
813	1.600	1.594	1.618	1.621	1.600	1.601

Preliminary calculations on several all-silica zeolites at variable temperatures indicate that the BJS II potential can also model thermal changes of other structures than α -quartz. These results are given in Table 4.8. For all but one of the studied zeolites, the BJS II potential predicts a temperature-induced *contraction*. This contraction is also predicted by the JC potential for 16 different all-silica zeolites [43]. Experimentally this was found for Na-zeolite X, which has the cubic faujasite structure [44].

Table 4.8. BJS II predictions and experimental values for the unit cell parameters of all-silica zeolites at variable temperatures. Chabazite is denoted by CHA and brewsterite by BRE. Lengths are in Å and angles in degrees. References denote experiment.

Property	Expt.	0 K	300 K	500 K
CHA [38] †				
<i>a</i>	9.441	9.144	9.134	9.126
α	93.1	94.7	94.8	95.0
Symmetry	$R\bar{3}m$	$R\bar{3}m$	$R\bar{3}m$	$R\bar{3}m$
zsm-18 [39]				
<i>a</i>	13.18	12.97	12.96	12.94
<i>c</i>	15.85	15.49	15.48	15.47
γ	120.0	120.0	120.0	120.0
Symmetry	$P6_3/m$	$P6_3/m$	$P6_3/m$	$P6_3/m$
zsm-22 [40]				
<i>a</i>	13.89	13.81	13.84	13.85
<i>b</i>	17.42	17.37	17.40	17.41
<i>c</i>	5.03	5.032	5.049	5.056
α	90.0	90.0	90.0	90.0
Symmetry	$Cmc2_1$	$Cmc2_1$	$Cmc2_1$	$Cmc2_1$
BRE [41,42] †				
<i>a</i>	6.8	6.696	6.692	6.688
<i>b</i>	17.5	16.94	16.93	16.92
<i>c</i>	7.7	7.585	7.581	7.576
β	95	95.2	95.1	95.1
Symmetry	$P2_1/m$	$P2_1/m$	$P2_1/m$	$P2_1/m$

† We are aware of experimental values for Al containing samples only. Calculated all-silica unit cells are smaller than experiment as argued elsewhere [14].

We further investigated the accuracy of BJS II predictions for properties other than the structure at variable temperatures. The BJS II potential underestimates some of the room temperature elastic constants of α -quartz (see Table 4.4). Predicted constants at 400 K deviate similarly from experiment, indicating that this potential is less appropriate for modeling the elasticity at variable temperatures. Figure 4.5 illustrated calculated and experimental low-frequency phonon dispersion curves of α -quartz. Predictions of the BJS II potential for the highest frequencies in these diagrams are less satisfactory than those of the BJS I potential. This also applies for the lowest acoustic branch along $[0\ 0\ \xi]$. The remaining computed frequencies are in reasonable agreement with experiment. These predictions are more accurate than those of the KFBS potential [15] and comparable to results of the BJS I and JC potential [15]. The same applies for predictions of the constant-pressure heat capacity of α -quartz, illustrated in Fig. 4.6, because low-frequency phonons mainly determine the thermodynamical properties.

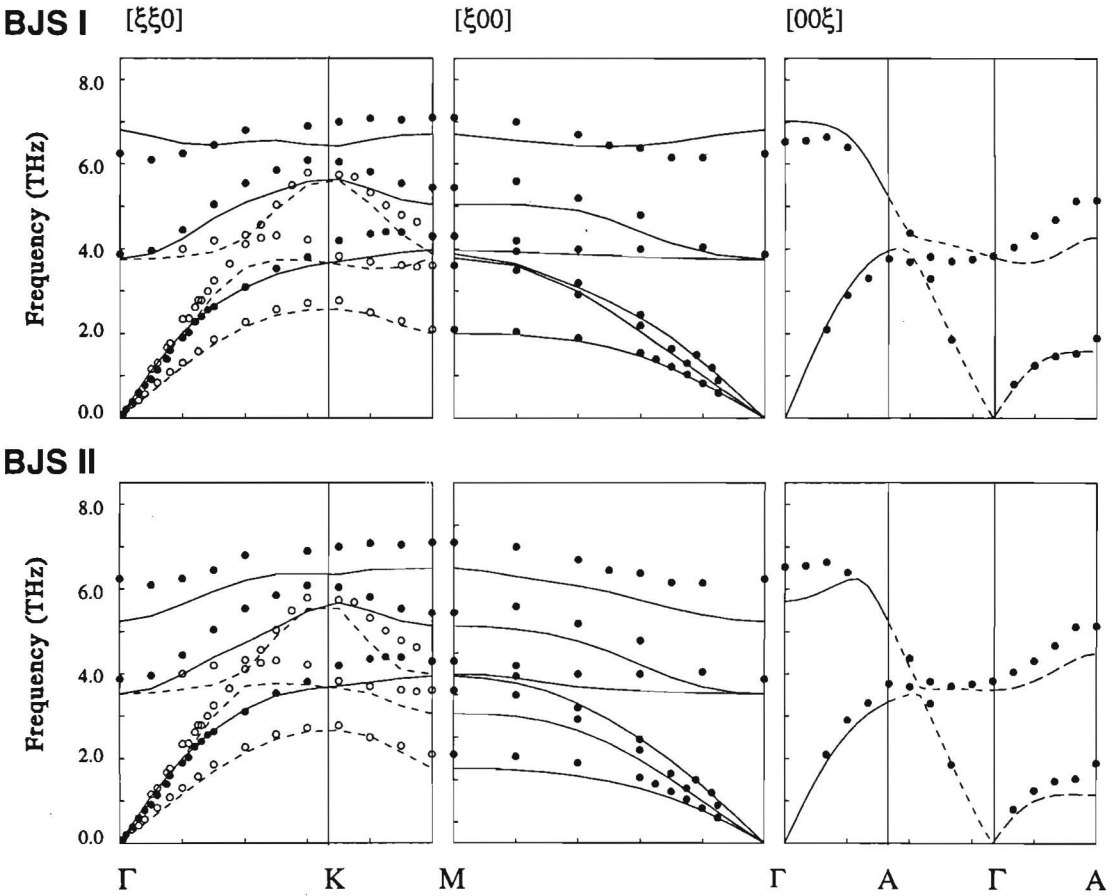


Figure 4.5. Calculated low-frequency phonon dispersion curves in the main directions of α -quartz in comparison with experiment. The $[\xi \xi 0]$ and $[\xi 0 0]$ direction are measured by Dorner *et al.* at $T = 300$ K [45] and calculations were done at this temperature. The $[0 0 \xi]$ direction is measured by Strauch *et al.* [46] at $T = 20$ K and calculations were done at 0 K. Lines: calculations. Points: measurements. In $[\xi \xi 0]$ direction: open points and broken lines show the T2 representation, closed points and straight lines show the T1 representation. For the $[0 0 \xi]$ direction an extended zone scheme is used.

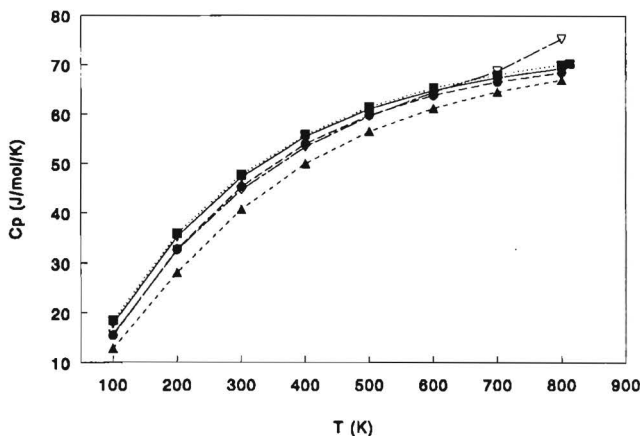


Figure 4.6. Calculated and experimental values for the constant-pressure heat capacity of α -quartz at variable temperatures. Crosses: BJS I predictions. Closed squares: BJS II predictions. Closed triangles: KFBS predictions. Closed points: JC predictions. Open triangles: experimental data [47]. (The BJS I and BJS II predictions are identical. The JC predictions virtually coincide with the experimental data.)

Our results indicate that the partial fit on the α -quartz structure in the parametrization of the BJS II potential has only a minor influence on the predicted phonon dispersion curves and heat capacity of α -quartz. As the BJS II potential also predicts a thermal contraction for several zeolites, we expect that this potential is able to model properties of all-silica polymorphs at variable temperatures. This potential is expected to be less suitable for modeling the elasticity of these materials at any temperature.

4.4 Conclusions

4.4.1 Parametrization procedure

Application of our parametrization procedure to *ab initio* data calculated with different methods, gives two potentials (BJS I and BJS II) that differ only slightly with respect to the charges. These small differences have a negative effect on the predicted Si-O-Si bond angle in α -quartz, however. The addition of an *ab initio* Si-Si repulsion term did not remedy this effect since the resulting potential predicts an incorrect symmetry for α -quartz. We also found that optimization of only one charge parameter on the α -quartz structure and fits of the remaining parameters on *ab initio* data yields a potential (BJS II) which gives satisfactory predictions for the structure and other studied properties of all-silica polymorphs at variable temperatures. The differences between the optimized charges and the *ab initio* values are not very large, indicating that our parametrization procedure is interesting enough for future research.

4.4.2 The BJS II potential

Predictions of the BJS II potential for substantially different structures are closer to experiment than the BJS I results. Thus, the partial optimization on the α -quartz structure in the parametrization of the BJS II potential has also improved the predictions for other structures. The structure predictions of the BJS II potential are more accurate than those of the KFBS potential and comparable to the JC results. Our calculations further indicate that the BJS II potential can model phonon dispersion curves and thermodynamical properties of all-silica systems at variable temperatures, similar to the JC and BJS I potential. The BJS II potential is less suitable for modeling the elasticity and the pressure behavior of those systems, in contrast to the KFBS and BJS I potential. The latter is due to the partial optimization of the BJS II potential on structure data of α -quartz at zero pressure. This has stiffened the Si-O-Si bond angle interactions and O-O repulsions for interatomic distances normally occurring in silicates, whereas at shorter distances these interactions remain too weak. Further improvement of the BJS II potential remains a future task.

4.5 References

- [1] J. Chelikowsky, N. Troullier, J.L. Martins and H.E. King, *Phys. Rev. B* **44**, 489 (1991).
- [2] N. Binggeli, N. Troullier, J.L. Martins and J. Chelikowsky, *Phys. Rev. B* **44**, 4771 (1991).
- [3] N. Binggeli and J. Chelikowsky, *Phys. Rev. Lett.* **69**, 2220 (1992).
- [4] N.R. Keskar and J.R. Chelikowsky, *Phys. Rev. B* **46**, 1 (1992).
- [5] N. Binggeli, N.R. Keskar and J.R. Chelikowsky, *Phys. Rev. B* **49**, 3075 (1994).
- [6] J.R. Chelikowsky and N. Binggeli, *Comp. Mater. Sc.* **2**, 111 (1994) and references therein.
- [7] X. Gonze, J.C. Charlier, D.C. Allan and M.P. Teter, *Phys. Rev. B* **50**, 13035 (1994).
- [8] C. Lee and X. Gonze, *Phys. Rev. B* **72**, 1686 (1994).
- [9] C. Lee and X. Gonze, *Phys. Rev. B* **51**, 8610 (1995).
- [10] K. de Boer, A.P.J. Jansen and R.A. van Santen, *Chem. Phys. Lett.* **223**, 46 (1994), *Chapter 2 of this thesis*.
- [11] R.A. Jackson and C.R.A. Catlow, *Mol. Simul.* **1**, 207 (1988).
- [12] G.J. Kramer, N.P. Farragher, B.W.H. van Beest and R.A. van Santen, *Phys. Rev. B* **43**, 5068 (1991).
- [13] S. Tsuneyuki, M. Tsukada, H. Aoki and Y. Matsui, *Phys. Rev. Lett.* **61**, 869 (1988).
- [14] K. de Boer, A.P.J. Jansen and R.A. van Santen, *Phys. Rev. B* **52**, 12579 (1995), *Chapter 5 of this thesis*.
- [15] K. de Boer, A.P.J. Jansen, R.A. van Santen, S.C. Parker and G.W. Watson, *Phys. Rev. B*, *in press*, (*Chapter 3 of this thesis*).
- [16] G.A. Lager, J.D. Jorgensen and F.J. Rotella, *J. Appl. Phys.* **53**, 6751 (1982).
- [17] S.C. Parker, computercode: PARAPOCS, BATHPROGS, School of Chemistry, University of Bath, Claverton Down, Bath BA2 7AY, U.K.
- [18] S.C. Parker and G.D. Price, *Advances in Solid-State Chem.* **1**, 295 (1989).
- [19] C.R.A. Catlow and M.J. Norgett, *Lattice Structure and Stability of Ionic Materials*, private communication.
- [20] A. Pavesi, private communication.
- [21] P. Tschaufeser, PhD. thesis, University of Bath, Bath (1992).
- [22] G.J. Kramer, A.J.M. de Man and R.A. van Santen, *J. Am. Chem. Soc.* **113**, 6435 (1991).
- [23] K. Kihara, *Europ. J. Mineral.* **2**, 63 (1990).
- [24] H.J. Mc Skimin, P. Andreat and R.N. Thurston, *J. Appl. Phys.* **36**, 1624 (1965).
- [25] J. Fontanella, C. Andeen, D Schuele, *J. Appl. Phys.* **45**, 2852 (1974).
- [26] W.G. Spitzer, D.A. Kleinman, *Phys. Rev.* **121**, 1324 (1961).
- [27] J.A. Hriljac, M.M. Eddy, A.K. Cheetham, J.A. Donahue and G.J. Ray, *J. Solid State Chem.* **106**, 66 (1993).
- [28] H. van Koningsveld, J.C. Jansen and H. van Bekkum, *Zeolites* **10**, 235 (1990).
- [29] H. Schober, D. Strauch, K. Nützel and B Dorner, *J. Phys. Condens. Matter* **5**, 6155 (1993).
- [30] H. Schober and D. Strauch, *J. Phys. Condens. Matter* **5**, 6165 (1993).
- [31] D.J. Weidner and H.R. Carleton, *J. Geophys. Res.* **82**, 1334 (1977).
- [32] W. Sinclair and A.E. Ringwood, *Nature (London)* **78**, 714 (1978).
- [33] J. Glinneman, H.E. King Jr., H. Schultz, Th. Hahn, S.J. La Placa and F. Dacol, *Z. Kristallogr.* **198**, 177 (1992).

- [34] R.M. Hazen, L.W. Finger, R.J. Hemley, and H.K. Mao, *Solid State Commun.* **507** (1989).
- [35] K.J. Kingma, R.J. Hemley, H.H. Mao and D.R. Veblen, *Phys. Rev. Lett.* **70**, 3927 (1993).
- [36] M. Born and K. Huang, *Dynamical Theory of Crystal Lattices, The international series of monographs on physics*, edited by D.H. Wilkinson and W. Marshall (Clarendon press, Oxford, 1968).
- [37] R.J. Hemley, A.P. Jephcoat, H.K. Mao L.C. Ming and M.H. Manghnani, *Nature (London)* **334**, 52 (1988).
- [38] J.V. Smith, F. Rinaldi and L.S. Dent Glasser, *Acta Cryst.* **16**, 45 (1963).
- [39] S.L. Lawton and W.J. Rohrbaugh, *Science* **247**, 1319 (1990).
- [40] B. Marler, *Zeolites* **7**, 393 (1987).
- [41] A.J. Perrotta and J.V. Smit, *Acta Cryst.* **17**, 857 (1964).
- [42] J.L. Schlenker, J.J. Pluth and J.V. Smit, *Acta Cryst.* **B33**, 2907 (1977).
- [43] P. Tschaufeser and S.C. Parker, *J. Phys. Chem.* **99**, 10609 (1995).
- [44] J.W. Couves, R.H. Jones, S.C. Parker, P. Tschaufeser and C.R.A. Catlow, *J. Phys. Condens. Matter* **5**, L329 (1993).
- [45] B. Dorner, H. Grimm and H. Rzyany, *J. Phys. C: Solid St. Phys.* **13**, 6607 (1980).
- [46] D. Strauch and B. Dorner, *J. Phys. Condens. Matter* **5**, 6149 (1993).
- [47] P. Richet, Y. Bottinga, L. Denielou, J.P. Petit and C. Tepui, *Geoch. Cosmochem. Acta* **46**, 2639 (1982).

Chapter 5

Structure-stability relationships for all-silica polymorphs.

Abstract

We discuss predictions for the stability and structures of all-silica zeolitic structures. We present a new shell model potential, which is based on *ab initio* calculations. The new shell model potential gives good predictions for the structure and stability of all-silica structures. We compare three shell model predictions with two rigid-ion model predictions for the structure and stability of silicates. We found that shell model predictions for the relative stability of zeolites are much closer to experiment than those of the rigid-ion model potentials. This is due to the canceling of covalent and electrostatic terms in the shell models which does not occur in the rigid-ion models. Using the potentials with the highest predictive power on both stabilities and structures of silicates, we discuss structure-stability relationships that have been proposed in literature.

5.1 Introduction

The synthesis of high silica zeolites is important for catalysis because of their thermal, hydrothermal and acidic stabilities, good resistance to aging and hydrophobicity which favors the reaction with organic molecules [1]. Although many pure and high-silica zeolites have been reported [2], the relation between crystal structure and thermodynamics is still poorly understood. Insight into the factors that govern the relative stability of silica zeolites is important for their synthesis, which is still a difficult process [2]. Modeling provides a powerful tool for gaining that insight. Experimentally observed relations [3..8] between structure and stability can be tested more thoroughly, because structures can be modeled that have not been synthesized yet. The calculated data and the structure are consistent, whereas sometimes in literature [9] measured enthalpies on alumina free compounds are correlated with data on the structure of materials that contain alumina. This is due to the lack of experimental data on pure-silica structures. Furthermore, the structure of only a few compounds has been determined with single-crystal diffraction. Most structures are determined with X-ray powder diffraction, which is considered less reliable [9]. Given a good potential, structures can be predicted which are more accurate than those obtained from X-ray powder measurements [10].

In this paper, we will discuss predictions for the stabilities and structures for pure-silica zeolites. First we will present a new shell model potential which gives very accurate structure predictions and reasonable predictions for the stability of zeolites. This *ab initio* based potential will be denoted as the BJS II potential. The BJS II potential is a modified version of the BJS I potential, which we have derived earlier [11]. Furthermore, we make an extensive comparison between predictions of the BJS I and BJS II potential and those of three other interatomic potentials. We will compare predictions of our shell model potentials with those of the potential derived by Catlow *et al.* [7], denoted as the JC potential. We will also compare predictions of our potentials with those of the rigid-ion model potentials derived by Kramer *et al.* [13] and Tsuneyuki *et al.* [14]. The latter potentials will be denoted as the KFBS and TTA potential, respectively. We find that the BJS I, BJS II and JC shell model predictions for the stability of zeolites are closer to experiment than the rigid-ion model predictions. We will show that this is caused by the partial canceling of covalent and electrostatic energy terms in the shell model, which does not occur in the rigid-ion model. Furthermore, we will use the BJS II and JC potential for the exploration of hypothetical structures and structure-stability relationships. These potentials predict, in contrast to other modeling studies [8,15], that there is no direct correlation between the density and the relative stability of silica polymorphs. This agrees with recent measurements. The potentials also predict that stabilization of low-density silicates must be caused by small Si-O-Si bond angles in those structures. This supports the conclusion of Petrovic *et al.* [9]. Our results further indicate for a large number of structures that there is no *linear* relationship between the percentage of angles smaller than or equal to 140° and the amount of destabilization. This relationship was suggested by Petrovic *et al.* [9].

5.2 Computational details

5.2.1 Structures

We have studied the following compounds which have been synthesized in pure or high-silica form: α -quartz [16], coesite [17], zsm-11 [19], zsm-12 [20], zsm-18 [21], cubic faujasite [22], monoclinic zsm-5 [23], ssz-24 [24] and zsm-22 [25]. These materials include the compounds for which the enthalpies have been measured recently [9]. In order to study structure-stability relations more thoroughly we have considered some hypothetical all-silica structures in the low-density region. These structures were derived from the original ones by replacing Al, Be or Zn by Si and deleting the compensations cations or water. The original structures are: thomsonite [26], chabazite [27], lovdarite [28], vpi-7 [29] and hexagonal faujasite [30]. We have also studied compounds that have been synthesised with varying Al/Si ratio. (See Refs. 18–31.). Those compounds are treated as purely siliceous in our calculations. The calculations are done using the above structures as starting structures.

5.2.2 Calculations

The minimizations are done with the THBREL code [33] which is based on lattice dynamics [34] and the use of interatomic potentials. No symmetry constraints are applied during the minimization. THBREL also generates the elastic constant tensor (elastic stiffness tensor) and the high and low frequency dielectric tensor. Using the relaxed structure and the interatomic potential, we have calculated the vibrational spectra with the THBPHON code [35]. The calculated spectra serves as a check on the stability of the structures [10]. We decomposed for each potential the calculated lattice-energy relative α -quartz into covalent and electrostatic contributions. This decomposition is obtained by calculating the energies of the relaxed structures with only the relevant interactions turned on.

5.2.3 Interatomic Potentials

In our calculations we have used the TTA, KFBS and JC potential, which were mentioned in Sect. 5.1. We have used the BJS I and BJS II potential, which have the following form:

$$E^{pot} = \sum_{\substack{i,j \\ i < j}} [A_{ij} \exp\left(\frac{-r_{ij}}{\rho_{ij}}\right) - \frac{C_{ij}}{r_{ij}^6}] + \sum_{\substack{i,j \\ i < j}} \frac{q_i q_j}{r_{ij}} + \frac{1}{2} \sum_i k(r_{i,shell} - r_{i,core})^2 \quad (5.1)$$

The first and second term in Eq. (5.1) constitute the well-known Buckingham form, which describes the covalent interactions between all atoms. The O-O interaction in this term only acts through the shells, the Si-O interaction acts between the O shell and the Si ion. Only the O atom is described as a core and a shell. The Si atom has no shell, only a core. The third term is the Coulomb interaction which describes all electrostatic interactions between cores, between shells, and between cores and shells belonging to different atoms. The fourth term is the harmonic interaction, which acts between core

and shell of the same O atom. The Buckingham parameters of the BJS I potential are derived from fits on *ab initio* potential-energy surfaces of the $\text{Si}(\text{OH})_4$ cluster. The shell and atomic charges are obtained from *ab initio* polarizabilities and dipoles of $(\text{HO})_3\text{SiOSi}(\text{OH})_3$ clusters, respectively. The fit procedures are done iteratively so that the parameter set fits self-consistently all *ab initio* data employed. The derivation of the BJS I potential is given in Ref. 11.

The BJS II potential is a modified version of the BJS I potential. The Buckingham parameters of the BJS II potential are derived as described for the BJS I potential [11]. The shell and atomic charges of the BJS II potential are fitted such that the best structure of α -quartz is obtained. This was necessary to remedy the underestimated Si-O-Si bond angle in the BJS I-predicted structure of α -quartz[11]. The fit procedures which determine the electrostatic and Buckingham parameters are done iteratively in order to obtain a parameter set which fits all data self-consistently. The derivation of the BJS II potential is treated in more detail elsewhere [12]. Parameters of the BJS I and BJS II potential are shown in Table 5.1.

Table 5.1. Parameters of the BJS I and BJS II potential. Charges of the BJS I potential: $q_{\text{Si}}=2.7226$, $q_{\text{O}_s}=-2.0125$, $q_{\text{O}_c}=0.6512$. Charges of the BJS II potential: $q_{\text{Si}}=3.0906$, $q_{\text{O}_s}=-2.0948$, $q_{\text{O}_c}=0.5495$. For both potentials $C = 0$. The subscripts *c* and *s* denote core and shell, respectively.

Interaction	$A(\text{eV})$	$\rho (\text{\AA})$	$k (\text{eV \AA}^{-2})$
BJS I			
$O_s - O_s$	266757.0	0.173411	—
$\text{Si} - O_s$	18122.0	0.17077	—
$O_c - O_s$	—	—	34.98
BJS II			
$O_s - O_s$	4591190.0	0.139636	—
$\text{Si} - O_s$	5086.63	0.212366	—
$O_c - O_s$	—	—	33.52

In our calculations with the TTA, KFBS and JC potential we applied a cutoff of 10 \AA [5,14] for the covalent interactions. The covalent O-O interactions of the BJS I and BJS II potentials are applied with a cutoff of 3.5 \AA , because for larger distances all covalent potential terms are effectively zero. The covalent Si-O interaction of the latter potentials is applied with a cutoff of 2.5 \AA (i.e., in between the nearest and next nearest Si and O neighbors) to simulate a real Si-O bond. Electrostatic interactions are calculated using the Ewald summation.

5.3 Results

We will first discuss predictions of structures, followed by an evaluation of the predicted energies. Using the potentials which predict those quantities the most accurate, we will discuss structure-stability relationships that have been proposed in literature.

5.3.1 Pure silica structures

Table 5.2 presents calculated and experimental all-silica structures. The BJS II and JC predictions for the structure of α -quartz, cubic faujasite, ssz-24, zsm-18, zsm-22 and monoclinic zsm-5 are equally accurate and much closer to experiment than those of the other potentials. The results clearly show that the BJS II prediction for the Si-O-Si bond angle in α -quartz and *other* structures is substantially more accurate than that of the BJS I potential. Both the BJS II and JC potential slightly underestimate the Si-O-Si bond angles in the structures studied. The KFBS and TTA potential overestimate these bond angles.

Table 5.2. Calculated and experimental structures of all-silica polymorphs. Distances are in Å and angles in degrees. Cubic faujasite is abbreviated as FAU. The symbol *l* denotes the largest distance or angle and *s* the smallest distance or angle. References denote experiment.

Property	Expt.	BJS I	BJS II	KFBS	JC	TTA
α -quartz [16]						
<i>a</i>	4.902	4.751	4.854	4.941	4.836	5.018
<i>c</i>	5.400	5.213	5.339	5.449	5.347	5.548
γ	120.0	120.0	120.0	120.0	120.0	120.0
d_{Si-O_s}	1.612	1.621	1.606	1.597	1.608	1.630
d_{Si-O_l}	1.613	1.624	1.608	1.605	1.615	1.642
$\langle d_{Si-O} \rangle$	1.613	1.623	1.607	1.601	1.611	1.636
$\langle \angle Si-O-Si \rangle$	142.4	131.7	140.1	148.5	139.1	146.8
$\angle O-Si-O_s$	108.6	104.6	106.6	107.9	108.3	107.5
$\angle O-Si-O_l$	110.7	112.9	111.9	115.0	111.3	115.7
Symmetry	$P3_121$	$P3_121$	$P3_121$	$P3_121$	$P3_121$	$P3_121$
FAU [22]						
<i>a</i>	24.26	23.87	24.11	24.78	24.23	25.39
α	90.00	90.0	90.0	90.0	90.0	90.0
d_{Si-O_s}	1.597	1.608	1.591	1.600	1.599	1.636
d_{Si-O_l}	1.616	1.62	1.616	1.620	1.614	1.658
$\langle d_{Si-O} \rangle$	1.606	1.616	1.604	1.609	1.607	1.646
$\angle Si-O-Si_s$	138.4	133.5	135.6	143.3	137.6	143.9
$\angle Si-O-Si_l$	149.4	139.8	150.0	160.4	148.9	161.7
$\langle \angle Si-O-Si \rangle$	143.7	136.4	142.6	152.7	143.3	153.7
$\angle O-Si-O_s$	108.0	102.4	106.2	104.8	107.5	104.4
$\angle O-Si-O_l$	111.5	114.4	112.4	116.0	112.0	116.8
Symmetry	$Fd\bar{3}m$	$Fd\bar{3}m$	$Fd\bar{3}m$	$Fd\bar{3}m$	$Fd\bar{3}m$	$Fd\bar{3}m$

(Continued on next page.)

Table 5.2. Continued.

Property	Expt.	BJS I	BJS II	KFBS	JC	TTA
ssz-24 [24]						
<i>a</i>	13.62	13.28	13.59	13.93	13.60	13.77
<i>b</i>	13.62	13.28	13.59	13.93	13.60	14.26
<i>c</i>	8.323	8.07	8.32	8.19	8.31	8.348
α	90.0	90.0	90.0	90.19	90.0	89.86
β	90.0	90.00	90.00	89.66	90.00	90.00
γ	120.0	120.0	120.0	122.1	120.0	118.9
<i>d</i> _{Si-O_s}	1.570	1.609	1.579	1.590	1.595	1.624
<i>d</i> _{Si-O_i}	1.619	1.622	1.601	1.623	1.608	1.660
$\langle d_{Si-O} \rangle$	1.596	1.615	1.593	1.605	1.602	1.641
$\angle Si-O-Si_s$	142.2	134.5	144.3	140.8	144.5	140.3
$\angle Si-O-Si_i$	164.7	140.4	161.3	179.86	154.7	179.5
$\langle \angle Si-O-Si \rangle$	151.3	136.3	150.1	157.5	147.7	158.0
$\angle O-Si-O_s$	96.99	105.6	105.9	104.3	107.8	103.9
$\angle O-Si-O_i$	119.3	115.0	112.6	115.6	111.3	114.8
Symmetry	<i>P6/mcc</i>	<i>P6/m</i>	<i>P6/m</i>	<i>C2/c</i>	<i>P6/m</i>	<i>C2/c</i>
zsm-18 [21]						
<i>a</i>	13.18	12.86	12.97	13.30	13.04	13.63
<i>c</i>	15.85	15.27	15.49	15.95	15.59	16.33
γ	120.0	120.0	120.0	120.0	120.0	120.0
<i>d</i> _{Si-O_s}	1.577	1.569	1.570	1.589	1.588	1.623
<i>d</i> _{Si-O_i}	1.631	1.643	1.638	1.628	1.628	1.668
$\langle d_{Si-O} \rangle$	1.613	1.615	1.604	1.609	1.606	1.645
$\angle Si-O-Si_s$	134.7	125.8	128.5	139.3	131.7	139.8
$\angle Si-O-Si_i$	180.00	180.0	180.0	180.00	180.0	180.0
$\langle \angle Si-O-Si \rangle$	147.4	137.6	143.8	153.4	144.8	154.2
$\angle O-Si-O_s$	105.3	103.5	105.7	100.7	106.6	100.1
$\angle O-Si-O_i$	111.98	114.3	113.4	116.4	112.5	117.1
Symmetry	<i>P6₃/m</i>	<i>P6₃/m</i>	<i>P6₃/m</i>	<i>P6₃/m</i>	<i>P6₃/m</i>	<i>P6₃/m</i>
zsm-22 [25]						
<i>a</i>	13.89	13.41	13.81	13.96	13.87	14.33
<i>b</i>	17.42	17.04	17.37	17.63	17.41	18.14
<i>c</i>	5.03	4.89	5.032	5.094	5.005	5.261
γ	90.0	90.0	90.0	90.0	90.0	90.0
<i>d</i> _{Si-O_s}	1.567	1.583	1.586	1.596	1.592	1.630
<i>d</i> _{Si-O_i}	1.627	1.629	1.597	1.617	1.609	1.656
$\langle d_{Si-O} \rangle$	1.600	1.611	1.591	1.604	1.599	1.640
$\angle Si-O-Si_s$	141.03	127.5	145.70	146.8	143.1	151.2
$\angle Si-O-Si_i$	156.6	158.3	155.6	162.0	153.9	163.4
$\langle \angle Si-O-Si \rangle$	151.3	139.3	151.4	156.3	150.0	158.9
$\angle O-Si-O_s$	107.6	103.5	105.3	106.2	106.2	106.0
$\angle O-Si-O_i$	111.2	115.6	113.0	114.5	112.8	114.9
Symmetry	<i>Cmc2₁</i>	<i>P2₁</i>	<i>Cmc2₁</i>	<i>Cmc2₁</i>	<i>Cmc2₁</i>	<i>Cmc2₁</i>

(Continued on next page.)

Table 5.2. Continued.

Property	Expt.	BJS I	BJS II	KFBS	JC	TTA
zsm-5-m [23]						
<i>a</i>	20.10	19.57	19.97	20.38	19.98	20.89
<i>b</i>	19.88	19.27	19.75	20.34	19.74	20.82
<i>c</i>	13.37	13.03	13.20	13.68	13.32	14.01
α	90.44	90.8	90.36	90.0	90.53	90.0
d_{Si-O_o}	1.583	1.589	1.580	1.594	1.591	1.629
d_{Si-O_i}	1.608	1.631	1.603	1.622	1.613	1.662
$\langle d_{Si-O} \rangle$	1.595	1.611	1.592	1.606	1.601	1.642
$\angle_{Si-O-Si_o}$	141.2	128.5	139.6	149.9	138.8	151.3
$\angle_{Si-O-Si_i}$	169.0	155.4	170.5	177.6	166.5	177.3
$\langle \angle_{Si-O-Si} \rangle$	153.9	130.0	151.0	162.1	148.8	163.0
\angle_{O-Si-O_o}	107.10	99.73	103.9	105.3	104.5	104.9
\angle_{O-Si-O_i}	111.63	117.0	113.4	114.9	112.72	115.5
Symmetry	$P2_1/c$	$P2_1/c$	$P2_1/c$	$Pnma$ †	$P2_1/c$	$Pnma$ †
coesite [17]						
<i>a</i>	7.137	6.832	6.776	7.138	6.806	7.256
<i>b</i>	12.37	12.14	12.36	12.49	12.29	12.76
<i>c</i>	7.174	7.019	7.086	7.271	7.115	7.434
γ	120.3	120.04	121.72	120.76	119.42	121.07
d_{Si-O_o}	1.595	1.566	1.559	1.579	1.569	1.608
d_{Si-O_i}	1.621	1.637	1.635	1.620	1.628	1.657
$\langle d_{Si-O} \rangle$	1.609	1.614	1.609	1.604	1.611	1.638
$\angle_{Si-O-Si_o}$	137.2	126.5	127.9	144.7	132.6	143.9
$\angle_{Si-O-Si_i}$	180.0	180.0	180.0	180.0	180.0	180.0
$\langle \angle_{Si-O-Si} \rangle$	150.8	139.9	142.1	154.4	143.8	153.96
\angle_{O-Si-O_o}	108.0	104.6	103.5	104.3	104.85	104.0
\angle_{O-Si-O_i}	110.4	114.7	114.1	115.7	112.7	116.4
Symmetry	$C2/c$	$C2/c$	$C2/c$	$C2/c$	$C2/c$	$C2/c$

† The TTA and KFBS potentials predict orthorhombic zsm-5 as the most stable form, when both the orthorhombic and monoclinic structure are used as a starting structure. (Continued on next page.)

For ssz-24 both the KFBS and TTA potential predict identical layered structures. These structures are not in accordance with experiment, which has been discussed earlier for the KFBS potential [37]. The TTA and KFBS potential predict for zsm-5 that the high-temperature orthorhombic phase is the most stable. This is not in agreement with the experimental observation that the low-temperature monoclinic phase is the most stable form [23]. Thus, the TTA and KFBS potential show similar behavior. The BJS I and KFBS predictions for the coesite structure are the closest to experiment. This is line with accurate predictions of these potentials for the high pressure behavior of α -quartz [36]. We notice that two structures have been reported for coesite. Kirfel *et al.* [38] reported that

coesite has space group P121/A1 and that the structure does not contain Si-O-Si bond angles of 180°. According to Geisinger *et al.* [17], the coesite structure contains straight Si-O-Si bond angles and has space group C2/c. All potentials predict essentially the latter structure. Also, the high pressure structure stishovite is the most accurately predicted by the KFBS and BJS I potential. The BJS II potential underestimates the long Si-O distances in stishovite. The JC potential overestimates the distortion of the O-Si-O angles in stishovite and predicts the Si-O bond distances less accurately. These results will be further discussed in Sect. 5.3.

Table 5.2. Continued.

Property	Expt.	BJS I	BJS II	KFBS	JC	TTA
stis [18]						
<i>a</i>	4.177	4.089	4.029	4.149	4.025	4.264
<i>c</i>	2.665	2.591	2.638	2.662	2.775	2.747
<i>u</i>	0.306	0.307	0.296	0.305	0.304	0.304
<i>d</i> _{Si-O₂}	1.757	1.751	1.757	1.755	1.782	1.810
<i>d</i> _{Si-O₁}	1.809	1.715	1.689	1.790	1.728	1.836
$\langle d_{Si-O} \rangle$	1.774	1.738	1.734	1.764	1.764	1.818
$\angle_{Si-O-Si}$	130.7	132.2	131.3	130.7	128.8	130.7
\angle_{O-Si-O_1}	81.3	84.5	82.7	81.3	77.7	81.30
\angle_{O-Si-O_2}	180.0	180.0	180.0	180.0	180.0	180.0
\angle_{O-Si-O_3}	90.0	90.0	90.0	90.0	90.0	90.0
\angle_{O-Si-O_4}	98.7	95.5	97.3	98.7	102.3	98.7
Symmetry	<i>P4₂/mnm</i>	<i>P4₂/mnm</i>	<i>P4₂/mnm</i>	<i>P4₂/mnm</i>	<i>P4₂/mnm</i>	<i>P4₂/mnm</i>
zsm-11 [19]						
<i>a</i>	20.07	19.39	19.93	20.47	19.95	20.92
<i>b</i>	20.07	19.66	19.93	20.47	19.95	20.92
<i>c</i>	13.41	13.02	13.34	13.73	14.05	14.04
α	90.0	90.0	90.0	90.0	90.0	90.0
<i>d</i> _{Si-O₂}	1.489	1.540	1.569	1.582	1.580	1.621
<i>d</i> _{Si-O₁}	1.686	1.721	1.602	1.628	1.614	1.665
$\langle d_{Si-O} \rangle$	1.597	1.611	1.591	1.607	1.600	1.643
$\angle_{Si-O-Si_2}$	144.1	129.2	142.8	150.3	141.7	150.8
$\angle_{Si-O-Si_1}$	165.3	172.1	169.0	175.9	163.7	175.9
$\langle \angle_{Si-O-Si} \rangle$	153.3	140.0	151.4	161.6	149.2	162.3
\angle_{O-Si-O_2}	99.7	99.3	104.2	105.9	103.7	104.6
\angle_{O-Si-O_1}	122.9	119.5	113.3	115.8	113.9	116.2
Symmetry	<i>I4m2</i>	<i>P1</i>	<i>I4</i>	<i>I4m2</i>	<i>I4</i>	<i>I4m2</i>

(Continued on next page.)

The JC and BJS II predictions for the unit cell parameters of zsm-11 and zsm-12 are equally accurate and closest to the experiment. However, the smallest Si-O bond distances in these structures are substantially longer than the experimental values. The predicted

largest Si-O bond distances are shorter than the experimental values. The predicted range of O-Si-O angles for zsm-11 is much smaller than indicated by experiment. The BJS II and JC predictions might be closer to the actual values than the experimental data reported so far, for the following reasons: Petrovic *et al.* [9] already noticed that the experimental O-Si-O angles and Si-O bond distances reported for zsm-11 and zsm-12 deviate much from those normally encountered in most reliable single-crystal studies on silicates [9]. It remains to be seen if those distances and angles can be confirmed by further experiments [9].

Table 5.2. *Continued.*

Property	Expt.	BJS I	BJS II	KFBS	JC	TTA
zsm-12 [20]						
a	24.86	24.21	24.95	25.15	24.94	25.80
b	5.012	4.839	5.036	4.937	4.998	5.048
c	24.32	23.63	24.23	23.91	24.16	24.39
β	107.7	107.2	107.6	106.5	107.37	106.8
d_{Si-O_s}	1.526	1.600	1.585	1.596	1.597	1.628
d_{Si-O_i}	1.698	1.625	1.609	1.622	1.610	1.663
$\langle d_{Si-O} \rangle$	1.596	1.615	1.593	1.605	1.602	1.641
$\angle_{Si-O-Si_s}$	134.3	129.2	136.9	137.9	137.7	137.2
$\angle_{Si-O-Si_i}$	158.6	149.9	159.2	167.8	157.3	168.6
$\langle \angle_{Si-O-Si} \rangle$	150.3	136.5	149.8	151.4	146.9	151.8
\angle_{O-Si-O_s}	103.3	104.1	105.5	105.1	106.1	104.4
\angle_{O-Si-O_i}	114.2	116.6	113.2	117.5	113.2	118.4
Symmetry	$C2/c$	$C2/c$	$C2/c$	$C2/c$	$C2/c$	$C2/c$

Furthermore, if zsm-11 and zsm-12 would really contain those deviating distances and angles, then one would expect that only the JC potential, which is derived from structural data on α -quartz, would disagree with experiment. However, *both* the JC and the almost *ab initio* BJS II potential predict virtually the same structures. In the latter structures only the above mentioned angles and distances differ from experiment. Furthermore, we have shown that the BJS II and JC potential give very accurate predictions for well-defined structures like α -quartz, cubic faujasite, and monoclinic zsm-5, which have been determined from single-crystal measurements. Thus, the BJS II and JC predictions indicate that the measured O-Si-O angles and Si-O distances in zsm-11 and zsm-12 might not be accurate. We conclude that the BJS II and JC potential are the most accurate on structure predictions for all-silicate polymorphs with a density lower or equal to that of α -quartz.

5.3.2 Hypothetical all-silica structures

In Table 5.3 we compare predictions for the hypothetical all-silica structures with experimental data on the alumina containing materials. Both the BJS II and JC potential predict for chabazite and hexagonal faujasite smaller unit cells than indicated by experiment.

Table 5.3. Predictions for hypothetical all-silica structures compared with experimental original structures. Symbols and units are the same as in Table 5.2. Hexagonal faujasite is abbreviated as hexagonal faujasite, thomsonite as THO and chabazite as CHA. References denote experiment.

	Expt.	BJS I	BJS II	KFBS	JC	TTA
EMT [30]						
<i>a</i>	17.42	16.89	17.05	17.53	17.13	17.95
<i>c</i>	28.42	27.53	27.83	28.62	27.98	29.31
γ	120.0	120.00	120.0	120.0	120.0	120.0
d_{Si-O_s}	1.630	1.607	1.591	1.600	1.599	1.635
d_{Si-O_i}	1.631	1.621	1.616	1.621	1.615	1.659
$\langle d_{Si-O} \rangle$	1.631	1.616	1.604	1.609	1.607	1.646
$\angle_{Si-O-Si_s}$	141.5	133.3	135.5	143.3	137.5	143.9
$\angle_{Si-O-Si_i}$	145.8	140.3	150.4	161.0	149.4	162.0
$\langle \angle_{Si-O-Si} \rangle$	142.9	136.5	142.8	152.9	143.47	153.8
\angle_{O-Si-O_s}	109.4	102.3	106.1	104.7	107.2	104.4
\angle_{O-Si-O_i}	109.5	114.4	112.5	116.2	112.0	116.9
Symmetry	<i>P6₃/mmc</i>	<i>P6₃/mmc</i>	<i>P6₃/mmc</i>	<i>P6₃/mmc</i>	<i>P6₃/mmc</i>	<i>P6₃/mmc</i>
THO [26]						
<i>a</i>	13.23 (13.85)	13.52	13.65	13.98	13.75	14.32
<i>b</i>	13.08 (6.92)	6.762	6.827	6.99	6.876	7.161
<i>c</i>	13.05 (6.43)	6.224	6.315	6.47	6.357	6.625
α	90.00 (90.00)	90.0	90.0	90.0	90.0	90.0
d_{Si-O_s}	1.614 (1.569)	1.565	1.562	1.585	1.578	1.619
d_{Si-O_i}	1.755 (1.632)	1.629	1.617	1.620	1.615	1.659
$\langle d_{Si-O} \rangle$	1.681 (1.614)	1.613	1.602	1.609	1.605	1.646
$\angle_{Si-O-Si_s}$	126.9 (142.0)	131.7	138.3	148.2	140.46	148.9
$\angle_{Si-O-Si_i}$	140.9 (180.0)	180.0	180.0	180.0	179.99	180.0
$\langle \angle_{Si-O-Si} \rangle$	135.5 (150.8)	142.0	147.9	155.6	149.4	156.2
\angle_{O-Si-O_s}	101.5 (108.0)	106.2	107.4	103.1	108.1	102.6
\angle_{O-Si-O_i}	113.7 (111.1)	116.2	113.8	113.6	112.2	113.9
Symmetry	<i>Pncn (Pmma)</i>	<i>P2/c</i>	<i>Pmma</i>	<i>Pmma</i>	<i>Pmma</i>	<i>Pmma</i>
CHA [27]						
<i>a</i>	9.441	9.102	9.144	9.398	9.198	9.620
α	93.09	94.77	94.66	94.91	94.75	94.95
d_{Si-O_s}	1.616	1.601	1.593	1.599	1.599	1.635
d_{Si-O_i}	1.683	1.609	1.603	1.619	1.607	1.657
$\langle d_{Si-O} \rangle$	1.642	1.605	1.599	1.609	1.603	1.645
$\angle_{Si-O-Si_s}$	140.35	140.0	142.2	153.7	144.2	154.5
$\angle_{Si-O-Si_i}$	157.66	144.4	147.3	155.7	148.7	156.5
$\langle \angle_{Si-O-Si} \rangle$	148.1	142.6	145.7	154.9	147.0	155.4
\angle_{O-Si-O_s}	98.57	104.1	106.7	105.1	107.6	104.7
\angle_{O-Si-O_i}	113.3	114.0	112.4	114.7	111.7	115.2
Symmetry	<i>R$\bar{3}m$</i>	<i>R$\bar{3}m$</i>	<i>R$\bar{3}m$</i>	<i>R$\bar{3}m$</i>	<i>R$\bar{3}m$</i>	<i>R$\bar{3}m$</i>

(Continued on next page.)

This is mainly due to the T-O distances in the calculated all-silica structures, which are substantially smaller than the experimental distances in the alumina containing materials. Experimentally [45] it is also found that that T-O distances are smaller in all-silica polymorphs than in the alumina containing analogues. (We use T instead of Si when in the experiment Si might have been replaced by Al or another atom). The KFBS and TTA calculated hypothetical structures possess smaller T-O distances and larger T-O-T angles than the experimental alumina containing materials. This seems an artifact of the potentials instead of an Al/Si substitution effect, because the KFBS and TTA potential also overestimate the Si-O-Si bond angle in all-silica structures. (See Table 5.2.) Thomsonite (Si/Al 1:1) shows a spectacular effect when Al is replaced by Si. All potentials predict a decrease of the T-O distances and a large increase of the T-O-T angles in this structure. The largest T-O-T angle in this structure becomes 180° , causing a change of symmetry. Due to this symmetry change, the unit cell almost halves. We notice that JC and BJS II predictions for the all-silica thomsonite structure are close to the structure proposed by Genechten *et al.* [26]. (Genechten data are in parentheses.) Table 5.4 presents predictions for the all-silica form of lovdarite which are compared with experimental data on the Be containing material. Predictions for the all-silica form of vpi-7 are compared with experimental data on the Zn containing sample. Although KFBS calculations of the all-silica forms of lovdarite and vpi-7 have been reported before [40], we could not obtain satisfactory KFBS and TTA results for these structures. The calculated structures did not converge or had imaginary frequencies. We obtained many local minima structures in our calculations. Some of the structures obtained showed anomalous angles and distances and all symmetry was lost.

Table 5.4. Predictions for hypothetical all-silica structures compared with experimental original structures. Symbols and units are the same as in Table 5.2.

Property	Expt.	BJS I	BJS II	JC
lovdarite [28]				
a	39.58	40.0	41.13	41.13
b	6.931	6.979	7.076	7.107
c	7.152	6.995	7.076	7.115
α	90.0	90.0	90.0	90.0
d_{Si-O_s}	1.560	1.596	1.581	1.630
d_{Si-O_t}	1.699	1.643	1.639	1.594
$\langle d_{Si-O} \rangle$	1.622	1.618	1.607	1.608
$\angle_{Si-O-Si_s}$	122.1	124.6	128.1	140.0
$\angle_{Si-O-Si_t}$	162.9	148.2	166.3	159.8
$\langle \angle_{Si-O-Si} \rangle$	137.5	135.9	142.9	143.4
\angle_{O-Si-O_s}	102.5	103.4	107.3	107.6
\angle_{O-Si-O_t}	116.6	115.2	114.5	112.4
Symmetry	$Pma2$	$Pma2$	$P4_2/mmc$	$Pma2$

(Continued on next page.)

Table 5.4. Continued.

Property	Expt.	BJS I	BJS II	JC
vpi-7 [29]				
<i>a</i>	40.62	39.79	41.12	40.98
<i>b</i>	7.179	6.945	7.053	7.079
<i>c</i>	7.179	6.945	7.053	7.079
α	90.0	89.7	90.0	89.9
d_{Si-O_s}	1.569	1.592	1.581	1.593
d_{Si-O_i}	1.657	1.642	1.636	1.630
$\langle d_{Si-O} \rangle$	1.605	1.620	1.607	1.610
$\angle_{Si-O-Si_s}$	132.8	124.9	128.0	131.0
$\angle_{Si-O-Si_i}$	170.8	148.3	163.7	153.8
$\langle \angle_{Si-O-Si} \rangle$	145.6	135.0	142.4	142.4
\angle_{O-Si-O_s}	104.0	103.8	106.8	106.5
\angle_{O-Si-O_i}	115.7	116.0	114.4	113.5
Symmetry	$I\bar{4}m2$	$Fdd2$	$Fdd2$	$Fdd2$

This indicates that either vpi-7 and lovdarite can not exist in the pure-silica form or that the potentials can not cope with these structures. We think the latter is the case because the starting structure used in the calculations contains very narrow T-O-T angles. These angles could not be reproduced by both potentials. This must be due to that the TTA and KFBS potential predict Si-O-Si bond angles which are too stiff. (See Table 5.2.) For the KFBS potential this has also been discussed elsewhere [36]. The BJS II and JC potential predict for lovdarite and vpi-7 an all-silica structure with virtually unchanged T-O-T angles and again shortened T-O distances. Thus, except for thomsonite, the BJS II and JC predictions indicate that substitution of Al, Be, B or Zn by Si in the hypothetical structures causes a decrease of T-O distances and leaves the T-O-T angles, even the small ones, virtually unchanged. The predicted Al/Si substitution effect is in agreement with experimental findings [45].

5.3.3 Calculated energies versus experiment

Table 5.5 presents the calculated lattice energy relative to α -quartz of several all-silica polymorphs. This quantity is equal to the change in energy, denoted as ΔU_{trans} , for the process SiO_2 (α -quartz) \rightarrow SiO_2 (silica polymorph). The latter is compared with the experimental enthalpy change ΔH_{trans} , which equals ΔU_{trans} for solid state reactions, because the ΔpV -term is negligible for solids at ambient conditions. As we compare the calculated ΔU_{trans} at 0 K with the experimental ΔU_{trans} determined at 300 K, we neglect the effect of temperature on this energy. This effect can be neglected because free energy calculations on α -quartz, with several potential used, predict changes of the lattice energy that range from from 0.5 to 0.001 kJ/mol when temperature is increased from 0 to 300 K. Free energy minimizations are discussed elsewhere [41]. We do not expect this effect to be larger in other silicates because experiments [42,43] have shown that temperature-induced structural changes in other silicates are also small.

Table 5.5. The calculated ΔU_{trans} of all-silica polymorphs compared with data of Petrovic et al. [9] and Johnson et al. [44]. Silicates measured by Johnson et al. [44] are indicated by daggers. Monoclinic zsm-5 is abbreviated as zsm-5-m, cubic faujasite as FAU and hexagonal faujasite as EMT. ΔU_{trans} is in kJ/mole SiO_2 .

silicate	Expt.	BJS I	BJS II	KFBS	JC	TTA
zsm-11	8.2	5.54	1.83	42.56	10.91	38.26
zsm-12	8.7	3.59	0.96	32.41	8.04	30.32
zsm-5-m	8.2	4.78	1.93	37.00	9.55	33.79
ssz-24	7.2	4.37	2.04	36.48	10.68	33.94
EMT	10.5	6.97	7.08	64.48	19.94	59.16
FAU	13.6	6.79	6.95	64.34	19.71	59.24
α -cristobalite †	2.84	2.07	-1.50	16.36	3.39	16.56
coesite †	2.93	5.68	0.84	-13.83	2.05	-16.74
stishovite †	51.88	40.99	-48.40	-15.56	131.56	5.69

Only the JC and BJS I potential predict correctly that the dense silicates coesite and stishovite are more unstable than α -quartz. (See Table 5.5.) The BJS I potential gives a reasonable prediction of the structure and relative stability of stishovite, although the silicon is sixfold-coordinated in this material, while the parameters of this potential are derived from *ab initio* potential energy surfaces of fourfold-coordinated clusters [11]. (See Table 5.2.) This is not so surprising as it may seem at first sight, because in the calculations of those potential energy surfaces the Si-O bond length was stretched to 2.00 Å and the O-Si-O bond angle was lowered to 70°, well beyond the bond distances and angles in stishovite. The BJS II potential gives a worse prediction for both the structure and relative stability of stishovite. The less accurate BJS II prediction for the stishovite structure is mainly due to a substantial underestimation of the largest Si-O bond distances. (See Table 5.2.) As the remaining distances and angles are predicted reasonably, the underestimated Si-O distances might stabilize the predicted stishovite so much that it becomes more stable than α -quartz, which is not in agreement with experiment. Although the BJS II potential is derived from the same potential energy surfaces as the BJS I potential (see Sect. 5.2.3 and Ref. 11.) the less accurate BJS II prediction for stishovite might be due to the inclusion of structural data on α -quartz in the parametrization of this potential. Although the latter has improved the BJS II predictions for a large range of structures, this potential is not suitable to model stishovite. The JC predicted value for the ΔU_{trans} of stishovite is far too high. Some of the Si-O bond lengths in stishovite are overestimated by the JC potential while others are underestimated. (See Table 5.2.) Presumably, this has opposite effects on the predicted ΔU_{trans} . The large overestimation of the ΔU_{trans} might therefore be caused by the three-body bond angle term in the JC potential, which destabilizes O-Si-O angles deviating from the ideal tetrahedral value. Predictions of the KFBS and TTA potential for stishovite are discussed in literature [13]. We notice that the predictions of all three shell model potentials (BJS I, BJS II and JC) for ΔU_{trans} are substantially closer to the experimental values than those of the rigid-ion model potentials (TTA and KFBS). To account for these results we have decomposed the calculated ΔU_{trans} into covalent and electrostatic contributions.

5.3.4 Decomposition of the calculated ΔU_{trans}

Table 5.6 lists the silicates for which we have calculated the ΔU_{trans} .

Table 5.6. Predicted densities for the studied silicates. Densities are in number of T atoms per 1000 Å³. Orthorhombic zsm5 is abbreviated as zsm-5-o, for other abbreviations see Tables 5.2 and 5.3. Dashes denote structures that did not converge. References denote experiment.

silicate	BJS I	BJS II	KFBS	JC	TTA
EMT [30]	14.11	13.71	12.61	13.50	11.73
FAU [22]	14.11	13.71	12.61	13.51	11.74
zsm-18 [21]	15.55	15.05	13.91	14.82	12.95
chabazite [27]	16.09	15.86	14.63	15.59	13.64
thomsonite [26]	17.57	16.99	14.75	16.64	14.72
gismondine [26]	18.82	17.38	15.80	17.13	–
lovdarite [28]	18.42	17.48	–	17.31	–
vpi-7 [29]	18.77	17.60	–	17.53	–
sodalite [31]	19.37	17.86	22.81	17.85	15.43
mordenite [32]	19.22	17.98	17.14	17.87	15.73
ssz-24 [24]	19.49	18.03	17.81	18.02	16.70
zsm-11 [19]	19.33	18.11	16.69	18.05	15.57
zsm-5-o † [23]	19.70	18.24	16.93	18.27	15.76
zsm-5-m † [23]	19.54	18.31	16.93	18.05	15.76
laumontite [26]	19.37	18.51	18.27	18.27	–
brewsterite [32]	19.69	18.67	18.42	18.42	16.23
zsm-12 [20]	21.18	19.31	19.48	19.48	18.40
zsm-22 [25]	21.50	19.87	19.85	19.85	17.55
analcime [26]	20.57	20.23	19.90	19.90	18.21
α-cristobalite [43]	25.21	22.67	23.09	23.09	23.80
α-quartz [16]	29.44	27.54	27.70	27.70	24.79
coesite [17]	31.75	32.27	30.86	30.86	27.13
stishovite [18]	46.17	46.67	44.47	44.47	40.03

† The TTA and KFBS potential predict orthorhombic zsm-5 as the most stable form, when both the orthorhombic and monoclinic structure are used as a starting structure.

The ΔU_{trans} predicted by the rigid-ion model potentials is decomposed into a term ΔU_{trans}^{cov} that is a sum over all covalent interactions, and a term ΔU_{trans}^{els} , which is a sum over all electrostatic interactions of the point charges. The KFBS and TTA results of this decomposition are shown in Fig. 5.1. Shell model predictions for ΔU_{trans} are decomposed into a covalent term ΔU_{trans}^{cov} , acting on the shells, without the intra-core-shell harmonic interaction, and an electrostatic term ΔU_{trans}^{cov} due to the atomic charges and the polarization. The latter terms includes the harmonic intra-core-shell interaction. Shell model results are shown in Fig 5.2.

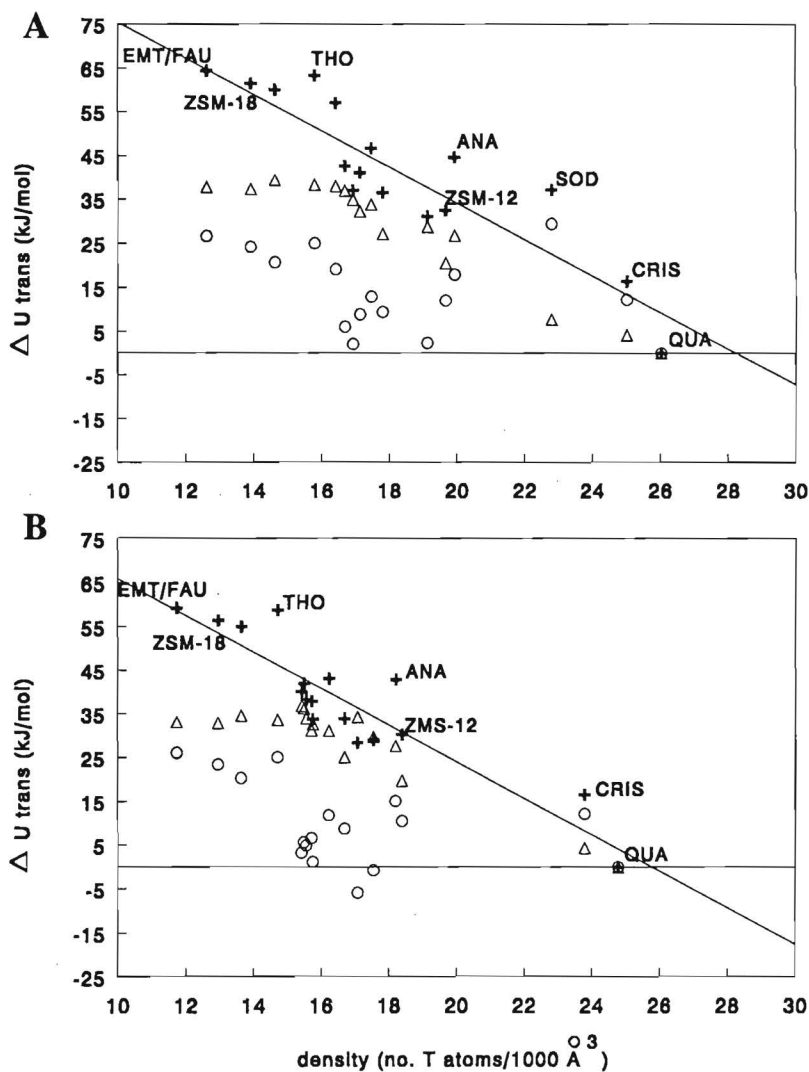


Figure 5.1. Decomposition of predicted values for ΔU_{trans} into ΔU_{trans}^{els} and ΔU_{trans}^{cov} for the silicates in Table 5.5. Crosses depict ΔU_{trans} . Open circles depict ΔU_{trans}^{cov} and open triangles ΔU_{trans}^{els} . A: KFBS prediction. B: TTA prediction. Lines represent linear fit on ΔU_{trans} versus the density.

Both rigid-ion models predict a positive ΔU_{trans}^{cov} and ΔU_{trans}^{els} . The ΔU_{trans}^{els} calculated with both rigid-ion model potentials varies much more than the ΔU_{trans}^{cov} . Thus the variation of the ΔU_{trans} is mostly caused by that of the ΔU_{trans}^{els} . We did not apply the energy correction of Kramer *et al.* [5] on the KFBS predictions. This correction was applied to the energy after the structure was optimized. As this makes the structure and the energy predictions inconsistent their conclusions seem hard to justify.

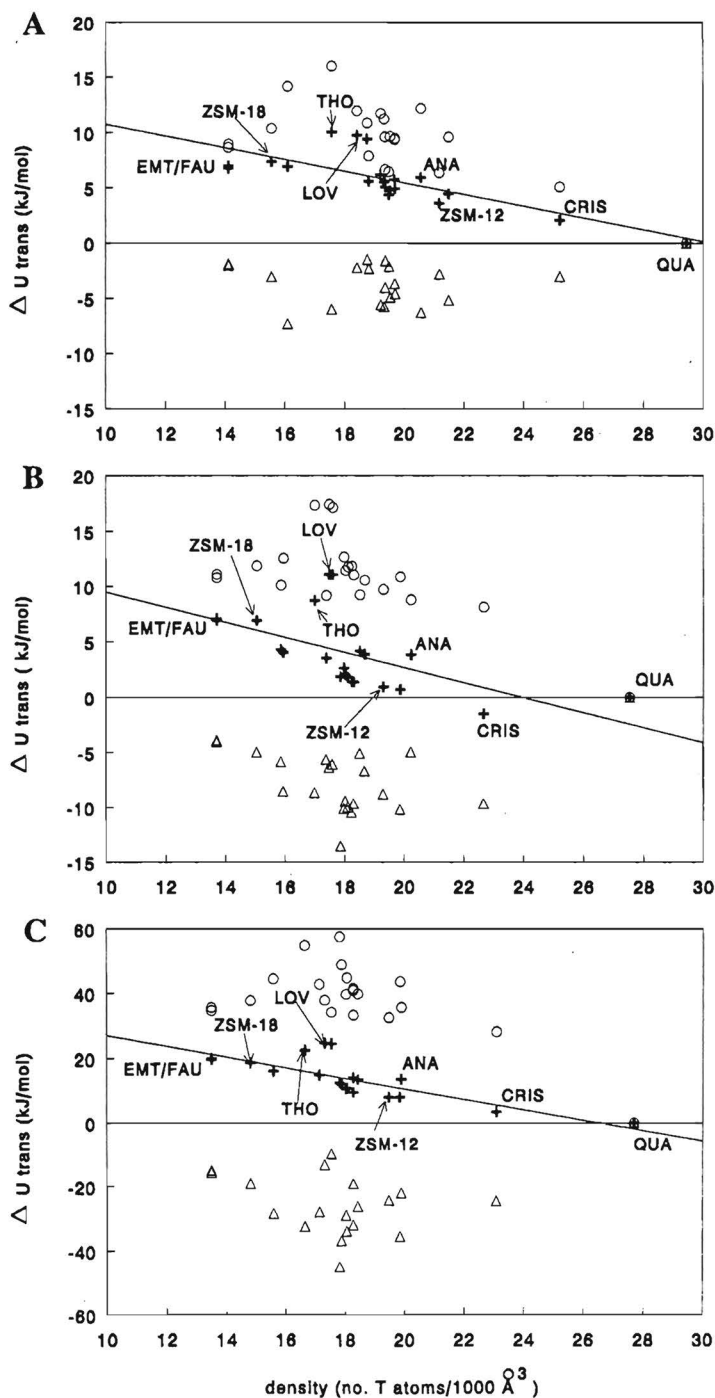


Figure 5.2. Decomposition of predicted values for ΔU_{trans} into ΔU_{trans}^{els} and ΔU_{trans}^{cov} for the silicates in Table 5.5. Crosses depict ΔU_{trans} . Open circles depict ΔU_{trans}^{els} and open triangles ΔU_{trans}^{cov} . A: BJS I prediction. B: BJS II prediction. C: JC prediction. Lines represent linear fits on ΔU_{trans} versus the density.

The shell model potentials predict that ΔU_{trans}^{cov} and ΔU_{trans}^{els} have opposite sign. (See Fig. 5.2.) The partial canceling of ΔU_{trans}^{cov} and ΔU_{trans}^{els} favors a less varying and smaller ΔU_{trans} than in the rigid-ion model predictions. The energy predictions of all three shell models give pictures that are similar, although the parameters of these potentials are quite different. The same applies to the two rigid-ion model potentials. These results indicate that a good prediction of relative stabilities is not due to the use of a specific parameter set, as suggested in literature [5], but might be caused by the use of a shell model potential.

Thus, we have shown that the KFBS and TTA potential do not give accurate predictions for both the structure and ΔU_{trans} of silicates. The BJS I potential predicts the ΔU_{trans} of silicates reasonably but gives less accurate predictions for the structure of those materials. Both the JC and BJS II potentials give accurate structure predictions for a large range of silicates. The JC potential also gives accurate prediction for the ΔU_{trans} of the silicates studied. Because the JC and BJS II potential give the most accurate prediction for the structure of silicates, we used them to investigate structure-stability relationships that have been proposed in literature.

5.3.5 Correlation between ΔU_{trans} and the density

The existence of a correlation between the density and the ΔU_{trans} of silicates is subject to debate: Henson *et al.* [8] conclude on basis of calculations with the JC potential that there is a linear relation between ΔU_{trans} and the density. The latter was also concluded by de Vos *et al.* on basis of their force field results [15]. Kramer *et al.* concluded that the strong correlation between the calculated ΔU_{trans} and the density is due to an artifact in the C/r^6 term of the KFBS potential (see above) [5]. Johnson *et al.* measured enthalpies for seven silicates. Those data suggested a linear relation between ΔU_{trans} and the density of silicates [44]. Recently Petrovic *et al.* [9] measured the ΔH_{trans} for six silica polymorphs. Those data show at most, a weak correlation between the density and ΔU_{trans} of all-silica polymorphs. Figure 5.3 shows experimental values for the ΔU_{trans} and the density, together with BJS II and JC results for the all-silica polymorphs listed in Table 5.5. The linear fits in Fig. 5.3 show that both potentials do not predict a real correlation between ΔU_{trans} and the density if a large number of structures is considered. This is consistent with the recent results of Petrovic *et al.* [9]. We therefore conclude that a linear relation between ΔU_{trans} and the density is not likely to hold for a large number of all-silica polymorphs.

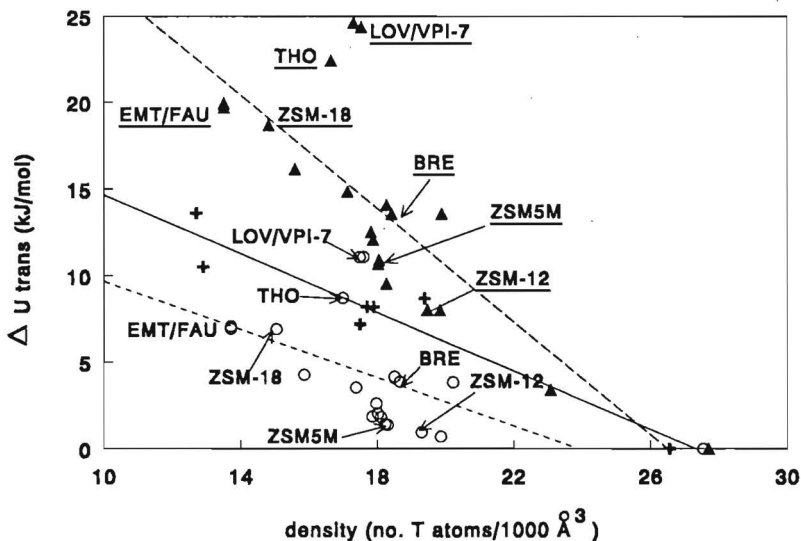


Figure 5.3. JC and BJS II predictions for ΔU_{trans} versus the density of the silicates in Table 5.5, compared with experiment. Closed triangles and underlined abbreviations depict JC predictions. Open circles and remaining abbreviations depict BJS II predictions. Crosses depict data of Petrovic *et al.*, (See Table 5.4.) The abbreviations depict silicates containing Si-O-Si bond angles smaller than or equal to 140° . The lower line represents a linear fit on BJS II predictions, rms error of this fit is 2.75 kJ/mol. The middle line represents a linear fit on data of Petrovic *et al.*, rms error of this fit is 1.20 kJ/mol. The upper line represents a linear fit on JC predictions, rms error of this fit is 3.95 kJ/mol. Monoclinic zsm-5 is abbreviated as zsm5m.

5.3.6 Correlation between small Si-O-Si bond angles and ΔU_{trans}

Petrovic *et al.* [9] proposed on basis of enthalpy measurements for six silicates that there should exist a linear relationship between ΔU_{trans} and the percentage of Si-O-Si bond angles smaller than or equal to 140° in the structure. To investigate this more thoroughly we have evaluated BJS II and JC predictions for more silicates with narrow Si-O-Si bond angles. Plots of JC and BJS II predictions for ΔU_{trans} versus the above mentioned percentage are shown in Fig. 5.4. The lines represent linear fits. Both potentials predict that the linear relationship proposed by Petrovic *et al.* is not expected to hold when a large number of structures is considered.

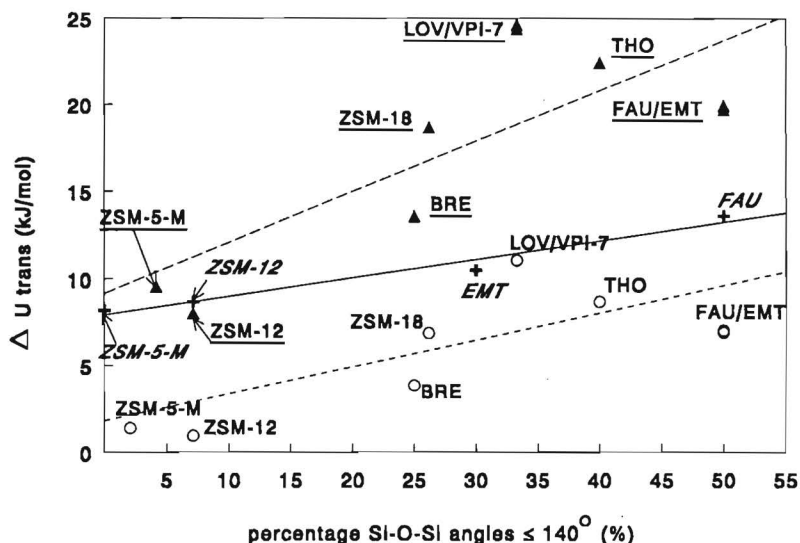


Figure 5.4. BJS II and JC predictions for ΔU_{trans} versus the percentage of angles smaller than or equal to 140° in the structures of Table 5.5. which contain small angles. These values are compared with experimental values of the structures mentioned in Table 5.4 which contain small angles. Abbreviations in slanted type depict experiment, remaining abbreviations are as in Fig. 5.3. The lower line represents a linear fit on BJS II predictions, rms error of this fit is 2.63 kJ/mol. The middle line represents a linear fit on experimental values, rms error of this fit is 0.38 kJ/mol. The upper line represents a linear fit on JC predictions, r.m.s error of this fit is 3.82 kJ/mol.

5.3.7 Relation between structure and ΔU_{trans} for low-density silicates

Petrovic *et al.* have hypothesised that pure-silica materials with large pores (i.e. materials with a low density) are not destabilized by their large cages but by the presence of small Si-O-Si bond angles in the structure. This is then the reason why they are so difficult to synthesize [9]. This hypothesis is based on enthalpies of three low-density silicates. To test this hypothesis, we have considered BJS II and JC predictions for a larger number of low-density silicates. The BJS II and JC predictions on hexagonal faujasite, cubic faujasite, zsm-18, vpi-7, lovdarite and thomsonite, materials that have a relative low density, show that these structures are less stable than the other structures. (See Figs. 5.3 and 5.4.) The former structures contain a significant percentage of angles smaller than or equal to 140° . (See Fig. 5.3.) These structures contain, except the small Si-O-Si bond angles, no *other* anomalous angles and distances, which might be responsible for instability. (See Tables 2 and 3.) Thus, the instability of those structures must be caused by small Si-O-Si bond angles, which supports the hypothesis of Petrovic *et al.* [9]. We note in passing that this hypothesis also explains why cubic faujasite is more unstable than zsm-18, something which could not be explained by the presence of 3-rings in the structure [3,40,45]. Furthermore, we expect that this hypothesis does not hold for higher-density zeolites because higher-density silicates with a significant percentage of Si-O-Si bond angles smaller than or equal

to 140°, are not necessary less stable than other systems. (See Figs. 5.3 and 5.4.)

5.4 Conclusions

Our main result is that we have derived a new *ab initio* based shell model potential (BJS II) which is equally accurate as the JC potential on structure predictions. Inclusion of structure data on α -quartz in the BJS II potential improved all structure predictions studied. The predictions of the JC and BJS II potentials for well-defined structures are much closer to the experiment than those of the BJS I, TTA and KFBS potential. The BJS II and JC results further indicate that the experimentally determined Si-O distances and O-Si-O angles in zsm-11 and zsm-12 may not be accurate. The fact that the BJS II and the JC potential have been derived in completely different manners (*ab initio* versus semi-empirical), and yet yield such similar results for structures, implies that these potentials should be very reliable on structure predictions. The accurate structure predictions of the JC potential combined with reasonable stability predictions, makes this potential suitable for the exploration of hypothetical structures and the study of structure-stability relationships. To a lesser extent this also holds for the BJS II potential. This potential gives accurate structure predictions, but less accurate predictions for the relative stability of silicates. The structure-stability relationships can not be studied with the KFBS and TTA potential, because those potentials predict the structure and relative stability of silicates less accurately.

Furthermore, the higher accuracy of the BJS I, BJS II and JC stability predictions, compared to those of the KFBS and TTA potential indicates that a shell model might be mandatory for a good prediction of the stability. With respect to the structure-stability relationships we conclude the following: *Both* the JC and BJS II potential predict that there exists no linear relation between ΔU_{trans} and the density of silicates. Those potentials consistently predict that low-density silicates are destabilized by their narrow Si-O-Si bond angles. This supports the hypothesis of Petrovic *et al.* [9] that pure-silica large-pore (i.e., low-density) materials are destabilized by small Si-O-Si bond angles in the structure. This makes them more difficult to synthesize than materials containing Be, B and Zn, because the presence of the latter elements favors smaller T-O-T bond angles [9]. We have shown that the T-O distances in the latter structures are substantially larger than in the all-silica structures. These large T-O distances favor smaller T-O-T angles. The JC and BJS II results indicate that the linear relation between ΔU_{trans} and the percentage of angles smaller than or equal to 140°, as proposed by Petrovic *et al.* [9], is not likely to exist for a large number of silicates.

5.5 References

- [1] *Solid State Chemistry*, Editors A.K. Cheetham and P. Day, University Press Oxford, 1990 Vol 2; Compounds.
- [2] P.A. Jacobs and J.A. Martens, *Synthesis of High Silica Alumino Silicate Zeolites*, Elsevier, Amsterdam, 1987.
- [3] R.A. van Santen, G. Ooms, J.J. den Ouden, B.W.H. van Beest and M.F.M. post, ACS Symp. Series **398**, 617 (1989).
- [4] R.A. van Santen, B.W.H. van Beest and A.J.M. de Man, *Guidelines for Mastering the Properties of Molecular Sieves*, Editors D. Bartomeuf *et al.*, Plenum Press, New York, 1990.
- [5] G.J. Kramer, A.J.M. de Man and R.A. van Santen, J. Am. Chem. Soc. **113**, 6435 (1991).
- [6] J.B. Nicolas, A.J. Hopfinger, F.R. Trouw and L.E. Iton, J. Am. Chem. Soc. **113**, 4792 (1991).
- [7] R.A. Jackson and C.R.A. Catlow, Mol. Simul. **1**, 207 (1988).
- [8] N.J. Henson, A.K. Cheetham and J.D. Gale, Chem. Mater. **6**, 1647 (1994).
- [9] I. Petrovic, A. Navrotsky M.E. Davis and S.I. Zones, Chem. Mater. **5**, 1805 (1993).
- [10] A.J.M. de Man, H.K. Küppers and R.A. van Santen, J. Phys. Chem. **96**, 2092 (1992).
- [11] K. de Boer, A.P.J. Jansen and R.A. van Santen, Chem. Phys. Lett. **223**, 46 (1994), *Chapter 2 of this thesis*.
- [12] K. de Boer, A.P.J. Jansen, R.A. van Santen, *Chapter 4 of this thesis*.
- [13] G.J. Kramer, N.P. Farragher, B.W.H. van Beest and R.A. van Santen, Phys. Rev. B **43**, 5068 (1991).
- [14] S. Tsuneyuki, M. Tsukada, H. Aoki and Y. Matsui, Phys. Rev. Lett. **61**, 869 (1988).
- [15] E. de Vos Burchard, V.A. Verheij, H. van Bekkum and B. van de Graaf, Zeolites **12**, 183 (1992).
- [16] G.A. Lager, J.D. Jorgensen and F.J. Rotella, J. Appl. Phys. **53** (10), 6751 (1982).
- [17] K.L. Geisinger, M.A. Spackman and G.V. Gibbs, J. Phys. Chem. **91** (1987) 3237.
- [18] W. Sinclair and A.E. Ringwood, Nature **272**, 714 (1978).
- [19] C.A. Fyfe, H. Gies, G.T. Kokotailo, C. Pasztor, H. Strobl and D.E. Cox, J. Am. Chem. Soc. **111**, 2470 (1989).
- [20] C.A. Fyfe, H. Gies, G.T. Kokotailo, B. Marler and D.E. Cox, J. Phys. Chem. **94**, 3718 (1990).
- [21] S.L. Lawton and W.J. Rohrbaugh, Science **247**, 1319 (1990).
- [22] J.A. Hriljac, M.M. Eddy, A.K. Cheetham, J.A. Donahue and G.J. Ray, J. Solid State Chem. **106**, 66 (1993).
- [23] H. van Koningsveld, J.C. Jansen and H. van Bekkum, Zeolites **10**, 235 (1990).
- [24] R. Bialek, W.M. Meier, M.E. Davis and M.J. Annen, Zeolites **111**, 438 (1991).
- [25] B. Marler, Zeolites **7**, 393 (1987).
- [26] K.A. van Genechten and W.J. Mortier, Zeolites **8**, 273 (1988).
- [27] J.V. Smith, F. Rinaldi and L.S. Dent Glasser, Acta Cryst. **16**, 45 (1963).
- [28] S. Merlino, Europ. J. Miner **2**, 809 (1990).
- [29] M.J. Annen, M.E. Davis, J.B. Higgins and J.L. Schlenker, J. Chem. Soc., Chem. Commun. 1175 (1991).
- [30] J.M. Newsam, M.M. Treacy, D.E.W. Vaughan, K.G. Strohmaier and W.J. Mortier, J. Chem. Soc., Chem. Commun. 493 (1989).
- [31] I. Hassan and H.D. Grundy, Acta Cryst. B **40**, 6 (1984).
- [32] A. Alberti, Proc. 7th Int. Zeolite. Conf., Tokyo, 437 (1986).

- [33] C.R.A. Catlow and W.C. Mackrodt, *Computer simulations in physics, lecture notes in physics* (Springer, Vienna 1982); C.R.A. Catlow, M. Doverty, G.D. Price, M.J. Sanders and S.C. Parker, *Mater. Sci. Forum* **7**, 163 (1986); author of THBREL: M. Leslie, Science and Engineering Research Council, Daresbury Laboratory, U.K.
- [34] C.R.A. Catlow and M.J. Norgett, Lattice Structure and Stability of Ionic Materials, private communication.
- [35] G. Dolling, *Calculations of phonon frequencies in Methods in computational physics vol. 15* (Academic Press, New York 1976); author of THBPHON: M. Leslie, Science and Engineering Research Council, Daresbury Laboratory, U.K.
- [36] K. de Boer, A.P.J. Jansen, R.A. van Santen, S.C. Parker and G.W. Watson, *Phys. Rev. B in press, Chapter 3 of this thesis.*
- [37] A.J.M. de Man, W.P.J.H. Jacobs, J.P. Gilson and R.A. van Santen, *Zeolites* **12**, 826 (1992).
- [38] A. Kirfel, G. Will and J. Arndt, *Z. Kristallogr.* **149** 315 (1979).
- [45] J.D. Gale, C.R.A. Catlow and W.C. Mackrodt, *Modelling Simul. Mater. Sci. Eng.* **1**, 73 (1992).
- [40] A.J.M. de Man, S. Ueda, M.J. Annen, M.E. Davis and R.A. van Santen, *Zeolites* **12**, 789 (1992).
- [41] S.C. Parker and G.D. Price, *Advances in Solid-Sate Chem.* **1**, 295 (1989).
- [42] K. Kihara, *Europ. J. Mineral.* **2**, 63 (1990).
- [43] J.J. Pluth, J.V. Smit and J. Faber Jr., *J. Appl. Phys.* **57**, 1045 (1985).
- [44] G.K. Johnson, I.R. Tasker and D.A. Howell, *J. Chem. Thermodynamics* **19**, 617 (1987).
- [45] J.D. Gale and A.K. Cheetham, *Zeolites* **12**, 674 (1992).

Chapter 6

The structure and elasticity of dodecasil-3C at variable temperatures

Abstract

Using free energy minimizations and three interatomic potentials, we calculated the structure of dodecasil-3C without guest molecules at several temperatures. For this structure, the interatomic potentials predict substantially different free energies relative to α -quartz. We find that dodecasil-3C without guest molecules is triclinic for temperatures between 0 to 1200 K. The positions of the O atoms in the experimental structure of calcined dodecasil-3C may not be well-resolved. Furthermore, we present predictions for the elastic constants C_{11} , C_{12} , and C_{44} that are in reasonable agreement with experiment on material with guest molecules. As we find that the symmetry of dodecasil-3C is lower than cubic which was reported at the time of the elasticity measurements, it might be interesting to perform additional measurements on this compound and to compare them with our predictions.

6.1 Introduction

In 1982 Gies *et al.* [1] introduced a new class of all-silica structures, the so-called clathrasils, which are iso-structural to clathrate gas-hydrates. Those frameworks have been extensively studied since then [2–7]. In all these structures, corner-connected tetrahedra form cages, large enough to occlude organic molecules during synthesis. One of these compounds is dodecasil-3C. This clathrasil is characterized by two types of cages: a dodecahedron build from twelve 5-rings ($[5^{12}]$) and a larger one, consisting of twelve 5-rings and four 6-rings ($[5^{12}6^4]$). A simplified picture of dodecasil-3C, showing only straight lines between adjacent Si atoms, is given in Fig. 6.1.

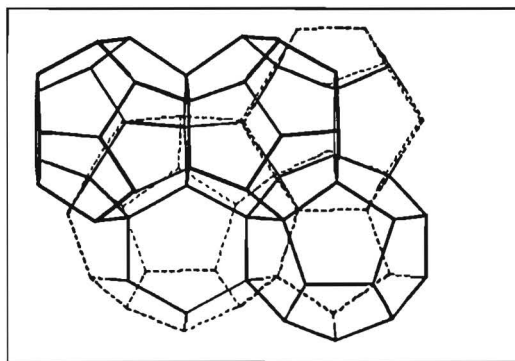


Figure 6.1. Simplified picture of dodecasil-3C, showing only straight lines between adjacent Si atoms.

The $[5^{12}]$ cage can contain smaller molecules such as N_2 , CH_4 or CO_2 [2–7]. The larger $[5^{12}6^4]$ cage, can occlude molecules such as pyridine, adamantylamine or trimethylamine [2–7]. Many different phases, dependent on temperature and the trapped guest molecules, have been reported for dodecasil-3C [7]. The relative stability of those phases and their transition temperatures are strongly dependent on the guest molecules enclathrated [7]. The structure of as-synthesized dodecasil-3C at low temperatures has not been resolved completely [7]. The X-ray powder diffraction experiments of Gunawardana *et al.* [8] indicate that the symmetry of dodecasil-3C, with guest molecules enclathrated, is maintained when the sample is calcinated, i.e. when the guest molecules are removed by heating the sample. According to the ^{29}Si NMR measurements of Groenen *et al.* [9], the structure of dodecasil-3C changes slightly on calcination. This is understandable because dodecasil-3C is stable up to 1200 K, far beyond the temperature that causes breakdown of the guest molecules [8]. Recently, Könnecke *et al.* [10] reported that the structure of calcined dodecasil-3C at $T \approx 523$ K has space group $Fd\bar{3}m$. These authors concluded that $Fd\bar{3}m$ was merely the space group for the averaged structure, which they attributed to static disorder of the O atoms in the lattice. The lower local symmetry of calcined dodecasil-3C could not be determined because DLS simulations in subgroups of $Fd\bar{3}m$ failed, or could not explain the observed disorder [10]. The X-ray diffraction and ^{29}Si NMR results of Tse *et al.* [11], indicate that calcined dodecasil-3C remains a single phase between 80 and

400 K. Könnecke *et al.* reported that this compound undergoes a small displacive phase transition at $T = 451$ K, which was detected using differential scanning calorimetry. We are not aware of other authors that report phase transitions of calcined dodecasil-3C. Furthermore, ^{29}Si NMR spectra that were reported [9,12] for dodecasil-3C after calcination at various temperatures above 400 K are similar, indicating that the empty structure changes only slightly with temperature.

Therefore, we have done a theoretical study, using free energy minimizations, to determine the local symmetry of dodecasil-3C without guest molecules at variable temperatures and to investigate temperature-induced phase transitions of this material. This work extends a previous study on dodecasil-3C that was based on calculations at $T = 0$ K [13]. Our free energy calculations require the use of interatomic potentials. Calculations are done with two shell model potentials and a rigid-ion model potential. According to the shell model predictions, dodecasil-3C without guest molecules is triclinic for temperatures ranging from 0 to 1200 K. The rigid-ion model predictions, indicating a different structure, will be shown to be less reliable than the shell model. Our calculations also indicate that the experimentally determined positions of the O atoms in calcined dodecasil-3C may be not well-resolved. Furthermore, we will compare predicted elastic constants of empty dodecasil-3C with experiment. One of the shell model potentials used predicts values for C_{11} , C_{12} and C_{44} that are in reasonable agreement with experiment. Experimental values for other elastic constants were not determined because when those experiments were performed, dodecasil-3C was reported to be cubic [14]. As our calculations indicate that the symmetry of calcined dodecasil-3C is lower than cubic, we conclude that it might be interesting to perform additional elasticity measurements on this material and to compare them with our predictions.

6.2 Method and computational details

Free energy minimizations have been done with the code PARAPOCS [15] which can be used to calculate physical properties of solids at variable temperatures and pressures. To calculate thermodynamical properties, the vibrational frequencies of the solid have to be computed. The calculations assume that vibrational motions in the solid are described by independent quantized harmonic oscillators the frequency of which varies with cell volume [16]. Minimization of the Gibbs free energy can be achieved by varying the cell volume and the positions of the ions until the configuration satisfies the following equilibrium conditions for a given temperature and pressure:

$$\frac{\partial F}{\partial V} = P_{app}. \quad (6.1)$$

$$\frac{\partial U_{stat}}{\partial \mathbf{r}} = \mathbf{0}. \quad (6.2)$$

In Eq. (6.1) F denotes the Helmholtz free energy, V the cell volume and P_{app} the applied pressure. In Eq. (6.2) U_{stat} denotes the static energy due to the interatomic interactions and \mathbf{r} denotes the atomic coordinates. Equation (6.1) states that the pressure exerted by the system (internal pressure) must equal the applied pressure. (Equation (6.1) is only

valid for cubic crystals. For more general cases the derivatives of the Helmholtz free energy with respect to the strain must be computed. Details can be found in Ref. 17.) Equation (6.2) states that the net force on each atom must vanish. After the Gibbs free energy is minimized, thermodynamical properties, elastic constants, dielectric constants and the structure of the solid can be computed. Calculation of the Helmholtz free energy and other thermodynamical properties requires computation of the vibrational frequencies for all wave vectors in the Brillouin-zone. This is done by computation of the frequencies on a three-dimensional grid within the Brillouin-zone. In our calculations we used the grid of Pavasi *et al.* [18] with each of the three coordinates k_n having values

$$k_n = \frac{3(2^{n-1}) - 2}{4(2^N - 1)}, \quad (6.3)$$

where N denotes the number of grid points in the reciprocal lattice and $n=1,2,\dots,N$. In our calculations we used the above grid with eight k -points ($N = 3$). This yields Gibbs free energies with an accuracy of 10^{-3} eV. The stability of the structures with minimal Gibbs free energy was tested by checking if all phonon frequencies were real on a grid in k -space of 125 grid points ($N = 5$). Furthermore, the calculations have been done on the structures without guest molecules. In our calculations we have employed the rigid-ion model potential derived by Kramer *et al.* [19] denoted as the KFBS potential. We have used the shell model potential of Catlow *et al.* [20] and the *ab initio* shell model potential derived by de Boer *et al.* [21]. Those potentials are referred to as the JC and BJS I potential, respectively. Cutoffs applied in calculations using the KFBS and JC potential are 10 Å [22]. The covalent O-O interactions of the BJS I potential are applied with a cutoff of 3.5 Å, because for larger distances all covalent potential terms are effectively zero. The covalent Si-O interaction of this potential is applied with a cutoff of 2.5 Å (i.e. in between the nearest and next nearest Si and O neighbors) to simulate a real Si-O bond. The electrostatic interactions are calculated using the Ewald summation.

6.3 Results

We will first discuss predictions for the relative stabilities of the dodecasil-3C structures. Subsequently, we will compare predicted elastic constants of the most stable structures with experiment. Finally, we will discuss the comparison between predicted structures and experiment.

6.3.1 Free energies of dodecasil-3C at variable temperatures

Several experimental structures are used as starting structures in the minimizations. We used the cubic $Fd\bar{3}$ structure that was proposed by Gies *et al.* [2] for dodecasil-3C at room temperature with Kr, Xe and $N(\text{CH}_3)_3$ as guest molecules. This structure will further on be denoted as D3C_c. We employed the tetragonal $I42d$ structure which was reported [23] for dodecasil-3C with pyridine as guest molecule at ambient conditions. This structure will be denoted as D3C_t. Finally, we used the orthorhombic structure with space group $Fddd$ that was proposed [24] for dodecasil-3C at low temperatures. This structure will further on

be referred to as $D3C_o$. We first performed $T = 0$ K minimizations on the above structures. For each potential used, both the $D3C_o$ and $D3C_c$ structure relaxed to essentially the same cubic structure with space group $Fd\bar{3}$. The cubic structures are saddle point structures as some of the frequencies, close to the Γ -point, are imaginary. When the tetragonal $D3C_t$ structure is minimized at $T = 0$ K both the BJS I and JC potential predict that this structure is a saddle point structure with space group $I\bar{4}2d$. Minimization with the KFBS potential of the $D3C_t$ structure at $T = 0$ K gives a tetragonal structure without change of symmetry. The latter structure corresponds to a true minimum structure, because there are no imaginary frequencies. The saddle point structures, obtained from the $T = 0$ K calculations, are used to calculate local minima structures, according to a well-known procedure [13]. Although many starting structures were used in this procedure, only a few local minima structures at $T = 0$ K were obtained. Those structures are listed in Table 6.1. To investigate whether those local minima might correspond to different phases of dodecasil-3C at elevated temperatures, we calculated the Gibbs free energy of those structures at several temperatures up to 1200 K. Dodecasil-3C is thermally stable below 1200 K [8]. Differences of the Gibbs free energies between the local minima structures are very small. Table 6.1 lists the Gibbs free energies in the temperature range for which phase transitions of as-synthesized dodecasil-3C have been reported [7]. The BJS I potential predicts that the most stable phase of dodecasil-3C is triclinic with space group $P\bar{1}$ in the temperature range 0 to 1200 K. Although the calculated Gibbs free energies of the local minima structures differ only slightly, the BJS I potential predicts no phase transitions in the studied temperature range.

Table 6.1. Predicted energies of the local minima structures at variable T . Free energy, denoted as $G(T)$, with T in K, is in eV. Internal energy, denoted as U is also in eV.

Symmetry	$U(0)$	$G(200)$	$G(300)$	$G(400)$	$G(500)$
BJS I					
$C2$	-2304.974	-2296.523	-2298.000	-2300.050	-
$P1$	-2304.989	-2296.538	-2298.013	-2300.054	-2302.591
$P\bar{1}$	-2305.138	-2296.654	-2298.127	-2300.157	-2302.681
KFBS					
$I4_1/a$	-1970.382	-1959.702	-1960.832	-1962.442	-1964.493
$I\bar{4}2d$	-1970.465	-1959.738	-1960.866	-1962.476	-1964.530
JC					
$P1$	-4372.280	-4363.322	-4364.703	-4366.633	-
$P\bar{1}$	-4372.353	-4363.345	-4364.703	-4366.606	-4368.994

The JC potential predicts that a triclinic structure with space group $P\bar{1}$ is the most stable for temperatures below 300 K. Above $T = 300$ K the triclinic $P1$ structure becomes more stable, indicating a phase transition at 300 K. (See Table 6.1.) This prediction might correspond to the small phase transition at $T = 451$ K, reported by Könnecke *et al.* [10].

As the structural changes associated with this transition have not been reported, we can not verify the JC prediction in more detail. For the $P1$ structure at $T = 410$ K, the JC potential predicts imaginary frequencies at several k -points which are not close to the Γ point. This indicates that the $P1$ structure becomes thermally unstable at $T = 410$ K. We emphasize that, although the JC-predicted $P\bar{1}$ structure is thermally stable for temperatures above 410 K, it is *metastable* with respect to the $P1$ structure for temperatures above 300 K. (See Table 6.1.) The JC-predicted $P1$ structure becomes thermally unstable at $T = 410$ K. Thus, the JC potential essentially predicts that the structure of dodecasil-3C is triclinic with space group $P1$ and that this structure becomes thermally unstable at $T = 410$ K. This temperature is too low when compared to the experimental value of 1200 K. The KFBS potential predicts that the tetragonal $I\bar{4}2d$ structure is the most stable in the range 0 to 1200 K. No phase transition is predicted. Thus, the KFBS-predicted structure differs substantially from the structure predicted by both other potentials. Predictions for the geometry of the most stable structures at 300 K are listed in Table 6.2.

Table 6.2. Predicted geometries of dodecasil-3C at $T = 300$ K. The symbol l refers to the largest distance or angle and s to the smallest distance or angle. Distances are in \AA and angles in degrees. As the JC potential predicts the $P\bar{1}$ and $P1$ structures with ΔG_{trans} values that are essentially equal at room temperature, we have listed them both.

Property	BJS I	KFBS	JC	JC
a	18.751	19.780	19.265	19.207
b	18.655	19.780	19.219	19.197
c	18.824	19.929	19.140	19.412
α	89.73	90.00	90.47	89.964
β	90.10	90.00	89.85	90.127
γ	89.34	90.00	89.95	89.974
ds_i-o_s	1.589	1.595	1.586	1.587
ds_i-o_l	1.623	1.616	1.609	1.608
$\langle ds_i-o \rangle$	1.606	1.606	1.599	1.597
$\angle_{si-o-si_s}$	131.6	159.6	143.7	140.8
$\angle_{si-o-si_l}$	155.5	177.1	166.4	175.6
$\langle \angle_{si-o-si} \rangle$	142.7	170.2	153.2	155.1
\angle_{o-si-o_s}	102.3	107.7	105.2	105.6
\angle_{o-si-o_l}	115.1	111.4	112.9	113.2
Symmetry	$P\bar{1}$	$I\bar{4}2d$	$P\bar{1}$	$P1$

To investigate which predictions are the most reliable, we calculated the Gibbs free energies relative to α -quartz of the most stable structures at variable temperatures. The results are illustrated in Fig. 6.2. The relative Gibbs free energy will further on be denoted as ΔG_{trans} . The BJS I and KFBS potentials predict correctly [25] that dodecasil-3C is metastable with respect to α -quartz for temperatures ranging from 0 to 800 K. The JC-predicted structure, that is thermally stable up to 400 K, is metastable with respect to α -quartz for temperatures ranging from 0 to 400 K. Dodecasil-3C must be metastable with respect to β -quartz for temperatures between 848 and 1200 K [26]. At 1200 K, dodecasil-3C

must be less stable than β -cristobalite [26]. The relative Gibbs energy with respect to the β -phases could not be calculated because all three potentials predict that those phases are not true minima structures at any temperature.

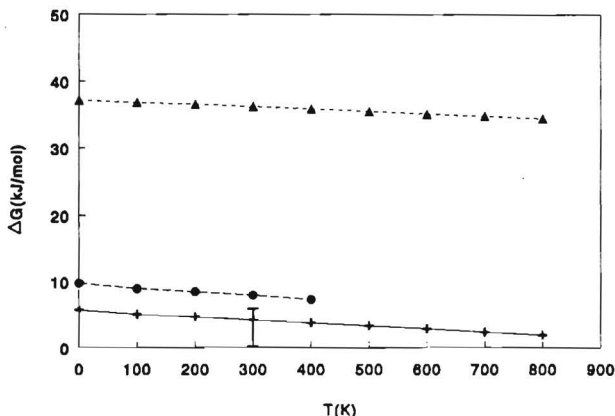


Figure 6.2. Predictions for ΔG_{trans} of dodecasil-3C at variable temperatures. Crosses: BJS I prediction. Closed triangles: KFBS prediction. Closed points: JC predictions. Vertical bar at 300 K indicates the range of experimental [27] ΔG_{trans} values for several all-silica frameworks in which the silicon is tetrahedrally coordinated.

The JC and BJS I potential predict similar values for the ΔG_{trans} of dodecasil-3C, whereas the KFBS-predicted values are substantially higher. (See Fig. 6.2.) We are not aware of experimental values of ΔG_{trans} for calcined dodecasil-3C. Experimental data [27] on other materials, ranging from the molecular sieve silicalite to the dense coesite, indicate that ΔG_{trans} values of all-silica frameworks with tetrahedrally coordinated silicons lie in a narrow range (vertical bar in Fig. 6.2.) The BJS I and JC predictions for the ΔG_{trans} of dodecasil-3C at room temperature are much closer to that range than those of the KFBS potential. Furthermore, the large differences between the KFBS-predicted values for ΔG_{trans} and those of the other potentials are mainly due to the predicted value of ΔG_{trans} at absolute zero. The ΔG_{trans} at 0 K is equal to the lattice energy relative to α -quartz because the ΔpV -term is negligible for solids at ambient pressure. We have shown in a previous study [32] that BJS I and JC-calculated values for the lattice energy relative to α -quartz of several all-silica polymorphs are much closer to experiment than those of the KFBS potential. The latter values are substantially different. This, as shown earlier [32], might be due to the fact that the KFBS potential is based on the rigid-ion model, in contrast to both other potentials. The above arguments indicate that JC and BJS I predictions for the stability of dodecasil-3C are more reliable than those of the KFBS potential. The JC potential is only able to model the thermal stability of dodecasil-3C up to 400 K. We conclude that BJS I and JC predictions for the stability of dodecasil-3C without guest molecules below 400 K are the most accurate. Above that temperature, we consider that of the BJS I potential as most reliable.

6.3.2 Predicted and experimental elastic constants of dodecasil-3C

In Table 6.3 we compare calculated elastic constants of the most stable structures at $T = 300$ K with experimental values, obtained by Küppers *et al.* [14]. (For the latter structures see Table 6.2.) The elastic constants were measured at ambient conditions for dodecasil-3C with guest molecules N_2 and Ar in the small and $N(CH_3)_3$ in the large framework cages. We are not aware of elasticity measurements on calcined dodecasil-3C.

Table 6.3. Predictions for elastic constants of dodecasil-3C at $T = 300$ K compared with experimental data of Küppers *et al.* [14]. Values not mentioned in the table are zero. Elastic constants are denoted as C_{ij} and are in $10^{10} Nm^{-1}$. Values in square brackets are elastic constants that have changed significantly due to increase of the cell volume with 1% as discussed in the text.

C_{ij}	Expt.	BJS I	KFBS	JC	JC
C_{11}	5.5	5.58 [6.41]	8.62 [9.01]	8.74	7.70
C_{22}	5.5	6.44	8.62 [9.01]	7.99	8.08
C_{33}	5.5	7.93	14.54	7.61	7.48 [6.84]
C_{44}	2.4	2.87	2.12	3.39	3.23
C_{55}	2.4	3.16	2.12	3.30	2.92
C_{66}	2.4	3.12	4.08	3.55	3.65
C_{12}	1.1	1.46 [1.19]	0.50 [0.77]	1.14	1.11
C_{13}	1.1	0.62	3.72	1.07 [1.00]	1.29 [1.59]
C_{14}		-0.07		-0.40	0.02
C_{15}		-0.83		0.13	0.18
C_{16}		0.03		0.03	0.19
C_{23}	1.1	0.63 [0.53]	3.72	1.35 [1.25]	1.79 [1.38]
C_{24}		0.43		-0.10	0.04
C_{25}		0.15		0.08	0.15
C_{26}		0.21		-0.25	-0.07
C_{34}		0.04		-0.23	0.14
C_{35}		0.00		0.28	0.17
C_{36}		0.43		0.00	0.05
C_{45}		0.02		0.02	0.15
C_{46}		-0.01		0.01	0.05
C_{56}		0.02		-0.01	0.12
Symmetry	†	$P\bar{1}$	$I\bar{4}2d$	$P\bar{1}$	$P1$

† Küppers *et al.* have not determined the spacegroup of the compound they used in the elasticity measurements.

First, we notice that the elastic constants were determined from sound velocities measured with Brillouin-zone spectroscopy along the [010], [110] and [111] direction. Equations which hold for cubic crystals [14,28], the reported symmetry of dodecasil-3C at the time of the experiments, were applied to calculate the elastic constants from the sound velocities. This method yields C_{11} , C_{12} and C_{14} as independent elastic constants. For crystals with a lower symmetry sound velocities in more directions are needed to determine the elastic constants. (See e.g. Ref. 29.) Thus, in this experiment it could not be detected if the local

symmetry of the sample was perhaps lower than cubic, as indicated by recent ^{29}Si NMR measurements on as-synthesized room temperature forms of dodecasil-3C [4,11]. Also, the symmetry of our calculated structures is lower than cubic. Therefore, we compare the calculated C_{11} , C_{12} and C_{44} with experiment and consider the remaining computed constants as predictions. (See Table 6.3.) Furthermore, we compare calculated elastic constants of empty dodecasil-3C with experimental data [14] of dodecasil-3C that contains the guest molecules mentioned earlier. The X-ray powder diagrams of Hofman *et al.* [30] indicate that as-synthesized dodecasil-3C contracts slightly upon calcination. This might affect our comparison between calculated elastic constants of the empty framework and the experimental data. To estimate this effect, we expanded the unit cells of our calculated structures with 1% by applying a small negative pressure in our minimizations. This volume change is well above the value obtained from the unit cell data of calcined dodecasil-3C [10] and those of the material used by Küppers *et al.* [14]. For the expanded structures we re-calculated the elastic constants. Elastic constants that have changed more than a few percent are listed in Table 6.3. These data imply that the presence of guest molecules has only a small effect on the elastic constants of the framework.

The BJS I potential predicts values for C_{11} , C_{12} and C_{14} that are in reasonable agreement with experiment. Both the KFBS and JC potentials predict these constants less accurately than the BJS I potential. (See Table 6.3.) The worse KFBS predictions for the elasticity of dodecasil-3C seem peculiar when compared with predictions for other silicates. The KFBS predictions for the elastic constants of coesite and stishovite are more accurate than those of both other potentials. (See Appendix.) Similar results were obtained for predictions on the high pressure elasticity of α -quartz [31]. Therefore, we would not expect that KFBS predictions for the elastic constants of dodecasil-3C are less accurate than those of the JC and BJS I potential, *unless* the KFBS-predicted structure is less accurate. The following arguments indicate that the latter must be the case. We have seen that the KFBS-predicted symmetry for dodecasil-3C differs substantially from the BJS I and JC predictions. The latter potentials predict similar symmetries for dodecasil-3C, although they are parametrized in completely different ways: The JC potential is derived from empirical data on α -quartz, whereas the BJS I potential is solely derived from *ab initio* data of small silicious clusters. Furthermore, the JC potential predicts a large range of all-silica structures very accurately [32]. Also, for zsm-5 and ssz-24 it has been shown [32,33] that the KFBS-predicted symmetries are not in accordance with experiment, in contrast to the BJS I and JC predictions.

6.3.3 Predicted and experimental dodecasil-3C structures

The BJS I potential predicts that dodecasil-3C without guest molecules is triclinic with space group $P\bar{1}$ for temperatures ranging from 0 to 1200 K. The KFBS-predicted structure in this temperature range is tetragonal with space group $I42d$. The JC potential predicts that the structure of dodecasil-3C is triclinic with space group $P1$. This structure is thermally stable up to 400 K. We compare the predicted structures with (split position refined) single-crystal data of Könneck *et al.* [10] that were obtained for a calcined sample at $T \approx 523\text{ K}$. As we are not aware of single-crystal data on the structure of calcined dodecasil-3C at lower temperatures, we will also compare the JC-predicted structure at

400 K with the data of Könneck *et al.*, thereby assuming that the structure does not change much in the range 400 K to 500 K. Table 6.4 presents the data of Könneck *et al.* in comparison with the JC-predicted structure at 400 K and predictions of both other potentials for the structure at 500 K. The JC-predicted unit cell parameters are much closer to experiment than those of both other potentials. All three potentials predict Si-O distances that are considerably larger than the experimental values. The KFBS-predicted Si-O-Si bond angles are closest to the experiment, while both the BJS I and JC potential seem to underestimate these values.

Table 6.4. Predictions for the structure of dodecasil-3C compared with experimental (split position refined) data for calcined dodecasil-3C at $T = 523 \pm 15$ K [10]. Distances are in Å and angles in degrees.

Property	Expt.	BJS I	KFBS	JC
a	19.369	18.796	19.758	19.239
b	19.369	18.694	19.758	19.247
c	19.369	18.860	19.925	19.455
α	90.00	89.75	90.00	89.98
β	90.00	90.08	90.00	90.13
γ	90.00	89.36	90.00	89.95
d_{Si-O_s}	1.569	1.589	1.595	1.588
d_{Si-O_i}	1.598	1.622	1.616	1.607
$\langle d_{Si-O} \rangle$	1.581	1.605	1.606	1.597
$\angle_{Si-O-Si_s}$	150.9	132.6	158.6	141.3
$\angle_{Si-O-Si_i}$	175.8	156.6	177.0	175.9
$\langle \angle_{Si-O-Si} \rangle$	163.5	143.5	169.8	156.1
\angle_{O-Si-O_s}	104.3	102.7	107.7	109.5
\angle_{O-Si-O_i}	114.4	115.1	111.4	113.0
d_{Si-Si_s}	3.066	2.989	3.140	3.031
d_{Si-Si_i}	3.156	3.105	3.228	3.176
$\langle d_{Si-Si} \rangle$	3.123	3.051	3.188	3.113
Symmetry	$Fd\bar{3}m$	$P\bar{1}$	$I42d$	$P1$

The predictions for dodecasil-3C are peculiar when compared with predictions of all three potentials for a large number of *other* all-silica structures [32]. The Si-O bond distances in the latter frameworks, which were calculated with all three potentials [32], are much closer to experiment than the bond distances predicted for dodecasil-3C. Furthermore, the Si-O-Si bond angles in all silicas studied [32] are overestimated by the KFBS potential, underestimated by the BJS I potential and most accurately predicted by the JC potential. However, *both* the JC and BJS I potential seem to underestimate the Si-O-Si bond angles in dodecasil-3C while the KFBS prediction is closest to experiment. Furthermore, the BJS I-predicted Si-O-Si bond angles in dodecasil-3C deviate much more from experiment than the predictions for other all-silica polymorphs [32]. If the BJS I-predicted dodecasil-3C structure really deviates that much from experiment, then it is peculiar that the potential still predicts the elastic constants for this framework reasonably. (See Table 6.3.) Also,

if the KFBS-predicted structure is accurate, then it is peculiar that this potential does not predict elastic constants that are in agreement with experiment. This was argued in Sec. III.2. The predictions of each potential for the structure of dodecasil-3C would be consistent with those for other all-silica frameworks, when in the *actual* dodecasil-3C structure the Si-O-Si bond angles would be smaller and the Si-O bond distances would be larger than the experimental values reported so far [10]. We notice that JC predictions for the nearest neighbor Si-Si distances do *not* differ much from the experimental values. The KFBS and BJS I predictions for the Si-Si distances in dodecasil-3C are consistent with those predicted for a large number of other all-silica frameworks [32]. This suggests that in the actual structure the O atoms may be further away from the line connecting nearest neighbor Si-Si atoms, than indicated by experiment. Thus, the O positions in the experimental structure of calcined dodecasil-3C may not be well-resolved. Our conclusions agree with the observation [10] that refinement of the calcined dodecasil-3C structure in the space group $Fd\bar{3}m$ with O atoms on split positions gives lower values for the Si-O-Si bond angles and higher values for the the average Si-O bond distances than the conventional refinement in that space group.

6.4 Conclusions

The shell model calculations indicate that the local symmetry of dodecasil-3C without guest molecules is triclinic for temperatures between 0 and 1200 K. For the KFBS predictions, that indicate a different structure, we have shown that they are less reliable. The JC potential predicts that the triclinic structure undergoes a small displacive phase transition at $T = 300$ K where the symmetry of the framework changes from $P\bar{1}$ to $P1$. According to the BJS I potential, this structure remains a single phase with space group $P\bar{1}$ in the temperature range studied. More experiments are needed to determine the accuracy of these predictions. Our calculations indicate that the experimental values reported for the Si-O-Si bond angles in dodecasil-3C might be too large whereas those for the Si-O bond distances might be too small. This may be due to less well-resolved positions of the O atoms in the experimental dodecasil-3C structure. Furthermore, the BJS I potential predicts values for the elastic constants C_{11} , C_{12} and C_{44} that are in reasonable agreement with experiment. The experimental values were obtained by the application of cubic symmetry in the equations that relate the elastic constants to the measured sound velocities. As our calculations indicate that the local symmetry of empty dodecasil-3C might be lower than cubic, it might be interesting to perform additional elasticity measurements on calcined dodecasil-3C and to compare these results with the BJS I predictions.

6.5 Appendix: Calculations on stishovite and coesite

Tables 6.5 and 6.6 present calculated structures and elastic constants of stishovite and coesite in comparison with experiment. The KFBS values for both the structure and elastic constants of those silicates are the closest to experiment.

Table 6.5. Calculations of the structure and elastic constants of coesite at room temperature, compared with experiment. Experimental values for the elastic constants are from Ref. 29. Experimental data for the structure are from Ref. 34. Lengths are in Å and angles in degrees. Elastic constants, denoted as C_{ij} , are in 10^{10}N/m^2 .

Property	Expt.	BJS I	KFBS	JC
a	7.137	6.851	7.157	6.816
b	12.37	12.15	12.51	12.29
c	7.174	7.026	7.275	7.118
β	120.3	120.0	120.7	119.4
d_{Si-O_s}	1.595	1.567	1.581	1.570
d_{Si-O_i}	1.621	1.637	1.621	1.628
$\langle d_{Si-O} \rangle$	1.609	1.614	1.605	1.611
$\angle_{Si-O-Si_s}$	137.2	127.1	145.1	132.8
$\angle_{Si-O-Si_i}$	180.0	179.99	179.99	180.00
$\langle \angle_{Si-O-Si} \rangle$	150.8	140.3	154.6	143.9
\angle_{O-Si-O_s}	108.0	104.8	104.3	105.0
\angle_{O-Si-O_i}	110.4	114.6	115.6	112.7
C_{11}	16.08	11.97	17.30	9.32
C_{12}	8.21	6.15	8.21	6.26
C_{13}	10.29	6.45	10.60	7.42
C_{15}	-3.62	-1.17	-2.93	0.47
C_{22}	23.04	21.37	24.89	21.05
C_{23}	3.56	5.53	8.72	6.60
C_{25}	0.26	1.78	0.98	2.17
C_{33}	23.16	22.20	27.83	23.96
C_{35}	-3.93	-5.51	-4.80	-6.03
C_{44}	6.78	5.13	2.77	3.36
C_{46}	0.99	1.24	-0.83	0.70
C_{55}	7.33	4.49	5.90	4.77
C_{66}	5.88	4.13	3.92	3.95
Symmetry	$C2/c$	$C2/c$	$C2/c$	$C2/c$

Table 6.6. Calculations of the structure and the elastic constants of stishovite at room temperature, compared with experiment. Experimental values for the elastic constants and the structure are from Ref. 35 and Ref. 36, respectively. Distances are in Å and angles in degrees. Elastic constants, denoted as C_{ij} , are in 10^{10}N/m^2 .

Property	Expt.	BJS I	KFBS	JC
a	4.177	4.102	4.164	4.034
c	2.665	2.595	2.667	2.776
$d_{\text{Si-O}_4}$	1.757	1.753	1.758	1.784
$d_{\text{Si-O}_1}$	1.809	1.722	1.799	1.733
$\langle d_{\text{Si-O}} \rangle$	1.774	1.742	1.771	1.767
$\angle_{\text{Si-O-Si}}$	130.7	132.3	130.7	128.9
$\angle_{\text{O-Si-O}_1}$	81.3	84.5	81.3	77.8
$\angle_{\text{O-Si-O}_2}$	180.0	180.0	180.0	180.0
$\angle_{\text{O-Si-O}_3}$	90.0	90.0	90.0	90.0
$\angle_{\text{O-Si-O}_4}$	98.7	95.5	98.7	102.2
C_{11}	45.3	67.8	62.5	47.5
C_{12}	21.1	34.8	22.8	30.4
C_{13}	20.3	41.2	26.8	36.1
C_{33}	77.6	98.9	93.3	86.6
C_{44}	25.2	26.8	26.9	14.7
C_{66}	30.2	37.9	26.1	39.6
Symmetry	$P4_2/mnm$	$P4_2/mnm$	$P4_2/mnm$	$P4_2/mnm$

6.6 References

- [1] H. Gies, F. Liebau and H. Gerke, *Angew. Chem.* **82**, 214 (1983).
- [2] H. Gies, *Z. Kristallogr.* **167**, 73 (1984).
- [3] H. Gies, *Nachr. Chem. Tech. Lab.* **33**, 387 (1985).
- [4] C.A. Fyfe, H. Gies and Y Feng, *J. Am. Chem. Soc.* **111**, 7702 (1989).
- [5] F. Liebau, H. Gies, R.P. Gunawardane and B. Marler, *Zeolites* **6**, 373 (1986).
- [6] M. Könnecke, PhD. thesis, University of Darmstadt (1992).
- [7] M. Könnecke and H. Fuess, *Zeolites* **15**, 264 (1995).
- [8] R.P. Gunawardane, *Indian J. Chem.* **27A**, 380 (1988).
- [9] E.J.J. Groenen, N.C.M. Alma, J. Dorrepaal, G.R. Hays and A.G.T.G. Kortbeek, *Zeolites* **5**, 361 (1985).
- [10] M. Könnecke, G. Miehe and H. Fuess, *Z. Kristallogr.* **201**, 147 (1992).
- [11] J.S. Tse, M. Desando, J.A. Ripmeester and Y.P. Handa, *J. Am. Chem. Soc.* **115**, 281 (1993).
- [12] G.T. Kokotailo, C.A. Fyfe, G.C. Gobbi, G.J. Kennedy, and C.T. DeSchutter, *J. Chem. Soc. Chem. Commun.* **1984**, 1208 (1984).
- [13] A.J.M. de Man, H.K. Küppers and R.A. van Santen, *J. Phys. Chem.* **96**, 2092 (1992).
- [14] R. Freimann and H. Küppers, *Phys. Stat. Sol. (a)* **123**, K123 (1991).
- [15] S.C. Parker, computercode: PARAPOCS, BATHPROGS, School of Chemistry, University of Bath, Claverton Down, Bath BA2 7AY, U.K.
- [16] S.C. Parker and G.D. Price, *Advances in Solid-Sate Chem.* **1**, 295 (1989).
- [17] C.R.A. Catlow and M.J. Norgett, *Lattice Structure and Stability of Ionic Materials*, private communication.
- [18] A. Pavesi, private communication.
- [19] G.J. Kramer, N.P. Farragher, B.W.H. van Beest and R.A. van Santen, *Phys. Rev. B* **43**, 5068 (1991).
- [20] R.A. Jackson and C.R.A. Catlow, *Mol. Simul.* **1**, 207 (1988).
- [21] K. de Boer, A.P.J. Jansen and R.A. van Santen, *Chem. Phys. Lett.* **223**, 46 (1994), it Chapter 2 of this thesis).
- [22] G.J. Kramer, A.J.M. de Man and R.A. van Santen, *J. Am. Chem. Soc.* **113**, 6435 (1991).
- [23] H.K. Chae, W.G. Klemperer, D.A. Payne, C.T.A. Suchicital, D.R. Wake and S.R. Wilson, *ACS Symp. Series* **455**, 528 (1991).
- [24] M. Könnecke, private communication.
- [25] R.B. Sosman, *The Phases of Silica* (Rutgers University Press, New Brunswick, 1965).
- [26] P. Richet, Y. Bottinga, L. Denielou, J.P. Petitet and C. Tequi, *Geochim. Cosmochim. Acta* **46**, 2639.
- [27] G.K. Johnson, I.R. Tasker and D.A. Howell, *J. Chem. Thermodynamics* **19**, 617 (1987).
- [28] J. de Launay, *Solid. State. Phys.* **2**, 220, (1956).
- [29] D.J. Weidner and H.R. Carleton, *J. Geophys. Res.* **82**, 1334 (1977).
- [30] R. Hofmann and W. Sterzel, *Z. Kristallogr.* **200**, 101 (1992).
- [31] K. de Boer, A.P.J. Jansen, R.A. van Santen, S.C. Parker and G.W. Watson, *Phys. Rev. B. in press, (Chapter 3 of this thesis.)*
- [32] K. de Boer, A.P.J. Jansen and R.A. van Santen, *Phys. Rev. B* **52**, 12579 (1995), (*Chapter 5 of this thesis*).
- [33] A.J.M. de Man, W.P.J.H. Jacobs, J.P. Gilson and R.A. van Santen, *Zeolites* **12**, 862 (1992).
- [34] K.L. Geisinger, M.A. Spackman and G.V. Gibbs, *J. Phys. Chem.* **91** (1987) 3237.
- [35] W. Sinclair and A.E. Ringwood, *Nature* **78**, 714 (1978).
- [36] D.J. Weidner, J.B. Bass, A.E. Ringwood and W. Sinclair, *J. Geophys. Res.* **87**, 4760 (1982).

Summary and conclusions

In this thesis we studied all-silica polymorphs using computational methods based on interatomic potentials. The aim of our research was threefold. The first aim was to derive interatomic potentials that are suitable for computing the physical properties of all-silica systems. The second aim was to investigate the reliability of these potentials. The third aim was to apply these potentials in studies on the physical properties of several all-silica polymorphs.

In Chapter 1 we described two types of interatomic potentials considered in this thesis: The rigid-ion model potential where each ion is assumed to be non polarizable and the shell model potential which takes polarizability into account. Subsequently, we treated the theoretical background of the calculations, which is the dynamical theory of harmonic crystals. Major assumption in this theory is that the vibrational motions of the ions in the solid can be described by collective harmonic oscillators. Although assumptions are made in the theory, results of the calculations are most critically determined by the interatomic potential used.

In Chapter 2 we derived a shell model potential (BJS I) from *ab initio* data. The covalent parameters of this potential were determined from *ab initio* potential energy surfaces of small clusters. The energies of these clusters were calculated with Møller-Plesset second-order perturbation theory. The ionic and shell charges of the BJS I potential were determined from *ab initio* dipole moments and polarizabilities of larger clusters. The larger clusters calculations were done with self-consistent Hartree-Fock. Subsequently, we compared predictions of the BJS I potential with results of two other well-known potentials. These potentials are the rigid-ion model potential (KFBS) derived by Kramer *et al.* and the shell model potential (JC) determined by Catlow *et al.* We found that BJS I predictions for the structure of several all-silica systems are less accurate than those of the JC and KFBS potential. However, BJS I predictions for the elastic constants and the vibrational spectrum of α -quartz agree better with experiment.

The reliability of the three potentials is investigated more thoroughly in Chapter 3. With these potentials we computed physical properties of α -quartz at variable temperatures and pressures. We compared the results with experimental data. We found that the JC potential can model the structure and elasticity of α -quartz at variable temperatures. Accurate predictions are also given for the vibrational and thermodynamic properties of this material at variable temperatures. The JC potential can not predict the behavior of α -quartz at high pressures. This is due to underestimation of the Si-O-Si bond angle and the O-O repulsions at *short* interatomic distances. The KFBS potential gives less accurate predictions for the structure, vibrational and thermodynamic properties of α -quartz at variable temperatures. This is mainly due to overestimation of the Si-O-Si bond angle. The KFBS potential gives good predictions for the mechanical properties of α -quartz up to high pressures. The BJS I potential predicts the structure of α -quartz at any pressure and temperature less accurately than both other potentials. This potential gives accurate predictions for the elastic, vibrational and thermodynamic properties of α -quartz at variable temperatures. Also, the mechanical behavior of this material is reasonably predicted. The worst prediction for the α -quartz structure is caused by two effects. The BJS I potential systematically underestimated both the Si-O-Si bond angle and the O-O repulsions. The

underestimated O-O repulsions partially compensate for the too small Si-O-Si bond angle. Predictions for properties other than the structure are therefore less affected. Finally, having analyzed the predictions of each potential for α -quartz, we argued why we expect similar results for *other* systems.

Attempts to improve the BJS I potential were described in Chapter 4. To improve this potential, we fitted on *ab initio* data calculated with more accurate methods than used in the BJS I parametrization. We obtained a potential with charges that differ slightly from the BJS I values. Despite these small differences the structure predictions of this potential were not satisfactory. Therefore, we optimized one charge parameter on the structure of α -quartz and fitted the remaining parameters on *ab initio* data of small clusters. We compared predictions of the latter potential (BJS II) with results of the three potentials mentioned before. We found that BJS II predictions for several structures are far more accurate than the BJS I and KFBS results. The BJS II results are comparable to those of the JC potential. Our results indicate that the BJS II potential can model phonon dispersion curves and thermodynamical properties of all-silica systems at variable temperatures. The BJS II predictions are similar to those of the JC and BJS I potential. The BJS II potential can not be used for describing the elasticity and the pressure behavior of those systems. This is in contrast with the KFBS and BJS I potential. The BJS II potential is unsuitable for pressure studies because it is partially optimized on the structure of α -quartz at ambient pressure. This optimization has stiffened the Si-O-Si bond angle and the O-O repulsions for interatomic distances normally occurring in silicates. At shorter distances these interactions remain too weak.

In Chapter 5 we used the interatomic potentials to study the structure and stability of all-silica polymorphs. We considered a large number of all-silica zeolites and denser systems. Calculations were done with the four potentials mentioned above and the rigid-ion model potential (TTA) derived by Tsuneyuki *et al.* We found that BJS II and JC predictions for a large number of structures are far more accurate than results of the other potentials. Our calculations further indicate that the experimental structures of zsm-11 and zsm-12 might not be accurate. We found that only the shell model potentials give reasonable predictions for the relative stability of all-silica systems. We have tried to explain this. Using the BJS II and JC potential, we studied structure-stability relationships that have been proposed in literature. These proposals are based on experimental data for a few materials. We found that linear relationships between structural features and the relative stability do not exist when a large number of structures is considered. Our results support the hypothesis that large-pore materials are destabilized by small Si-O-Si bond angles in the structure.

In Chapter 6 we studied the structure and elasticity of dodecasil-3C at variable temperatures. Calculations were done with the JC, BJS I and KFBS potential. We did not use the BJS II and TTA potential because they are less suitable for elasticity studies. Results of the shell model calculations indicate that the local symmetry of dodecasil-3C without guest molecules is triclinic for temperatures between 0 and 1200 K. The KFBS predictions, indicating a different structure, are less reliable. The JC potential predicts that the triclinic structure undergoes a small displacive phase transition at $T = 300$ K. The symmetry of the framework changes from $P\bar{1}$ to $P1$ during this transition. The BJS

I potential predicts that dodecasil-3C remains a single phase with space group $P\bar{1}$ in the temperature range studied. More experimental data is needed to verify these predictions. The BJS I potential predicts elastic constants for the triclinic structure that agree well with available experimental data. The experimental values were obtained under the assumption that the symmetry of dodecasil-3C is cubic. Our calculations indicate that the local symmetry of empty dodecasil-3C might be lower than cubic. It might therefore be interesting to perform additional elasticity measurements on the calcined material and to compare the results with our calculations. Our results further indicate that the oxygen positions in the experimental dodecasil-3C structure may not be well-resolved.

Samenvatting en conclusies

In dit proefschrift hebben we onderzoek gedaan naar silica kristallen. Hierbij hebben we rekenmethoden gebruikt die gebaseerd zijn op interatomaire potentialen. Het doel van ons onderzoek was drieledig. Hoofddoel was het afleiden van interatomaire potentialen die geschikt zijn voor het berekenen van de fysische eigenschappen van voornoemde systemen. Het tweede doel was het testen van de betrouwbaarheid van deze potentialen. Het derde doel bestond uit de toepassing van deze potentialen in studies naar de fysische eigenschappen van deze verbindingen.

In hoofdstuk 1 hebben we twee soorten interatomaire potentialen beschreven die gebruikt worden in dit proefschrift. Het eerste type is de rigid-ion model potentiaal waarbij elk ion in de vaste stof als niet polariseerbaar wordt beschouwd. Het tweede type is de shell model potentiaal waarmee polariseerbare ionen kunnen worden beschreven. Vervolgens hebben we de theoretische achtergrond van de berekeningen behandeld. De berekeningen zijn gebaseerd op de dynamische theorie van harmonische kristallen. Belangrijkste aanname in deze theorie is dat de trillingen van de atomen in het kristal beschouwd worden als onafhankelijke harmonische oscillatoren. Alhoewel de theorie gebaseerd is op aannames, worden de uitkomsten van de berekeningen voornamelijk bepaald door de betrouwbaarheid van de gebruikte interatomaire potentiaal.

In hoofdstuk 2 hebben we parameters voor een shell model potentiaal (BJS I) afgeleid uit *ab initio* data. De covalente parameters van deze potentiaal zijn bepaald uit *ab initio* potentiaal energie oppervlakken van kleine clusters. De energieën van deze clusters zijn berekend met Møller-Plesset tweede-orde storingstheorie. Parameters van de BJS I potentiaal die de ion en de shell lading bepalen, zijn bepaald uit *ab initio* dipool momenten en polariseerbaarheden van grotere clusters. We hebben de self-consistente Hartree-Fock theorie gebruikt voor berekeningen aan deze grotere clusters. Vervolgens hebben we voorspellingen van de BJS I potentiaal vergeleken met resultaten van twee andere veel gebruikte potentialen. Deze potentialen zijn de rigid-ion model potentiaal (KFBS) afgeleid door Kramer c.s., en de shell model potentiaal (JC) gepubliceerd door Catlow c.s.. We hebben gevonden dat de BJS I potentiaal de structuur van verschillende kristallen slechter voorspelt dan de KFBS en JC potentiaal. Echter, BJS I voorspellingen voor de elasticiteit en het vibrationele spectrum van het kristal α -quartz zijn aanmerkelijk beter.

We hebben de betrouwbaarheid van bovengenoemde potentialen grondiger getest in hoofdstuk 3. Met deze potentialen hebben we een groot aantal fysische eigenschappen van α -quartz bij verschillende drukken en temperaturen berekend. De resultaten hebben we vergeleken met experimentele data. We hebben gevonden dat de JC potentiaal accurate voorspellingen geeft voor de structuur en elasticiteit van α -quartz bij verschillende temperaturen. Ook worden goede voorspellingen gegeven voor de vibrationele en thermodynamische eigenschappen van dit materiaal bij variabele temperatuur. De JC potentiaal is ongeschikt voor berekeningen aan α -quartz bij hoge drukken. Dit komt doordat de potentiaal een te lage waarde geeft voor de Si-O-Si bindingshoek en de repulsies tussen de zuurstof atomen op *korte* interatomaire afstanden als te zwak beschrijft. De KFBS potentiaal geeft minder nauwkeurige voorspellingen voor de structuur, thermodynamische en vibrationele eigenschappen van α -quartz bij verschillende temperaturen. Dit komt voornamelijk doordat de KFBS potentiaal een te hoge waarde voorspelt voor de Si-O-Si

bindingshoek. Deze potentiaal geeft wel goede voorspellingen voor de mechanische eigenschappen van α -quartz bij variabele druk. De BJS I potentiaal voorspelt de structuur van α -quartz, bij variabele druk en temperatuur, slechter dan beide andere potentialen. Deze potentiaal geeft wel goede voorspellingen voor de elasticiteit tezamen met de vibrationele en thermodynamische eigenschappen van dit materiaal bij variabele temperatuur. Tevens wordt het mechanische gedrag van α -quartz redelijk beschreven. Er zijn twee oorzaken aan te wijzen voor de matige voorspelling van de α -quartz structuur. De BJS I potentiaal onderschat systematisch zowel de Si-O-Si bindingshoek als de repulsies tussen de zuurstof atomen. Doordat de te zwakke O-O repulsies gedeeltelijk compenseren voor de te kleine Si-O-Si bindingshoek, worden andere eigenschappen dan de structuur van α -quartz wel redelijk voorspeld. Na analyse van de α -quartz resultaten hebben we aannemelijk gemaakt waarom van elke potentiaal vergelijkbare resultaten verwacht kunnen worden voor *andere* systemen.

Pogingen om de BJS I potentiaal te verbeteren hebben we beschreven in hoofdstuk 4. Ten einde deze potentiaal te verbeteren, hebben we gefit op *ab initio* data berekend met een accuratere methode dan gebruikt bij de BJS I parametrisatie. Dit leverde een potentiaal op met ladingen die weinig verschil vertonen met de BJS I parameters. Ondanks deze kleine ladingsverschillen geeft deze potentiaal een slechte voorspelling van de α -quartz structuur. Daarom hebben we de ladingen geoptimaliseerd op de structuur van α -quartz en de resterende parameters gefit op *ab initio* data van kleine clusters. Resultaten van deze laatste potentiaal (BJS II) hebben we vergeleken met die van de andere potentialen. We hebben gevonden dat BJS II voorspellingen voor diverse structuren aanmerkelijk nauwkeuriger zijn dan die van de KFBS en BJS I potentiaal. De BJS II voorspellingen zijn vergelijkbaar met resultaten van de JC potentiaal. Onze resultaten geven aan dat de BJS II potentiaal geschikt is voor de berekening van fonon-dispersie diagrammen en thermodynamische eigenschappen van pure silica systemen. De BJS II potentiaal is dan vergelijkbaar met de BJS I en JC potentiaal. De BJS II potentiaal is niet geschikt om het gedrag van deze systemen bij hoge druk te berekenen, dit in tegenstelling tot de KFBS en BJS I potentiaal. De BJS II potentiaal is ongeschikt voor hoge druk studies omdat hij geoptimaliseerd is op de structuur van α -quartz bij atmosferische druk. Deze optimalisatie heeft alleen de Si-O-Si bindingshoek vergroot en de O-O repulsies versterkt voor interatomaire afstanden die normaal voorkomen in silica. Voor kleinere afstanden blijven deze interacties te zwak.

In hoofdstuk 5 hebben we de interatomaire potentialen toegepast in studies naar de structuur en de stabiliteit van silica systemen. We hebben gekeken naar een groot aantal zeolieten en systemen met een hogere dichtheid. De berekeningen in deze studie zijn gedaan met de vier eerder genoemde potentialen en de rigid-ion model potentiaal (TTA) afgeleid door Tsuneyuki c.s.. We hebben gevonden dat BJS II en JC voorspellingen voor een groot aantal structuren veel nauwkeuriger zijn dan die van de andere potentialen. Voorts wijzen onze resultaten in de richting dat de experimentele structuren van zsm-11 en zsm-12 niet nauwkeurig zijn. Ook hebben we gevonden dat alleen de shell model potentialen redelijke voorspellingen geven voor de relatieve stabiliteit van pure silica systemen. Dit hebben we geprobeerd te verklaren. Met de JC en BJS II potentiaal hebben we hypothesen uit de literatuur getest die betrekking hebben op de structuur en de stabiliteit van pure silica

systemen. Deze hypothesen zijn gebaseerd op experimentele data voor een beperkt aantal materialen. Uit de berekeningen is gebleken dat er geen lineaire relaties bestaan tussen structuur-eigenschappen en de relatieve stabiliteit als er een groot aantal systemen wordt beschouwd. Onze resultaten zijn alleen in overeenstemming met de hypothese dat materialen met grote porieën gedestabiliseerd worden door kleine Si-O-Si bindingshoeken in de structuur.

In hoofdstuk 6 hebben we de structuur en elasticiteit van dodecasil-3C bij variabele temperatuur onderzocht. Deze berekeningen zijn gedaan met de KFBS, BJS I en JC potentiaal. De TTA en de BJS II potentiaal hebben we niet gebruikt omdat deze minder geschikt zijn voor elasticiteits studies. Uit resultaten van de shell model berekeningen is gebleken dat de lokale symmetrie van dodecasil-3C triclief is voor temperaturen tussen 0 en 1200 K. De KFBS resultaten, die een andere symmetrie impliceren, zijn minder betrouwbaar. De JC potentiaal voorspelt dat de triclief structuur een fase overgang vertoont bij 300 K. Bij deze fase overgang, waarbij geen bindingen verbroken worden, verandert de kristal symmetrie van $P\bar{1}$ naar $P1$. De BJS I potentiaal voorspelt dat dodecasil-3C ruimte groep $P\bar{1}$ heeft en geen fase overgang vertoont in het bestudeerde temperatuur gebied. Op grond van huidige experimentele data kan de juistheid van bovengenoemde voorspellingen niet geverifieerd worden. De BJS I potentiaal voorspelt elasticiteits constanten voor de triclief structuur die goed overeenstemmen met de experimentele data die voorhanden is. Experimentele waarden voor deze constanten zijn verkregen uit metingen waarbij werd aangenomen dat dodecasil-3C kubisch is. Onze berekeningen wijzen echter uit dat de symmetrie van dit materiaal lager is. Het zou daarom interessant zijn om extra elasticiteits metingen te doen aan gecalcineerd dodecasil-3C en de resultaten te vergelijken met onze berekeningen. Onze resultaten impliceren verder dat de zuurstof posities in de experimentele dodecasil-3C structuur niet erg precies bepaald zijn.

List of publications

1. K. de Boer, J.J.C. Mulder and W.J.A. Maaskant, *On the enumeration of basisfunctions for a double chain of $S = 1/2$ ions: A resonating valence bond problem*,
J. Mol. Struct. (Theochem) **229**, 15–28 (1991).
2. K. de Boer, A.P.J. Jansen and R.A. van Santen,
Ab initio approach to the development of interatomic potentials for the shell model of all-silica polymorphs,
Chem. Phys. Lett. **223**, 46–53 (1994).
3. K. de Boer, A.P.J. Jansen and R.A. van Santen,
Interatomic potentials for zeolites: Derivation of an ab initio shell model potential,
Studies Surf. Sci. Catal. **84**, 2083–2087 (1994).
4. K. de Boer, A.P.J. Jansen and R.A. van Santen,
Structure-stability relationships for all-silica structures,
Phys. Rev. B **52**, 12579–12590 (1995).
5. K. de Boer, A.P.J. Jansen, R.A. van Santen and S.C. Parker,
Lattice-dynamical study of the structure and elasticity of dodecasil-3C at elevated temperatures,
Phys. Rev. B **53**, 14073–14079 (1996).
6. K. de Boer, A.P.J. Jansen, R.A. van Santen, G.W. Watson and S.C. Parker,
Free-energy calculations of thermodynamic, vibrational, elastic and structural properties of α -quartz at variable pressures and temperatures,
Phys. Rev. B **54**, 826–836 (1996).
7. K. de Boer, A.P.J. Jansen, R.A. van Santen and S.C. Parker,
Derivation of an all-silica shell model potential from ab initio data and the structure of α -quartz,
Submitted to: Computational Materials Science.

Dankwoord

In dit dankwoord wil ik me graag richten tot degenen, die een bijdrage hebben geleverd aan het tot stand komen van dit proefschrift. Allereerst wil ik Rutger van Santen bedanken. Je hebt me altijd alle vrijheid gegeven en onze discussies waren bijzonder stimulerend, ook in periodes dat ik het iets minder zag zitten. Tevens heb je het project met de Universiteit van Bath mogelijk gemaakt. Ook heb je me alle gelegenheid gegeven om mijn proefschrift af te ronden. Tevens wil ik Andries de Man bedanken. Met jou heb ik vaak zeer scherpe discussies kunnen voeren, ook in de periode dat je elders werkzaam was. Ik denk met plezier terug aan de vele E-mail conversaties, het doorzakken en de Eindhoven-Berlijn bijeenkomsten. Ook wil ik Erik Teunissen en Eric Meijer bedanken. Jullie hebben de *ab initio* berekeningen gedaan en met name Eric heeft veel T_EXnische problemen opgelost. Verder was onze samenwerking heel plezierig. Tonek Jansen, jij hebt mij geleerd mijn resultaten om te zetten in wetenschappelijke publicaties. Verder was je erg kritisch, hetgeen ik zeer waardeer. I am very grateful to Steve Parker. I enjoyed my stay in Bath very much. We had many discussions about solid state physics and lots of other things. The insight I gained during this period enabled me to finish my thesis. I would also like to thank Allison Wall for teaching me the use of PARAPOCS and Graeme Watson for the many discussions we had. Ook wil ik mijn kamergenoten en overige leden van de vakgroep bedanken voor het gezamenlijk koffiedrinken, borrelen en uiteten gaan. Het was bijzonder gezellig!

En, *last but certainly not least* wil ik Edwin bedanken, voor alles.

Curriculum Vitae

Kristine de Boer werd op 17 december 1965 geboren te Bennebroek. Na het doorlopen van het basisonderwijs begon zij in 1978 aan de VWO opleiding aan het 'College Leeuwenhorst' te Noordwijkerhout. In 1984 werd het VWO diploma behaald. Datzelfde jaar schreef zij zich in voor de studie chemie aan de Rijksuniversiteit Leiden. Deze studie omvatte het hoofdvak Theoretische Anorganische Chemie, onder leiding van prof.dr. W.J.A. Maaskant, en neven vakken op het gebied van de wiskunde en theoretische natuurkunde. In 1989 werd het doctoraal diploma (met genoegen) behaald.

In oktober 1989 begon zij haar promotieonderzoek aan de Technische Universiteit Eindhoven, onder leiding van prof.dr. R.A. van Santen. Tijdens haar promotieonderzoek verbleef zij vier maanden bij de Computational Solid State Chemistry Group aan de Universiteit van Bath (U.K.). Het onderzoek is beschreven in dit proefschrift en diverse publicaties.

Op 23 februari 1996 trad zij in het huwelijk met Edwin Buitenman.

Per 1 september 1996 zal zij in de automatisering werkzaam zijn bij de firma Palmtop, dochteronderneming van Psion Nederland BV, gevestigd te Hoofddorp.

Stellingen

behorende bij het proefschrift

**DERIVATION AND EVALUATION OF
INTERATOMIC POTENTIALS FOR
PURE-SILICA MATERIALS**

K. de Boer

1. Heel veel is al gedaan.
2. De uitspraak, gedaan door de Vos Burchart e.a. dat de de dimensies van de eenheidscel limitaties opleggen aan de betrouwbaarheid van de minimalisatie is niet juist. Er kan altijd een Brillouin-zone sampling worden gedaan om na te gaan of er structuren met grotere eenheidcellen en een lagere energie bestaan: Dit leidt namelijk tot imaginaire frequenties voor fononen met k ongelijk aan nul.
E. de Vos Burchart, Proefschrift, Technische Universiteit Delft, Delft (1992).
3. De wetenschappelijke en sociale vaardigheden van één persoon verhouden zich vaak als de onzekerheden in plaats en impuls zoals gegeven door de Heisenberg relatie.
4. De beschrijving van een interatomaire potentiaal in het werk van Tsuneyuki e.a. is nodeloos verwarrend.
S. Tsuneyuki, M. Tsukada, H. Aoki and Y. Matsui, Phys. Rev. Lett. **61**, 869 (1988).
5. Het geven van aparte voorlichtingsdagen voor vrouwen aan een Technische Universiteit bevordert hun uitzonderingspositie.
6. De fractionele coördinaten van zsm-11 zoals gegeven door Fyfe e.a. zijn niet consistent met de door hun beschreven hoeken en afstanden.
C.A. Fyfe, H. Gies, G.T. Kokotailo, C. Pasztor, H. Strobl and D.E. Cox, J. Am. Chem. Soc. **111**, 2470 (1989).
7. Het labjournaal geeft een realistischer beeld van wetenschappelijk onderzoek dan de publicaties.
8. De Brillouin-zone scattering experimenten van Freimann e.a., ter bepaling van de elasticiteitsconstanten van dodecasil-3C, dienen ook in andere richtingen dan [100], [110] en [001] gedaan te worden. Alleen dan kan nagegaan worden of elasticiteits constanten anders dan C_{11} , C_{12} en C_{44} ook daadwerkelijk nul zijn.
R. Freimann and H. Küppers, Phys. Stat. Sol. (a) **123**, K123 (1991); Hoofdstuk 6 van dit proefschrift.
9. Al scoort een potentiaal nog zo snel, de imaginaire frequentie achterhaalt hem wel.
G.J. Kramer, N.P. Farragher, B.W.H. van Beest and R.A. van Santen, Phys. Rev. B **43**, 5068 (1991); K. de Boer, A.P.J. Jansen and R.A. van Santen Phys. Rev. B **52**, 12579 (1995).
10. Men wordt niet overspannen van de eigen taak maar van het werk dat aan anderen moet worden uitbesteed.

11. Het is geopperd door van Garderen dat het gebruik van drie letter codes voor de naamgeving van zeolieten onrecht doet aan de fantastische structurele diversiviteit van deze materialen. Echter, het verschil in thermodynamische eigenschappen van deze systemen is zo gering dat het gebruik van drie letter woorden volkomen gerechtvaardigd is.
H. van Garderen, Proefschrift, Technische Universiteit Eindhoven, Eindhoven (1995).
12. Wetenschap vertoont een opvallende gelijkenis met koken: Dingen die je het snelst in elkaar flanst worden vaak het meest gewaardeerd.
13. Extrapolatie, zoals gedaan door de Vos Burchard e.a., van een relatie tussen positieve druk en de temperatuur waarbij α -quartz overgaat in β -quartz, naar resultaten bij negatieve druk mag alleen als de temperatuur- en druk geïnduceerde veranderingen in α -quartz invers zijn. Dit laatste is echter niet het geval.
E. de Vos Burchart, H. van Bekkum and B. van de Graaf, J. Chem. Soc. Faraday Trans. **88**, 1161 (1992).
14. Het boek van Wim Kaiser, getiteld "Vertrouwd en o zo vreemd" en de gelijknamige documentaire houden geen rekening met de belangrijkste principes van de werking van het geheugen, namelijk het scheiden van hoofd en bijzaken en een duidelijke ordening.
15. Het is merkwaardig te noemen dat auteurs die de opheldering claimen van het mechanisme van de α -quartz \rightarrow β -quartz overgang, onderwerp van ruim 100 jaar debat, dit werk alleen in het Russisch publiceren.
Т.Д. Соколовский, Доклады Академии Наук Беларуси, **38**, 46 (1994).
16. Het gebruik door Nicholas e.a. van een 'dielectrische constante' als parameter in een interatomaire potentiaal gaat voorbij aan het feit dat bovengenoemde 'constante', die bovendien een tensorgrootheid is, een macroscopische eigenschap is en dus uit de berekening met de potentiaal zou moeten volgen. Volgens hun redenering zou bijvoorbeeld het smeltpunt van quartz ook een prima potentiaal parameter kunnen zijn.
J.B. Nicholas, A.J. Hopfinger, F.R. Trouw and L.E. Iton, J. Am. Chem. Soc. **113**, 4792 (1991).
17. De opmerking van Ermoshin e.a. dat het forceveld van Hill e.a. vooral gericht is op het beschrijven van correcte energieën is opmerkelijk omdat in het werk van deze laatste auteurs namelijk geen energieën gegeven worden.
V.A. Ermoshin, K.S. Smirnov and D. Bougeard, Chem. Phys. **202**, 53 (1996); J.R. Hill and J. Sauer, J. Phys. Chem. **98**, 1238 (1994).
18. Het fileprobleem dient bij de basis te worden aangepakt: Voer geboorteperking in.